GRANT/FR/IN/24

2000135413 482050

Pgs 176

RFI and SCRIMP Model Development and Verification

Grant Number NAG-1-1881 Supplement 3

Final Report

Period of Performance: December 10, 1998 – May 15, 2000

Alfred C. Loos
Jay Sayre

Department of Engineering Science and Mechanics
Virginia Polytechnic Institute and State University
Blacksburg, VA 24061

August 15, 2000

Prepared For:
Mr. H. Benson Dexter
NASA Langley Research Center
Hampton, VA 23681

ABSTRACT

Vacuum-Assisted Resin Transfer Molding (VARTM) processes are becoming promising technologies in the manufacturing of primary composite structures in the aircraft industry as well as infrastructure. A great deal of work still needs to be done on efforts to reduce the costly trial-and-error methods of VARTM processing that are currently in practice today. A computer simulation model of the VARTM process would provide a cost-effective tool in the manufacturing of composites utilizing this technique. Therefore, the objective of this research was to modify an existing three-dimensional, Resin Film Infusion (RFI)/Resin Transfer Molding (RTM) model to include VARTM simulation capabilities and to verify this model with the fabrication of aircraft structural composites. An additional objective was to use the VARTM model as a process analysis tool, where this tool would enable the user to configure the best process for manufacturing quality composites.

Experimental verification of the model was performed by processing several flat composite panels. The parameters verified included flow front patterns and infiltration times. The flow front patterns were determined to be qualitatively accurate, while the simulated infiltration times over predicted experimental times by 8 to 10%. Capillary and gravitational forces were incorporated into the existing RFI/RTM model in order to simulate VARTM processing physics more accurately. The theoretical capillary pressure showed the capability to reduce the simulated infiltration times by as great as 6%. The gravity, on the other hand, was found to be negligible for all cases.

Finally, the VARTM model was used as a process analysis tool. This enabled the user to determine such important process constraints as the location and type of injection ports and the permeability and location of the high-permeable media. A process for a three-stiffener composite panel was proposed. This configuration evolved from the variation of the process constraints in the modeling of several different composite panels. The configuration was proposed by considering such factors as: infiltration time, the number of vacuum ports, and possible areas of void entrapment.

Table of Contents

List of Figures

List of Tables

Chapter 1 Introduction

Resin Transfer Molding (RTM) processes have become popular methods for manufacturing primary structures in the aerospace industry (1). In a traditional RTM process, a dry, fibrous preform is loaded into a matched-metal mold. The mold is then closed, which compacts the preform, and a thermosetting resin is injected into the preform. See Figure 1.1 for a schematic of this process.

There are several advantages in using RTM over more traditional composite processing techniques. Some of these advantages are as follows (2):

- Very large and complex shapes can be made efficiently and inexpensively.
- The preform eliminates the labor and skill that is required in hand lay-ups.
- Parts can be made with better reproducibility due to the high dimensional accuracy of the mold.
- There is a reduction in the exposure to Volatile Organic Compounds (VOC).

Along with the advantages, there are the inevitable disadvantages (2):

- The mold design is critical, and it can become quite expensive.
- Resin rich areas often form in the edges and radii.

- Reinforcements that move during injection can alter the quality of the finished part.

RTM has lead to the evolution of Vacuum-Assisted Resin Transfer Molding (VARTM) in order to overcome some of its inherent flaws. In the VARTM process, a vacuum bag is used as one of the tool surfaces. This eliminates the need for precise matched-metal mold making that is crucial in conventional RTM. The exact fit of the vacuum bag to the preform drastically reduces resin rich areas, and it also allows for a more efficient way of trapping and controlling VOC emissions that are being more strictly regulated (3). A final advantage of VARTM lies in the low injection pressures (~1 atm). These low pressures allow for little movement of the reinforcement during processing, which produces a better quality part.

Figure 1.2 shows a generalized VARTM lay-up. This lay-up begins with a dry, fibrous preform laid onto an open-faced tool plate. Then, a porous peel-ply is placed on top of the preform, but underneath a resin distribution tube. Next, comes the resin distribution medium. This material, which is also known as the high-permeable distribution medium, covers a large portion of the preform and peel-ply. (Even though VARTM processes do not technically require these high-permeable distribution media, they can be helpful in significantly reducing processing times by providing a low-resistance resin pathway.) The final step in the lay-up is the placement of a vacuum bag over the entire assembly.

Once the lay-up is complete, the processing can be carried out. Figure 1.3 shows a generalized schematic of the VARTM process. First, a vacuum pump is turned on to expel any air from the preform assembly. After the system has equilibrated, the resin is allowed to flow through the resin distribution tube and across the high-permeable distribution medium. The resin then fills the preform in the transverse, or through-the-thickness, direction by "leaking" downward from the high-permeable distribution medium. The vacuum source is left on until the resin system begins to gel. Once the vacuum is turned off, the part may either cure at room temperature, or it can be placed in an oven to assist the curing process. The VARTM process is currently implemented in the manufacturing of Naval structural components (masts, hulls, and bridgedecks), automobile chassis and body components, transportation infrastructure, railroad cars, and turbine blades (4-6).

A great deal of work still needs to be done on efforts to reduce the costly trial-and-error methods of VARTM processing that are currently in practice today. An understanding of the flow behavior of the system prior to production is crucial. A computer simulation model of the VARTM process would provide a cost-effective tool in the manufacturing of composites utilizing this technique. Therefore, the objective of this work was to develop and verify a three-dimensional, VARTM model and to use this model as a process analysis tool.

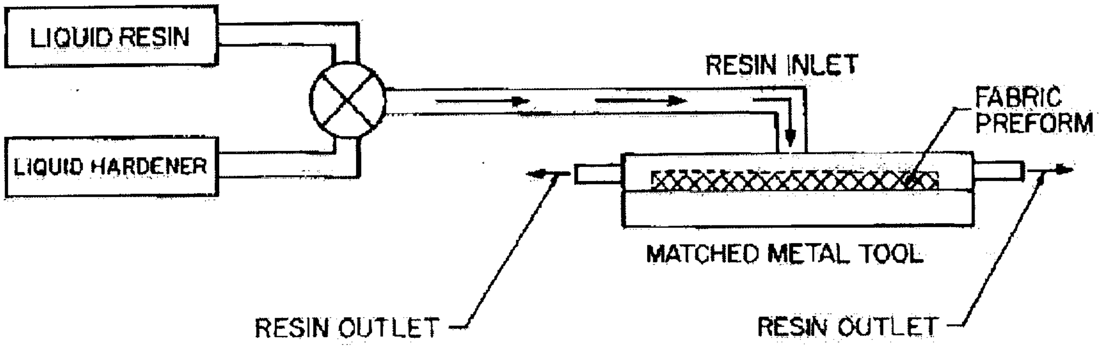

Figure 1.1 RTM Processing Schematic

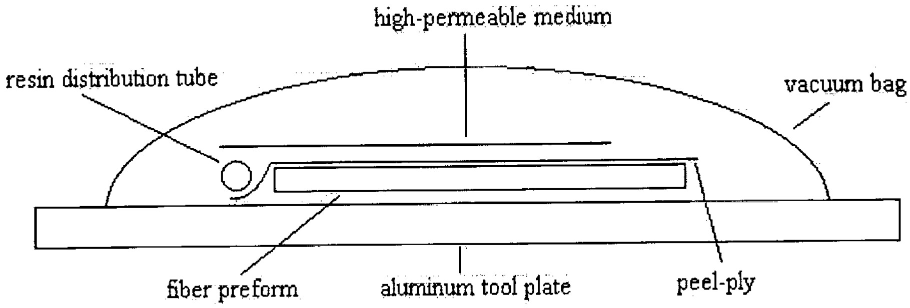

Figure 1.2 VARTM Lay-Up

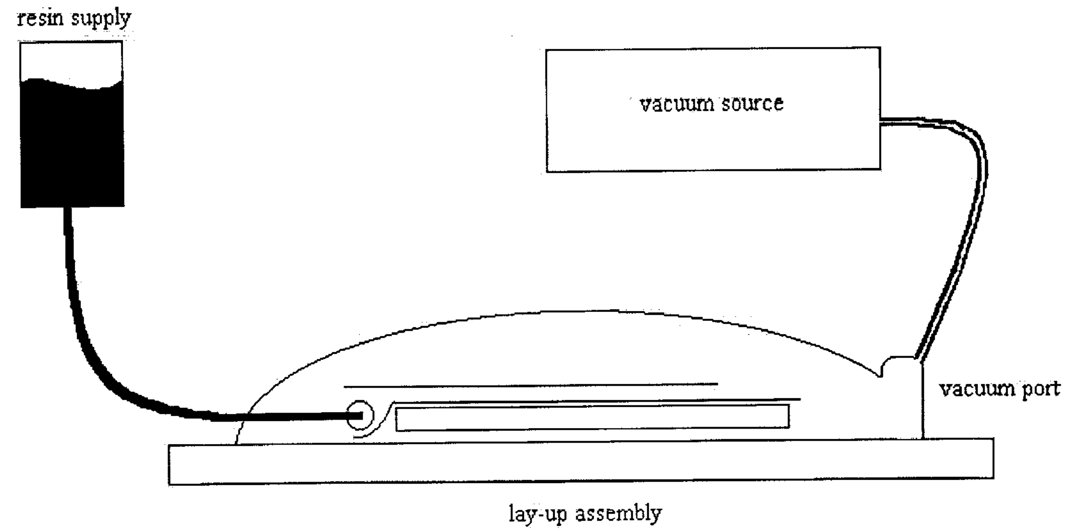

Figure 1.3 VARTM Processing Schematic

Chapter 2 Literature Review

2.1 Permeability

Permeability is defined as the property of a porous material which characterizes the ease with which a fluid may be made to flow through the material due to an applied pressure gradient (7). A porous material is defined as having the following characteristics:

- It is a heterogeneous medium.
- The heterogeneous medium consists of both a solid phase and a void phase.
- The solid phase has a high surface area due to numerous pores.
- The pores are interconnected to form an overall pathway.

The equation that is generally accepted as explaining flow through porous media was first proposed empirically by Darcy (8), and it is known as Darcy's Law:

$$q_i = -\frac{S_{ij}}{\eta}\frac{\partial P}{\partial x_j} \tag{2.1}$$

where, q_i is the i^{th} component of the superficial velocity vector of the fluid, S_{ij} is the permeability tensor of the porous medium, η is the viscosity of the fluid, and $\frac{\partial P}{\partial x_j}$ is the pressure gradient across the porous medium. The superficial velocity is the filter, or discharge, velocity of the fluid flowing through a cross-sectional area. As will be shown later, there is a relationship between the superficial velocity and the average interstitial velocity, $\bar{v}$, at the flow front.

The permeability is often related to the porosity, which is defined as the ratio of the total volume of open pores to the total volume of solid preform. The porosity is also known as the resin volume fraction of the composite. Therefore, the porosity, ϕ , can be related to the fiber volume fraction, v_f , by the following equation (9):

$$\phi = 1 - v_f \tag{2.2}$$

There are two techniques commonly used in measuring the permeability of a preform. These techniques are referred to as the steady-state and advancing front techniques.

Steady-state permeability is measured under constant flow rate conditions using a saturated preform. The pressure differential across the preform is measured, and the permeability is calculated using Darcy's Law. This technique has the advantage of the need for only one preform to measure the permeability of all the fiber volume fractions desired. The disadvantage is that it sometimes does not resemble the actual composite processing conditions.

In the advancing front technique, a fluid is introduced into a dry preform at either a constant flow rate or a constant pressure condition. The flow front may be measured by visual means and/or by the use of pressure transducers. The permeability is then calculated by the use of Darcy's Law. This technique has the advantage of accounting for capillary and gravitational effects, which are essential in either low-flow-rate or low-pressure injection processing techniques. However, it is time consuming because of the use of a new preform for every fiber volume fraction tested.

It is extremely difficult to predict analytically the permeability of a preform with a complicated architecture. Several models have been proposed that relate the permeability to fiber volume fraction (10-15). The most famous of these being the Kozeny-Carman equation (10-11):

$$S = \frac{D_f^{\,2}}{16C} \frac{\left(1 - v_f\right)^3}{v_f^{\,2}} \tag{2.3}$$

where, D_f is the average fiber diameter and C is the Kozeny-Carman constant, which accounts for tortuosity and pore nonuniformity, and is determined by the geometry and orientation of the packing material. The porous medium is assumed to be equivalent to a single channel with an effective diameter equal to four times the hydraulic radius of the medium. The flow velocity is described by the Hagen-Poiseuille equation for laminar flow. A comparison of this velocity with the pore velocity predicted by Darcy's Law gives an expression for the permeability. The short comings of this model are in the fact that it depends on the fiber radius and fiber volume fraction, which limits its effectiveness to in-plane, uniform fiber volume distributions (15).

The permeability of an idealized unidirectional reinforcement was derived form first principles (Navier Stokes equations in a boundary-fitted coordinate system) for flow parallel to and transverse to the fibers (14). This numerical solution was compared to an approximate solution similar to the Kozeny-Carman equation. For flow along the fiber axis, the Kozeny-Carman equation was used. For flow transverse to the fiber axis, a modification to the Kozeny-Carman equation was derived in order to account for the complex, transverse flow around the fiber bundles. Comparisons between the numerical solution and the approximate solution showed good agreement for fiber volume fractions greater than 0.35. The theoretical model was fit to experimental data by adjusting the effective fiber radius to four times larger than the real fiber radius.

The Kozeny-Carman equation was shown to be accurate in predicting permeabilities of woven fabric preforms for porosities up to 0.5 by Ahn et al. (16). Above 0.5, deviations were attributed to interfacial effects between fabric layers. Using the Kozeny-Carman equation, Williams et al. (17) looked at the effect of liquid properties, other than viscosity, on the flow rate through a continuous aligned array of fibers. They found that observed flow rates were much greater than those predicted. They postulated this was due to the surface tensions modifying the method of air entrapment resulting in a non-uniform distribution of fibers in the bed.

Dave and Houle (18) defined the permeability as an effective permeability, S_e, which was equal to the product of S_i and S_r. Here S_i is the intrinsic permeability defined by the Kozeny-Carman equation and S_r is the relative permeability, which varied from 0 to 1. For an unsaturated preform, S_r was equal to 0, and for a fully saturated preform, S_r was equal to 1. The effective permeability was found to be a function of the flow rate, and likewise, the flow rate was found to be a function of the effective permeability. This led to the recommendation of an iterative scheme for permeability calculations.

The asymptotic model of Bruschke and Advani (19-21) was used to examine the transverse permeability of solid rods and fiber bundles. Agreement was found for the measured permeability and the permeability predicted by the asymptotic model for Newtonian fluids flowing transversely to homogeneous arrays of solid rods. The predicted permeability for heterogeneous arrays of fiber bundles, however, was not accurate. Sadiq et al. (22) used Newtonian and shear-thinning fluids to examine the transverse permeability of a homogeneous array of solid rods and a heterogeneous array of porous bundles. Bruschke and Advani's (19-21) model was again used to predict the experimentally determined permeability. Results were in good agreement for the homogeneous array, but again failed in the prediction for the heterogeneous bundles.

Due to the complexity of analytically modeling the permeability, many researchers have focused their efforts on empirically determining it from Darcy's Law. Important factors considered in the evaluation of the permeability were the measurement technique, the anisotropic nature of the preform, the flow direction, and the fluid-surface interaction.

Fingerson (9) found advancing front results to closely match steady-state results for a biaxial, plain weave, 162 E-glass at a fiber volume fraction of 0.55. The in-plane principal permeability values were found to be nearly equal to the permeability values obtained for flow parallel to the stitching of a multiaxial warp knit preform.

Hammond (23) also reported that permeability values for the advancing front technique were similar to those obtained for the steady-state technique at low flow rates and high fiber volume fractions. He determined that through-the-thickness stitching increased transverse permeability due to the creation of flow pathways, and E-glass had a higher permeability than IM7-8HS carbon fabric due to the more complicated flow paths of the carbon fabric. Steady-state permeability testing indicated that the change in viscosity, due to the use of different fluids, had no significant effect on the permeability behavior.

Williams et al. (17) showed that advancing front permeability data matched steady-state data for flow through wet, packed fiber beds. For the case of flow through dry, packed fiber beds, however, advancing front technique measurements were significantly higher.

Foley and Gutowski (24) looked at the changes in fluid properties causing fundamental changes in fluid flow during the mold filling of carbon and Kevlar fabrics. Properties examined included viscosity, surface energy, and wetting angles. Their work supported the claim of (17) that the permeability of a dry preform was higher than for a saturated preform. It was postulated that this could be due to channeling of the resin during mold filling as it seeks preferential paths throughout the preform.

Weideman (25) examined the effect of stitching and preform thickness on permeability. The same conclusion reached by Hammond (23) was determined for stitching; it greatly enhanced the transverse permeability by providing low-resistance pathways. There was no effect on permeability due to thickness.

Adams et al. (26) made permeability measurements on several woven and non-woven fabrics using in-plane flow of an epoxy resin. The woven structures with large pores displayed larger permeabilities. The non-wovens exhibited a decrease in permeability with decreasing porosity. In addition to characterizing the flow properties of composite reinforcement materials, it was suggested that this technique could be used as a quality control test for fabric-to-fabric variations.

Lam and Kardos (27) found that, as alternating layers were laid down at higher off-axis angles, both the transverse and in-plane permeabilities decreased with the 0°/90° lay-up having the lowest values. They also found a similar conclusion to that of Weideman (25); for unidirectional preforms, the bed thickness had no influence on the permeability. The major conclusion by Lam and Kardos, however, was that the permeability of fiber beds is highly anisotropic, and errors will result if this is overlooked in predictive modeling efforts.

Kim et al. (15) investigated the in-plane flow through fiber reinforcements for different ply orientations. It was determined that 0°/90° cloths had higher permeability values than random placed fiber mats. When the number of 0°/90° layers was increased, for fiber volume fractions less than 0.45, there was an increase in the number of interlaminar pores. These pores resulted in higher permeability values. The permeability was also found to increase as the flow rate increased due to fiber movement. Wetted materials again showed lower permeability values compared to dry materials.

Molnar et al. (28) found that permeability values were higher for bidirectional mats than for random mats at the same fiber volume fraction. In-plane permeability was shown to be isotropic for plain weave, carbon mats and random, glass mats for porosity values less than 0.5 (29). The bidirectional glass mats were anisotropic in nature, and increased in anisotropy as porosity decreased.

Adams and Rebenfield (30) examined the effects of preform homogeneity and surface undulations on the in-plane permeability. It was determined that, in heterogeneous preforms, the permeability increased when a high-permeable layer was placed closer to the center of the preform than at the edge. This was attributed to a pressure gradient in the transverse permeability that was generated as the fluid moved from high to low permeable regions. The study on the surface undulations showed that as the number of layers increased for the woven preforms, the permeability increased because the surface undulations were unable to be compressed completely, yielding more flow areas. The preforms with minimal undulations (non-wovens and unidirectionals) had no change in permeability with thickness.

When looking at the advancing front technique, the capillary pressure must not be overlooked. Several researchers have focused on the one-dimensional form of Darcy's law with the capillary pressure at the flow front (14, 15, 24, 31). Gebart (14) was the only one that included porosity in calculating the permeability. Ahn et al. (16) derived an expression for the capillary pressure based on the porosity and a parameter they called a

Form Factor. This factor depended on the fiber alignment and flow direction, which was often measured experimentally.

The in-plane permeability measurements of various fabric reinforcements were carried out by Wang et al. (32) using two different techniques. A radial flow visualization technique, based on the work of Adams et al. (33), was used to determine the principal permeability axes. This technique showed the flow front progression as an ellipse. For a fully developed ellipse, the ratio of the length of the minor elliptic axis to the length of the major elliptic axis was equal to the square root of the ratio of the permeability in the major principal direction to the permeability in the minor principal direction. Once the principal axes were known, the one-dimensional form of Darcy' Law was used to determine the principal permeabilities in a unidirectional flow measurement technique. Although this unidirectional technique was more difficult to implement than the radial technique, it could account for edge effects that are prevalent in RTM. It was recommended that both techniques be used to accurately determine permeability values for fabric reinforcements.

The permeability values for VARTM applications can be complicated because of the resin flow in the preform, the high-permeable distribution medium, and the peel-ply. Sun et al. (34) measured the permeability as it pertains to VARTM applications. The radial flow technique was used to measure the in-plane permeability of the preform under constant flow rate conditions. There was some difficulty in directly measuring the transverse permeability of the reinforcement. Therefore, the transverse permeability was back-calculated from the comparison of three-dimensional model simulations and experimental measurements of the inlet pressure at a constant flow rate. The high-permeable distribution medium was constructed of a knitted fabric with a high porosity, and it was assumed isotropic. Due to the assumption of an isotropic material, only in-plane permeability was measured. Because of the low pressure drop in this medium, a flow visualization/analytical technique was employed to measure the in-plane permeability. Values of the square of flow length vs. time were plotted, and the permeability was calculated based on Darcy's Law. Due to the low permeability of the peel-ply, there was a large pressure drop across it in the thickness direction. This made it extremely difficult to measure. Thus, the transverse permeability of the peel-ply was determined analytically from the mold simulation program using a best-fit approach. The in-plane permeability was assumed to be that of the preform.

Sun et al. (34) found that the high-permeable distribution medium was essential in reducing mold filling time by a factor of seven. The peel-ply was also found to decrease mold filling time because it decreased the nestling effect of the high-permeable medium. The nestling effect was defined as the reduction of porosity due to the inlay of material between adjacent layers.

In flow visualization of the process, it was found that near-plug flow was observed at the top and bottom of the preform (34). There was also a lead-lag due to the permeability difference in the high-permeable distribution medium and the preform. Although this difference was nearly 50 times, the lead-lag was only about 6 cm, and remained virtually constant throughout processing (34).

2.2 Resin Transfer Molding

Most of the current VARTM technologies are low-cost variations of the RTM process. An understanding of the modeling efforts produced in the RTM arena is essential in both the comprehension and modeling of the phenomena associated with VARTM. Therefore, a summary of the most pertinent RTM modeling literature is presented here.

A finite element simulation of the RTM process using the Flow Analysis Network (FAN) with 1-D, 2-D, and 3-D element types was presented by Phelan (35). With this model, 2.5-D geometries and 3-D flows were examined. The finite element simulation predicted the pressure distribution in the preform during mold filling and the flow front position as a function of time.

Fracchia et al. (36) developed a two-dimensional mold filling simulation that was an extension of the work by Osswald and Tucker (37) involving Darcy's Law and the finite element/control volume (FE/CV) technique. The simulation predicted resin pressures and velocities during an isothermal, non-reactive filling. Experiments showed the simulation was accurate in predicting the fill patterns for thin, two-dimensional mold cavities.

A two-dimensional, FE/CV technique was employed to model the flow front of a fluid through an anisotropic preform (19-21). The simulation predicted the movement of a free-surface flow front in a thin-shell mold of arbitrary shape and varying thickness. The permeabilities were allowed to vary in magnitude and direction throughout the porous medium. The results were found to be satisfactory for a Newtonian fluid.

Bickerton and Advani (38) compiled a library of experimental flow visualization and pressure data for two-dimensional, isothermal RTM. A complex, five-sided mold was designed that utilized a variety of injection and venting sites and pressure measurements. Race tracking data and the dependence of injection pressure on preform fiber volume fraction data were examined to validate codes.

A two-dimensional flow model using the FE/CV technique and a three-dimensional heat transfer model was created by Lee et al. (39) to predict flow fronts in RTM and Structural Reaction Injection Molding (SRIM) processes. Young (40) took this progress a step further by developing a three-dimensional, non-isothermal mold filling simulation. Heat transfer, resin cure kinetics, and viscosity were included in this model. Flow and cure simulations were performed for a cube and T-shaped RTM preforms.

A two-dimensional, computer model was developed by MacRae (41) for the simulation of Resin Film Infusion (RFI) and RTM processing. This model calculated the resin infiltration, resin viscosity, resin advancement, heat transfer, and preform compaction. A FE/CV technique was implemented using Darcy's Law for flow through porous media. Heat transfer was based on a transient finite element model, which included the effects of convection on the tooling surface. Verifications of the model were performed by comparing with data obtained in the literature and generated experimentally. This model was proven to be effective, and showed promise for future work.

Verification of MacRae's (41) finite element model for the RTM process was performed by Hammond (23). This work used the FE/CV technique to determine the pressure at the inlet, along with the total infiltration time. The inputs to this model were the resin (kinetic and rheological) and preform (compaction and permeability) properties. Fits to data were used to relate fiber volume fraction to compaction pressure, and to correlate permeability to fiber volume fraction. The model successfully predicted the resin flow front position, the total infiltration time, and the rise in the fluid pressure at the inlet for a two-dimensional, RTM process.

MacRae's (41) RTM process simulation model was also verified by Fingerson (9). Techniques were developed to measure permeability values of preforms, and these material parameters were used as inputs to the model. Along with the permeabilities, the compaction data and the cure kinetics and viscosity of the resin were also important inputs. For a plain, biaxial weave, glass fabric and a stiffened, carbon preform, satisfactory results were obtained for the two-dimensional model.

Caba (42) developed and verified a three-dimensional model that incorporated resin flow through an anisotropic, carbon preform, heat transfer within the tool and preform assembly, and cure kinetics and viscosity of the resin for RFI/RTM. The model predicted the resin pressure distribution, the flow front location of the resin, the thermal profiles in the preform and tooling, and the degree of cure and viscosity of the resin. The governing differential equation for the flow model was based on Darcy's Law, and solved by the FE/CV technique. The heat transfer model was based on a three-dimensional, transient heat conduction equation, including heat generation. Isothermal, non-reacting flow was simulated in a single, blade-stiffened carbon composite panel. Non-isothermal, reactive flow was simulated in a stepped panel and a double, blade-stiffened carbon composite panel. Flow front predicted times were within 5-15% of the measured times for all three panels.

Calhoun et al. (43) used a two-dimensional model to simulate a RTM process that included a reactive resin. The model was developed by part of the research team at The Ohio State University, while the experimental design was developed by the other part of the team at The Dow Chemical Company. Analytical solutions for fluid flow, computer simulations of mold filling, and experimental verifications of the model were all compared in this study. Although the analytical solutions matched the computer simulations well, scaling factors were needed to match the experimental data. The scaling factors for the pressures were necessary to account for the local permeability variations that were possibly due to fabric deformation at high injection pressures.

A FE/CV technique was implemented to simulate the non-isothermal mold filling and cure reaction in RTM (44). Close agreement with experimental results was found for the filling patterns of a two-dimensional, thin-mold cavity. A three-dimensional simulation of an automobile bumper was also performed to show the practicality of the model for use in industry.

The use of the FE/CV technique to model isothermal flow in SRIM/RTM applications was performed by Gauvin et al. (45). Several experiments were performed where the mold was partially filled and allowed to cure in order to verify the location of the flow front. The model did not perform well in the corner areas of the mold. This was attributed to the difficulty in predicting the corner permeability. It was postulated that the inertial and friction forces may play a larger role than once thought in the modeling of higher speed injection processes.

Yousefi et al. (46) performed a one-dimensional simulation of the RTM process. Transient heat conduction and cure kinetic equations were solved simultaneously using the Galerkin finite element method. Gauvin and Trochu (47) discussed several issues in regards to liquid composite molding. Among these were permeability measurement, edge effects, flow in multilayer preforms, and non-isothermal filling. Experiments were compared against numerical solutions provided by RTMFLOT finite element software.

RTMFLOT software differs from traditional FE/CV techniques because non-conforming finite elements are used with a fixed triangular mesh to numerically solve equations. With this technique, it is no longer necessary to generate a control volume around each node. In the FE/CV technique, results are not accurate at the interface because the flow rates entering and exiting the control volume are averaged. Since these areas can have significantly different permeabilities, errors will result. A refinement of the mesh at the interface is prudent in the use of the FE/CV technique. The two main advantages of RTMFLOT are a precise local conservation of resin mass and no requirement to refine the mesh near the interface of two materials with varying permeabilities (47).

The effect of transverse inhomogeneities of two different materials was examined using RTMFLOT (48). Electrical wires were used to detect the flow front in the materials. In-plane and transverse permeability data were then used as input to the finite element code. This code accurately predicted the flow front shape, therefore, showing the importance of the transverse permeability on multi-layer preforms.

Friedrichs and Guceri (49) implemented a hybrid two-dimensional/three-dimensional technique to predict flow fields in a three-dimensional part. The three-dimensional aspect of the code was only used where all three components of the velocity vector needed to be solved. The two-dimensional section was put into use everywhere else. The governing equations were solved using a boundary-fitted coordinate system, coupled with the finite difference method. Results for a three-dimensional flow field of a Newtonian fluid were presented.

The flow modeling of thermoset injection molding was examined by Chiu et al. (50). The accuracy and efficiency of four different FE/CV approaches were compared. It was shown that the one-point upwind scheme, two-point upwind scheme, mixed upwind scheme, and exponential scheme all produced unsatisfactory results. Therefore, a Eulerian (FE/CV) - Lagrangian (tracer particles) approach was presented. Results from an isothermal, unidirectional mold filling problem with a chemical reaction showed that the Eulerian - Lagrangian approach provided the most accurate results.

Ismail and Springer (51) created an interactive finite element code that allowed variations of the inlet/outlet parameters and the flow rate during a single run. This interactive approach allowed the user to try several variations per run which eliminated the time expenditure normally required by completing several single runs using different parameters. Their model was successful in calculating the resin flow, temperature profiles, degree of cure, and viscosity of resin inside the preform.

One of the greatest problems in RTM comes from the surface quality of the parts produced. The "read-out" effect, where fibers are seen at the surface, and pinholes are two of the greatest problems (52). Pinholes are caused by microscopic air bubbles that can be trapped from the differences in permeability causing an uneven flow front. The work of Michaeli and Dyckhoff (52) showed that optimizing the flow front velocity can aid in reducing these pinholes. They also showed that increasing the mold cavity pressure could significantly reduce pinholes. The air content was then further reduced by the injection of acetone into the cavity prior to injection.

Air entrapped during RTM mold filling leads to void formation. Chui et al. (53) found many factors involved in void formation. Among these were: fill rate, capillary number, contact angle, resin-fiber wettability, preform characteristics, and the location of the inlet/outlet ports.

Dry spots are a common void formation where a dry area results because of the inability of the resin to infiltrate a particular region of the preform. A computational approach to predict the filling time and vent locations, or dry spots, was presented by Chen et al. (54). It required, for most cases, the solution of two linear equations. This simplistic mathematical approach eliminated lengthy computational times, and it was successful in the prediction of the last filling point. The results from this method were compared against earlier results of complete mold simulations by the FE/CV technique, and found satisfactory.

Young and Chuang (55) examined edge effects in the fabrication of T-shaped structural composites by RTM. It was found that when vacuum was applied to the mold, many dry spots were reduced, but not eliminated. It was also determined that sealing off of some of the preform edges resulted in less air enclosure, while still taking advantage of the remaining flow channels to hasten mold filling.

The edge effect in RTM was examined using a finite element code by Young and Lai (56). An equivalent permeability was defined, based on the size of the edge clearance, to model the flow in the channel. This edge flow model was used in combination with an existing flow model without altering the previous mesh.

The fluid flow in preforms may occur at different scales depending on the complicated preform architecture. In the region close to the flow front, tow impregnation causes a lag in the macroflow (flow outside the fiber tow). Therefore, some researchers focus on the microflow (flow inside the fiber tow) as well as the macroflow. Using one layer of unidirectional woven fabric, Binetruy et al. (57) found that the microflow can be neglected in a saturated preform. Close to the flow front, however, the micropores are transversely filled by the microflow resulting in a macroflow lag. A new boundary condition at the tow surface was proposed to account for the interaction between these two flow scales. A model was then developed that predicted the velocity drop from the tow transverse permeability and the macropore permeability during a constant pressure injection process. The difficulty in this model came from measuring the transverse permeability of the tows. It was also observed that tow impregnation had a significant effect on the overall permeability of the preform, especially for higher fiber volume fractions.

Another model was proposed that looked at the axial flow of the resin in tow impregnation under constant pressure conditions (58). It was found that, in most RTM cases, the axial flow can be neglected because the majority of tow impregnation comes from transverse flow. Void formation was also included in this model with two void mechanisms studied experimentally. One of the void mechanisms was due to the difference between the transverse velocities of separate macroflows outside of the tows. When these macroflows joined together, air entrapment often occurred. The second void mechanism was due to the coalescence of microflows at the fiber level inside the tows. These microflows also caused air entrapment by joining together at the fiber surfaces.

A two-dimensional flow model was developed to study flow in both the microflow and macroflow region (59). A control volume/finite difference method was employed to track the flow front by solving the Darcy's Law governing differential equation. At low filling rates, the capillary force needed to be included because it was the major driving force for the lead-lag of the microflow over the macroflow. The capillary pressure was calculated based on the method of Ahn et al. (16), which follows in the next section, and the contact angle was assumed to be zero, i.e. perfect wetting.

2.3 Capillary Effects

The contact angle is used as the accepted measure of wettability, with a low contact angle equivalent to good wetting. In association with the contact angle, the surface tension of the resin is a critical parameter in impregnation. Polymers with high surface tensions prove to be difficult in the production of a void-free composite. The contact angle and surface tension can be related to the capillary pressure. This pressure can often be the major driving force that can improve wet-out in low-pressure processes. The capillary pressure is the difference in pressure across the interface between two immiscible fluid phases. These phases jointly occupy the interstices of a porous medium because of the interfacial tension between them. If adhesive forces between the liquid and solid exceed the cohesive forces of the liquid, capillary rise will occur. Barrer (60) considered the flow through a single capillary to compare the magnitude of surface tension versus hydrostatic force, as a function of capillary radius. He concluded, for narrow capillaries, that the surface tension forces were comparable with the hydrostatic forces. Therefore, the capillary pressure must be taken into account given certain preform architectures and low-pressure injections. The capillary pressure is only one component of the total pressure of the system. The other pressure components are mechanical (including vacuum) and gravitational.

Ahn et al. (16) simultaneously measured the capillary pressure and advancing front permeability in woven fabric preforms. The capillary pressure, P_c, was also calculated based on a modification to the Young-Laplace equation (61) as:

$$P_c = \frac{4\gamma_{lv}\cos\theta}{D_e} \tag{2.4}$$

where, γ_{lv} is the surface tension between the resin and surrounding vapor, θ is the contact angle, which depends on the topology, surface chemistry, and the kinetics of the experiment, and D_e is the equivalent diameter of the pores, which is the capillary diameter for a single cylindrical pore. Furthermore, the anisotropic complexities of the preforms were combined into a dimensionless form factor, F, which depends on fiber alignment and flow direction (16):

$$P_c = \left(\frac{F}{D_f}\right)\left(\frac{1-\phi}{\phi}\right)\gamma_{lv}\cos\theta \tag{2.5}$$

where, D_f is the diameter of a single fiber filament. In unidirectional preforms, $F = 4$ for flow along the fibers, and $F = 2$ for flow transverse to the fibers. For complex architectures, F must be determined indirectly by measurements of the permeability.

The capillary pressure was measured experimentally for varying preform porosities. Based on these measurements, a form factor of 1.8 was calculated for the woven fabric architectures. The experimental data matched eq. (2.5) very well, especially at low porosities (16).

The advancement of fluid through a fiber preform is driven by two forces, capillaric and viscous. A convenient way of assessing the relative contributions of each force can be provided by dimensional analysis. The dimensionless parameter often used is the capillary number, which is the ratio of the viscous force to the capillary force:

$$C_a = \frac{\eta \upsilon}{\gamma_{lv}} \tag{2.6}$$

where, υ is the relative velocity of the resin as it passes the dry fibers. In general, the contact angle remains constant at low values of the capillary number, then increases as C_a increases.

Work by Young (59) showed that microflow (due to capillary pressure) leads macroflow at low flow rates, and vice versa for high flow rates. A critical capillary number (C_a ~ 0.1E-03 to 0.2E-03) was found where the micro- and macroflows were even, resulting in a uniform filling pattern. The critical capillary number was not dependent on the size of the fiber tow.

Dave (62) showed that process flow models, based on Darcy's Law, for autoclave processing, pultrusion, and RTM, are special cases of the same generalized theory. The model considered resin and porous media characteristics. Capillarity arose in RTM due to the injection of resin into an unsaturated preform. The effects of capillarity were accounted for by the capillary number.

The results of the Dave model (62) were presented by Dave and Houle (18). Darcy's Law was shown to be non-linear for an unsaturated region due to permeability variations during processing. It was deduced that capillarity needed to be taken into account. The surface tension and contact angle of the resin had to be considered in the calculations or differences in the permeability would result for different liquids. A modified capillary number was used:

$$C_a = \frac{\eta v}{\gamma_{lv} \cos \theta} \tag{2.7}$$

At small flow rates, the capillary forces dominated over the viscous forces, and the liquid proceeded to invade the capillaries. At higher flow rates, the viscous forces dominated, causing a back pressure at the inlet, and only the large capillaries were filled with resin.

Foley and Gutowski (24) determined that the advancing front permeability varied with fluid properties. Another modified capillary number was used as follows:

$$C_a = \left[\frac{S}{\left(1 - v_f\right)\gamma_{lv}}\right]\left[\frac{\Delta P}{L}\right] \tag{2.8}$$

where, $\frac{\Delta P}{L}$ is the pressure drop across the preform. A transition was found where the permeability did not remain constant but decreased. This transition was at a $C_a \sim 0.01$.

The effect of processing conditions on wetting was investigated by Patel et al. (63). Wetting was accomplished when the surface tension of the resin was less than the surface free energy of the fiber. Slower injection speeds and higher mold temperatures favored better bonding and wetting. Both of these aspects were reflected in higher tensile strengths. For single fiber composites, longer gel times equaled a stronger interface. It was also postulated that improper fiber sizing could hinder results.

Fingering at the flow front was observed in a unidirectional, stitched, glass mat (64). It was determined that the fingering was a result of the different permeabilities inside and outside the fiber tows. It was also found that fingering depended on the flow rate and the fluid properties (viscosity and surface tension). Therefore, the capillary number could easily show this dependency.

The strength and surface quality of parts manufactured by liquid composite molding is sometimes compromised due to the entrapment of air, which leads to void formation. Patel et al. (65) used high-resolution, video-assisted microscopy to observe in situ microvoid formation of a unidirectional, stitched, glass mat. Using the modified capillary number of Dave and Houle (18), they showed, for in-plane flow, microvoids formed at a C_a ~ 1E-03, and, for transverse flow, microvoids formed at a C_a ~ 1E-04.

At lower capillary numbers, the capillary force was larger than the viscous force, allowing the fluid to fill in the bundles instead of the larger gaps between bundles. This action produced macrovoids, which were removed by pushing more fluid through the system. As the capillary number increased, macrovoids decreased, but, above a certain number, microvoids formed. These voids were formed when viscous forces dominated over capillary forces causing the fluid to flow faster in the gaps between bundles than inside the bundles themselves. When these flow fronts met from opposite sides, voids formed (65).

Another void mechanism came about from the cross flow of the resin through the preform due to the penetration of the resin into the stitching paths. Eventually two microflows from each end met up to produce a microvoid. Microvoids are much harder to remove than macrovoids because they are trapped in the tows. The microscale flow behavior was determined to depend on the injection rate, the fluid properties, and the flow pattern (65).

The capillary interactions at low-pressure RTM injection was modeled using the body-fitted finite element method (66). The objective was to study the flow interaction between the microflow and the macroflow in RTM. Unidirectionally packed fiber mats with flow parallel to the fiber axes were examined. The properties of the fiber mats and the injection condition were found to influence void formation. The capillary driving force was a function of the contact angle, interfacial tension, porosity, and velocity of the flow front. This capillary force could not be neglected at low injection pressures because it resulted in void formation at the flow front by allowing the microflow to advance ahead of the macroflow.

The capillary force was determined by a modification to the Young-Laplace equation as:

$$P_c = \gamma_{lv} S_A \cos\theta \tag{2.9}$$

where, S_A is the surface area of the solid per unit volume of the fibers. θ was found to obey Tanner's Law (67) which states that the contact angle is proportional to the cube root of the capillary number $\left(\theta \propto C_a^{\frac{1}{3}}\right)$. The contact angle was calibrated from a set of known θ and C_a to form a basis:

$$\theta = \theta_{Basis} \cdot \left(\frac{C_a}{C_{a_{Basis}}}\right)^{\frac{1}{3}} \tag{2.10}$$

The contact angle was shown to vary during RTM processing due to the wetting of the fiber surface by the fluid, therefore, the free boundary condition was a function of the velocity of the flow front (66).

Hourng and Chang (68) developed a model for capillary flow along the edge of the mold in RTM of unidirectional glass mats. Using Darcy's Law and the body-fitted finite element technique, they found the critical gap size for inclusion of the capillary effect was $2\sqrt{S}$, where S is the in-plane permeability. Gravity was neglected when compared to mechanical, capillary, and vacuum pressure. Phelan (35) found the gravity term dominated the pressure balance for RTM at slow injection speeds where the resin flowed around the mold and then upward against gravity. He postulated that a venting point was needed at the top of the mold.

Batch et al. (69) measured capillary flow in both the longitudinal and transverse directions of continuous glass rovings. This was done with the capillary pressure only; no external pressure was applied. The capillary pressures measured were less than 10 kPa based on the measured contact angle, surface tension of the resin, and effective pore diameter (hydraulic radius). It was determined that low viscosity resins and low injection speeds should be used to minimize voids, but this resulted in slow production speeds.

A two-dimensional model for the transverse impregnation of resin into continuous, unidirectional glass bundles was presented by Chang and Hourng (70). This model took into account both the microflow inside the fiber bundles and the macroflow around the bundles using the body-fitted finite element method and Darcy's Law. Their model showed that the application of vacuum could significantly reduce voids.

2.4 Vacuum-Assisted Resin Transfer Molding

Conventional RTM has seen tremendous growth over the past few years. This growth has led to several variants of the traditional process. A detailed list of the more prominent variations used today can be found in Reference 71. Of these processes, VARTM is the most prevalent in industry due to its low-void-content products. An overview of the current VARTM literature is presented here.

Resin pressure distributions and flow front advancement were predicted in autoclave-assisted RTM (ARTM) by Kim et al. (29). Darcy's Law and the FE/CV technique were used in the evaluation of this improved RTM process. The mold-filling pressure and consolidation pressure were effectively controlled by the autoclave. A smart spacer was placed between consolidation plates to ensure consolidation after mold filling. The role of the smart spacer was to maintain an appropriate gap between the top and bottom platens during the filling stage, providing high void volume of the preform for an effective resin filling. Polyethylene (PE) and polyetheretherketone (PEEK) were the materials used as smart spacers.

Pike et al. (72) developed a VARTM process as a low-cost method for manufacturing structural laminates with integrated armor for ground combat vehicle hulls. This technique co-cured epoxy prepregs, ceramic armor tiles, and liquid resins in a single elevated temperature cure cycle. VARTM resulted in a 21% unit cost savings. The resins used for this VARTM process met the structural design requirements, and had typical ballistic penetration resistance when compared to traditional manufacturing methods.

The main disadvantage with the VARTM process is in the low fiber volume fractions achieved. One way to get around this limitation is by using stitching and debulking methods which result in near-net-shaped preforms that need little or no further compaction during processing (73-74). Another way is by improving existing VARTM techniques. The Seemann Composites Resin Infusion Molding Process (SCRIMP) was developed by Bill Seemann of Seemann Composites (75-80). This process has taken VARTM to a new level by allowing rapid impregnation of composite surfaces, followed by an infusion in the composite thickness direction. This allows for very large and high fiber volume fraction composites to be produced. The main feature that is different from VARTM is in the patented resin distribution systems. These distribution systems incorporate the injection/vacuum ports, the resin distribution medium, and the vacuum bag tool surface into one part which allows for high-quality, rapid impregnation of preforms.

The Department of Energy and Johns Hopkins University Applied Physics Laboratory developed a high-pressure compressed natural gas storage unit called the Integrated Storage System (ISS) (81). The ISS consists of two mating shells, which contain three filament wound cylinders for carrying natural gas and a removable valve cover that protects the valve plumbing. The mating shells and the removable valve cover were fabricated using SCRIMP. RTM, VARTM, filament winding, pultrusion, and SCRIMP were all considered for the manufacturing, but SCRIMP was chosen based on quality and cost considerations. The ISS container and protective cover were successfully manufactured by SCRIMP, and the components met all design requirements and testing standards.

The US Navy conducted a demonstration program to evaluate design and fabrication issues of composite structures (82). The four processes evaluated were: UV-VARTM (VARTM with ultraviolet resin), UV-Prepreg (consolidation using ultraviolet resin and no vacuum bag), LTC-Prepreg (consolidation using a low-temperature cured prepreg and no vacuum bag), and SCRIMP (using a catalyst cured resin system). Four one-half scale, midship sections of a medium-sized, 85.3 m, 1,089 metric ton vessel were fabricated using alternative low-cost processes with low VOC emissions. Exceptional quality was obtained for the SCRIMP hull section when compared to the other techniques. The resulting product weighed slightly under 10,442 kg, and took approximately 3,154 man hours to manufacture.

The U.S. Army has shown interest in the development of light-weight, short-span, mobile assault bridging using low-cost, SCRIMP fabrication techniques. The development of the all-composite assault bridge (CAB) has been undertaken by Kosmatka et al. (83). The CAB uses a two parallel treadway design, 14.0 m long, 1.5 m wide, and 0.6 m deep. The main structural component of the treadway is an open-bottom, W-shaped design with 2.97 cm thick, stitched, unidirectional graphite on the lower-most surface, and stitched (± 45/90) graphite on the vertical and angle mounted side-walls. The stitching provides pathways for the resin in the SCRIMP process. Because of the need for high strength at higher operating temperatures (49 °C), oven-cured epoxies were used.

Finite element analysis of a single CAB treadway was performed using NASTRAN (83). The global model consisted of 22,000 elements and 28 different property sets. Two different vehicle loads, at three different positions, were considered with three different boundary conditions (level, uphill, and twisting). Under the worst case, the maximum center span deflection was 8.89 cm. The weight of the bridge was also calculated to be 4,086 kg based on finite element data, which is a 75% weight reduction when compared to traditional metallic bridges. This translated into a 20% cost reduction.

The results of the first full-scale static test of a composite bridge treadway was presented (84). SCRIMP was determined to be a viable manufacturing process for the CAB treadway based on the quality of components. The failure was determined to be caused by poor bonding during fabrication.

Hardcore Composites evaluated several SCRIMP-processed, glass-fiber-reinforced plastic (GFRP) bridgedeck structures based on four configurations (85). These configurations were triangular, trapezoidal, cubic, and balsa decking. The triangular, trapezoidal, and cubic configurations consisted of foam shapes with a variety of fabrics individually wrapped around them. The balsa deck consisted of a balsa core with fabric wrapped around it. Since the span to depth ratio was 8:1 or greater, the stiffness and bending strength could be attributed to the face skins. All four of the sandwich structures tested had the same skin material and lay-up. Therefore, the difference in the configurations was evaluated based on the highest shear strength achieved per dollar of manufacturing cost. It was determined that the most cost-efficient design was a function of the support configuration and deck size. Triangular and trapezoidal web sandwich decks were best in one-dimensional, beam-like support configurations. The cubic was most efficient for two-dimensional support configurations, while the balsa was the best overall. The balsa core structure was not cost-effective, however, when the structure was scaled up to the size of the Delaware River and Bay Authority Magazine Ditch Bridge.

Hardcore Composites recently installed a SCRIMP-manufactured, 12,712 kg bridgedeck in Mill Creek, Delaware (86). This bridge was 5.2 m wide, 11.9 m long, and 22.86 to 25.40 cm deep. The structure consisted of complicated fiberglass skins and foam cores, and it required two days to lay-up. Infusion with a vinyl ester resin took four hours, followed by a four hour gel and a 12 hour cure. The deck was then deflashed, and coated with a concrete surface finish. The traditional installation time of 90 days for bridges was cut in half by using the composite bridgedeck. This faster installation time was accomplished by manufacturing the new bridgedeck off-site, while the demolition of the old bridgedeck and preparation was finished at the bridge-site. Once the preparation was complete, the new bridgedeck was set in place within an hour. The largest bridgedeck built to date by Hardcore is a 749 m^2 deck that is in operation in Ohio.

Along with performance, economics often play a key role in the implementation of composites in civil infrastructure. Although the initial cost for composite bridgedecks is comparable to traditional bridges, two factors point to a greater savings over the long run. First, these types of composite bridges are designed to last for 75 years, while a traditional reinforced concrete bridge is estimated to last only 30 years. Second, existing foundations are usually used without significant repairs due to the reduced payload of the new bridgedeck. Therefore, once the low maintenance and long life cycles are factored in, these bridges are clearly the better economical alternative.

The U.S. Navy has documented that the cost of SCRIMP processing is one-tenth of the previous cost for aircraft-quality parts (87). The mechanical properties rival the traditional prepreg or wet lay-up with autoclave cures. 12.8 m half-hulls have been manufactured by trial-and-error methods at The Hinckley Company in Maine. It is more of an art than a science at this time. SCRIMP processing has reduced VOC emissions by 90%, which has been a saving grace in times of stricter EPA regulations on hazardous chemical regulations.

Sun et al. (34) used a three-dimensional, FE/CV method to predict the mold filling time of SCRIMP based on a high-permeable distribution medium. It was found that the permeability of the high-permeable medium had a much more significant influence on the mold filling time than the fiber preform. It was assumed, for large differences in permeability, the in-plane flow of both the peel-ply and the preform could be neglected. Based on this assumption, a two-dimensional, resin leakage model for the high-permeable distribution medium was proposed. In this model, the resin fills the high-permeable medium and then “leaks” into the fiber preform which acts as a resin sink. This simplified model greatly reduced the computational time required by the 3D FE/CV simulation, yet provided a reasonable estimation of mold filling time.

Ni et al. (88) took a similar approach to that of Sun et al. (34) for the case of SCRIMP based on grooves. In this process, grooves are cut into a low-density core, which becomes a part of the final product. These grooves enable faster infiltration times due to their higher permeability values, and eliminate the need for a high-permeable distribution medium and peel-ply.

Mold filling times in SCRIMP based on grooves yielded faster infiltration times than those based on a high-permeable distribution medium. A resin leakage model similar to Sun et al. (34) was also implemented. This model was a one-dimensional simulation that provided a reasonable estimation of mold filling time while greatly reducing the computational time required by the 3D FE/CV simulation (88).

Other inventors have also developed similar VARTM-type processes. Le Comte (89-90) has proposed the use of a form-retaining inner mold and a resin delivery system. The resin delivery system consists of a foam core with a resin channel system as a part of the mold. The channels supply resin to the reinforcing fiber which is laid onto the mold surface. A flexible outer surface is then applied and a vacuum is introduced to cause the resin to flow through the channels of the foam strips.

The Navy Center of Excellence for Composites Manufacturing Technology has developed a low-cost, VARTM composite manufacturing technology for military applications (91). This new technique is a combination of Vacuum-Assisted Compression Molding and VARTM. The name of this process is Resin Injection Recirculation Molding (RIRM). A rigid outer tool is coupled with a flexible inner skin or a rigid inner tool. The tool is loaded with fiber and core material, a vacuum is applied, and then resin is pumped into the mold. The resin is allowed to flow out of the mold and into a resin trap. Once the trap reaches a particular level, the trap becomes the resin source and the prior resin source becomes the new trap. Thus, the resin is recirculated through the system, enhancing wet-out. This new technique reduces the cost of conventional open-mold, wet-lay-up fabrication, and allows for better process control.

Foley and Gutowski (24) have implemented a new technique called Flexible RTM (FRTM). In this process, a dry, fabric preform is placed between two elastomeric diaphragms, and a vacuum is used to assist the impregnation. The composite part is then formed into shape by utilizing the elastomeric diaphragms.

2.5 Summary

Darcy's Law is generally accepted as explaining flow through porous media. This law states that the superficial velocity of a fluid is dependent on the permeability of the porous medium, the viscosity of the fluid, and the pressure gradient across the porous medium. The permeability is defined as the property of a porous material which characterizes the ease with which a fluid may be made to flow through the material due to an applied pressure gradient

Several models have been developed to analytically predict permeability. This has proven to be extremely difficult due to the complicated architectures of many preforms. Therefore, several researchers have focused their efforts on empirically determining the permeability based on Darcy's Law. Important factors in measuring the permeability include the measurement technique, the anisotropic nature of the preform, the flow direction, and the fluid-surface interaction. There are two techniques commonly used for measuring the permeability of a preform. These techniques are referred to as the steady-state and advancing front techniques.

Capillary effects have been postulated to play a large role in the modeling of processes that require either low-flow-rate or low-pressure injections, such as VARTM. The major parameter involved in these effects is the capillary pressure. This pressure depends on the contact angle and surface free energies of the materials involved, and can often be the major driving force for wet-out in low-pressure processes.

The RTM process has been extensively modeled in the literature. Successful efforts have been recorded for three-dimensional, flow, heat transfer, and cure kinetics and viscosity models. Little has been done in the modeling of VARTM, however. Researchers have focused more of their attention on the actual development of VARTM manufacturing techniques rather than the predictive modeling. A great deal of work still needs to be done on efforts to reduce the costly trial-and-error methods of VARTM processing that are currently in practice today. A computer simulation model of the VARTM process would provide a cost-effective tool in the manufacturing of composites utilizing this technique.

Therefore, the objective of this research was to modify an existing three-dimensional, RFI/RTM model to include VARTM simulation capabilities and to verify this model with the fabrication of aircraft structural composites. An additional objective was to use the VARTM model as a process analysis tool, where this tool would enable the user to configure the best process for manufacturing quality composites.

Chapter 3 Preform and Resin Characterization

3.1 Permeability

The permeability is an important material property that is a required input for the computer model. Both the steady-state and the advancing front permeability measurement techniques were utilized in this work. Darcy's Law, eq. (3.1), is used as the starting point in the derivation of the necessary working equations for both of these techniques.

By prescribing a constant flow rate condition, q_o, the steady-state equations are derived as follows, for the principal permeability in the x-direction, S_{xx} (Assuming the material to be characterized is orthotropic, measurements must be made in three mutually perpendicular directions to fully characterize the preform.):

$$q_o = -\frac{S_{xx}}{\eta}\frac{dP}{dx} \tag{3.1}$$

For permeability testing, the resin viscosity and preform permeability are assumed constant, which allows the variables to be separated as follows:

$$q_o \eta \int_0^x dx = -S_{xx} \int_{P_o}^{P_f} dP \tag{3.2}$$

Integration of eq. (3.2) and rearranging gives an expression for the permeability in terms of measurable quantities:

$$S_{xx} = \frac{q_o \eta}{P_o - P_f} x_f \tag{3.3}$$

where, P_o is the inlet pressure, P_f is the outlet pressure, and x_f is the length of the preform. In this technique, the inlet pressure is allowed to vary in order to maintain a constant flow rate. Once the preform is saturated, the pressure differential across the preform is measured, and the permeability is calculated.

For the advancing front technique, a constant pressure or a constant flow rate condition may be defined. The following derivation is based on a constant pressure condition, P_o, and varying flow rate in the x-direction, q_x:

$$q_x = -\frac{S_{xx}}{\eta} \frac{dP}{dx} \tag{3.4}$$

There exists a relationship between the superficial and interstitial velocities, such that:

$$q_x = v_x \phi = \frac{dx}{dt}\phi \tag{3.5}$$

where, v_x is the x-component of the interstitial velocity vector, ϕ is the porosity of the preform, x is the wetted length of the preform, and t is the corresponding time. Combining eqs. (3.4) and (3.5) yields:

$$\frac{dx}{dt}\phi = \frac{S_{xx}}{\eta}\left(\frac{P_o - P_{flowfront}}{x}\right) \tag{3.6}$$

where, $P_{flowfront}$ is the pressure at the flow front. Rearranging eq. (3.6) and integrating:

$$\int_0^x x dx = \frac{S_{xx}}{\eta\phi}\left(P_o - P_{flowfront}\right)\int_0^t dt \tag{3.7}$$

gives the following expression for permeability:

$$S_{xx} = \frac{x^2 \eta\phi}{2\left(P_o - P_{flowfront}\right)t} \tag{3.8}$$

The porosity of the preform is related to the fiber volume fraction by the following equation:

$$\phi = 1 - v_f \tag{3.9}$$

and the fiber volume fraction is determined by:

$$v_f = \frac{\xi}{\rho_f t_p} \tag{3.10}$$

where, ξ is the areal weight of the preform, ρ_f is the density of the preform, and t_p is the thickness of the preform. The areal weight is determined by measuring the weight of the preform and dividing by the area to yield units of grams per square meter. The density of the preform is assumed to be the density of the fiber itself, which is provided by the manufacturer. In this technique, measurements are made as the resin infiltrates the dry preform, and they are stopped once the preform is saturated.

The permeability measurement system, for both the steady-state, constant flow rate technique and the advancing front, constant flow rate technique, consists of a real-time National Instruments data acquisition board, National Instruments SCXI signal conditioning and multiplexing hardware, LabVIEW data acquisition software running on a PC, and a Parker Zenith precision gear metering pump with a Zenith Zetrol control unit (9). A synthetic oil (η = 0.0345 Pa·s) was used as the infiltrating fluid for all permeability measurements.

Figures 3.1 and 3.2 show two of the permeability measurement fixtures that were used in this study. Figure 3.1 shows the in-plane steady-state and advancing front permeability measurement fixture. This fixture is equipped with five pressure transducers: one at the inlet, three beneath the preform, and a final one at the outlet. The sample chamber requires a preform 15.20 cm long and 15.32 cm wide. The test fluid flows through a narrow groove which is parallel to the face of the preform in order to ensure one-dimensional flow at the entrance of the preform. Figure 3.1 shows this fixture raised and ready to be loaded with a dry preform for testing.

Figure 3.2 shows the transverse steady-state permeability measurement fixture. This fixture was designed to test 5.1 cm square samples. In this photo, the upper section is to the left, and it is placed upside down. The lower section is to the right in the photo, and it is placed right-side up. For testing, this fixture is mounted in an Instron identical to the in-plane fixture shown in Figure 3.1. Once the fixture is mounted, the upper and lower sections of the mold compress the preform, and fluid is pumped into the mold cavity. This cavity contains holes that allow preform infiltration by the fluid in the transverse direction. Details of the permeability measurement fixtures, along with their respective measurement techniques, can be found in Reference 9.

Another permeability measurement fixture that was used in this work is shown in Figure 3.3. This fixture consists of a 121.92 cm long, 60.96 cm wide, open-faced, aluminum tool plate. Three 0 to 15 psia pressure transducers are located on 15.24-cm centers in the direction of flow, and one transducer is located on a 7.62-cm center from the middle transducer, perpendicular to flow.

This system is used to simulate VARTM processing conditions during advancing front permeability measurement with a constant pressure injection. It is used in a manner similar to the fixture in Figure 3.1, except a vacuum bag is used as one of the tool surfaces (not shown). Samples are cut 66.04 cm long by 17.78 cm wide for testing, and laid up in plies. Vinyl tubing, with five 3.175 mm diameter injection ports on 2.54-cm centers, is placed at one end, while a vacuum port is placed at the other end. Pressure, time, and flow front positions can then be recorded during infiltration, and used as input to eq. 3.8 to determine the permeability.

In-plane permeability measurements of both the warp and fill directions were performed for a 10-ply, glass fabric preform. The fabric used was an E-glass fabric manufactured by Clark-Schwebel (style 1523). It is a plain weave fabric that measures 0.3302 mm thick (92), and has a specific gravity of 2.58 (93). Three different permeability measurement techniques were implemented in order to determine the validity of using one technique versus another. The techniques used were:

1. Steady-state, constant flow rate, closed, steel mold (Figure 3.1)
2. Advancing front, constant flow rate, closed, steel mold (Figure 3.1)

3. Advancing front, constant pressure, open-faced, aluminum tool plate with vacuum bag (Figure 3.3)

The 1523 E-glass permeability measured by these techniques is shown in Figure 3.4.

These results show that there is no decisive advantage in using one technique over another. When each standard deviation of the permeability measurements was considered, all of the techniques showed an overlap within one standard deviation. Therefore, for fiber volume fractions ~0.50, the measurement techniques gave similar results. The steady-state technique, however, is the preferred technique due to its proven success and its ease of use (9). The steady-state technique was used to determine the in-plane principal permeabilities for all of the fiber systems. The transverse principal permeability was also determined by the steady-state technique, using the fixture shown in Figure 3.2.

In addition to the 1523 E-glass fabric, permeability data were obtained for several types of carbon fiber materials. The first type is a multiaxial warp knit fabric that contains seven layers of Tenax HTA unidirectional carbon fibers laid up in a quasi-isotropic stacking sequence. These layers are then knitted together with a polyester thread to form a "stack", which is taken to be an orthotropic material. Another type of carbon fabric characterized consists of stitched, triaxial-braided carbon fibers. The tows are braided around a cylindrical mandrel to form a tube with IM7 36k axial carbon fibers and AS4 6k carbon fibers at a 60° braid angle. The tube is then flattened to form a layer.

Preforms are constructed by stacking the above "stacks" or tubes together, and stitching the material in the through-the-thickness direction with Kevlar thread and a modified lock-stitch (center-lock or surface-lock). The preforms tested were 8-stack multiaxial warp knit, 4-tube center-lock braided and surface-lock braided, and 14-tube center-lock braided and surface-lock braided. The permeabilities were measured for three mutually perpendicular directions: parallel to the stitching, perpendicular to the stitching, and through the thickness. The results from all of the preform permeabilities measured are shown in Table 3.1.

The permeabilities of the high-permeable distribution media were also measured. Two high-permeable media were characterized. The first is a plain weave nylon screen with ~50% open area (Shown in Figure 3.5.). The second material is a hexagonal-shaped flow pathway manufactured by Seemann Composites. This medium is unique because the high-permeable medium is actually formed by cutting pathways into the vacuum bagging material. This enables the high-permeable medium and vacuum bag to function as one unit of continuous material (See Figure 3.6.).

Due to the high permeability of these materials, a new permeability measurement protocol had to be devised. A radial flow, advancing front technique with a center-port injection was first used to determine the orientation of the in-plane principal axes (32-34). In this technique, a 45.72 cm square sample is placed onto an aluminum tool plate with vacuum ports placed at the corners. The whole assembly is then sealed with a transparent vacuum bagging material. The tool plate has an air-tight injection port tapped in the center. This port allows the injection of an infiltrating fluid from beneath the tool plate and up into the high-permeable medium. Once the lay-up is finished, the vacuum pump is turned on to expel any air from the assembly. The infiltrating fluid then enters through the center-port and into the sample forming an elliptical flow front. The flow patterns are recorded by a video camera which allows for slow-motion visualization of the elliptical flow front. The major and minor axes of this ellipse coincide with the in-plane principal permeability axes of the material tested. Both the high-permeable materials used in this study were determined to be isotropic by forming circular flow patterns during radial infiltration. The infiltrating flow patterns perfectly overlapped circles of 15.24 and 30.48 cm diameters as the flow progressed outward from the injection port (These circles were drawn on the vacuum bag prior to infiltration with a black marker.).

Once the isotropic nature of each material was established, the in-plane principal permeabilities of the high-permeable distribution media were measured by the following one-dimensional advancing front technique. Samples of each material, 81.28 cm long and 15.24 cm wide, were tested with an oil absorbent material placed around the edges. Vinyl tubing, with four 3.175 mm diameter injection ports on 2.54-cm centers, was placed at one end, while a vacuum port was placed at the other end. The same synthetic oil used in the previous permeability measurements was used as the infiltrating fluid. The time for the infiltrating oil to travel the 81.28 cm distance was recorded to determine the permeability. The porosity values were determined by examining the geometry of media and calculating the ratio of the open cross-sectional area to the total cross-sectional area. For the nylon, the porosity was 0.51, and the permeability was measured to be 2.92 E-09 m^2. For the Seemann material, the porosity was 0.54, and the permeability was measured to be 3.45 E-09 m^2.

For these thin media, the transverse direction fills instantaneously as the fluid flows in the in-plane directions. This condition does not allow for any realistic transverse permeability measurements to be performed. Therefore, the transverse permeabilities were arbitrarily assumed to be approximately one order of magnitude higher than the in-plane values. The assumed transverse permeability, for both the nylon and the Seemann material, was 1.0 E-08 m^2.

3.2 Viscosity

The second characterization that is a necessary input for the computer model is the resin viscosity. There were three resins used in this study. The first was a room temperature cure, epoxy vinyl ester resin. This resin, Dow Derakane 510A-40, is 62% brominated vinyl ester and 38% styrene monomer, and has a specific gravity range of 1.17 to 1.22 (94). The curing agents consisted of a catalyst and a promoter. Cobalt napthanate (0.3 weight %) was the catalyst, and methyl ethyl ketone peroxide (1.25

weight %) was the promoter. When the resin was mixed using this formulation, gelation occurred in approximately one hour at room temperature. Another resin used was AroCy L-10, a dicyanate ester monomer with a specific gravity of 1.18 (95). The L-10 system used an active hydrogen initiator (2 weight % nonylphenol) and a catalyst (0.15 weight % of 8% zinc napthanate) to facilitate cure. The final resin was a cyanate epoxy with a 1.18 specific gravity (96). This resin, SC-36, was received in two parts, A (cyanate) and B (epoxy). The mixing ratio of both components was 1:1 by weight.

Viscosity measurements were performed using a Brookfield Model DV-III Concentric Cylinder Digital Rheometer. These results are displayed in Table 3.2. The DV-III drives a spindle, immersed in a test fluid, in order to measure the viscous drag of the fluid. All viscosity measurements were made isothermally at 10 RPM with readings taken every 30 seconds for up to an hour. The SC-36 resin cannot be injected at room temperature because of its high viscosity value (3.80 Pa·s). Therefore, in addition to room temperature isotherms of all resins, an elevated isotherm (43°C) of the SC-36 resin was performed.

3.3 Degree of Cure

Samples of all three resin systems were examined to determine the degree of cure for the composites after processing. Cure kinetics data were determined by Differential

Scanning Calorimetry (DSC), which measures the total heat of reaction for the resin system. In DSC measurements, the primary assumption is that the rate of heat generation is proportional to the rate of the cure reaction. The degree of cure can then be defined as:

$$\alpha(t) = \frac{H(t)}{H_R} \tag{3.11}$$

where, $H(t)$ is the heat evolved from the beginning of the reaction to some intermediate time, t, and H_R is the total heat of reaction during cure. These two quantities are defined as:

$$H(t) = \int_0^t \left(\frac{dH}{dt}\right) dt \tag{3.12}$$

$$H_R = \int_0^{t_c} \left(\frac{dH}{dt}\right) dt \tag{3.13}$$

where, t_c is the total time for the resin to cure.

Dynamic DSC data were obtained for the virgin L-10 and SC-36 samples in order to measure the total heat of reaction for each system. Both samples were subjected to a 10°C/min heating rate to a temperature of 350°C. The results are shown in Figures 3.7

and 3.8. In the case of the virgin 510A-40 system, the reaction proceeds much too quickly at room temperature for accurate total heat of reaction data to be recorded.

Residual dynamic scans were also performed on resin samples that were first subjected to their respective cure cycles. This was done to determine the heat of reaction that evolved during processing, which is equal to the difference between the total heat of reaction and the residual heat of reaction. All three resins were subjected to this residual scan. Results are shown in Figures 3.9-3.11.

Although Figure 3.9 does not provide a direct measure of the degree of cure for the 510A-40 resin system (because of the inability to obtain reliable total heat of reaction data), it does provide some insight into the incompleteness of the reaction. This data does show that a postcure may alleviate this residual, which is evident from the 47 J/g residual heat of reaction value. Relieving this residual would assure a higher degree of conversion, even though the actual numerical degree is unknown.

By using the dynamic DSC scans in Figures 3.7 and 3.10 and eq. 5.1, the degree of cure for the L-10 resin system was determined to be 0.95. Likewise, Figures 3.8 and 3.11 were used in conjunction with eq. 5.1 to determine the degree of cure for the SC-36 resin system. For this system, α was determined to be equal to 0.93.

3.4 Surface Tension and Contact Angle

The final characterization that needed to be performed was the surface tension and the initial contact angle for the 1523 E-glass/510A-40 system. This data is necessary for the capillary boundary condition that will be discussed in the next chapter.

The surface tension of the 510A-40 resin system was measured using a Cahn Dynamic Contact Angle Analyzer (DCA-322). This analyzer uses the Wilhelmy plate technique to measure both advancing and receding surface tensions. With the DCA-322, a glass plate is used to simulate a zero contact angle surface. This plate is then introduced to the resin system at a rate of 22 microns per sec (in 0.1 intervals) over a 10 mm distance with force measurements (due to the resin-glass interaction) taken every second. The force on the glass, F, is measured by a balance and related to the contact angle and surface tension by the following equation (22):

$$F = p\gamma_{lv} \cos\theta \tag{3.14}$$

where, p is the perimeter of the glass plate in contact with the resin-air interface. The receding surface tensions are of greater importance in determining the surface tension of an unknown system because the receding values allow for the zero contact angle assumption to be more accurate. For this resin system, the receding surface tension was determined to be 30.28 ± 4.49 dynes per cm using a linear least squares algorithm.

The contact angle of the 1523 E-glass/510A-40 system was measured using a Ramehart 100 Goniometer. A drop of the 510A-40 resin was placed on the 1523 E-glass fabric. A video camera was then used to zoom in on the resin-fiber interface. The video camera allowed the contact angle to be seen more clearly on a video monitor. The contact angle was easily measured with a special protractor-device located on the monitor. For this system, the contact angle was determined to be 30° ± 3°.

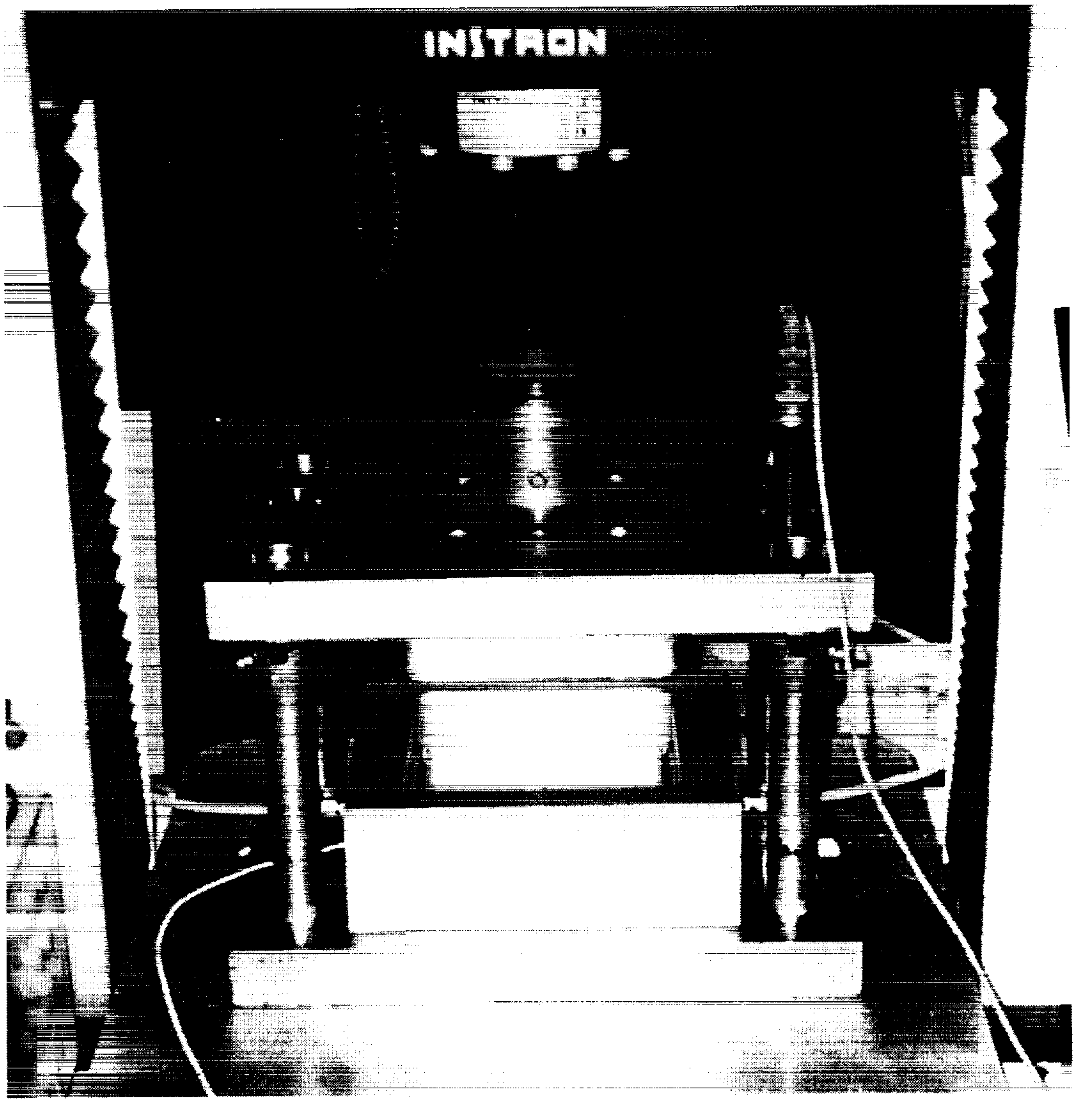

Figure 3.1 RTM In-Plane Fixture for Steady-State and Advancing Front Permeability Measurements

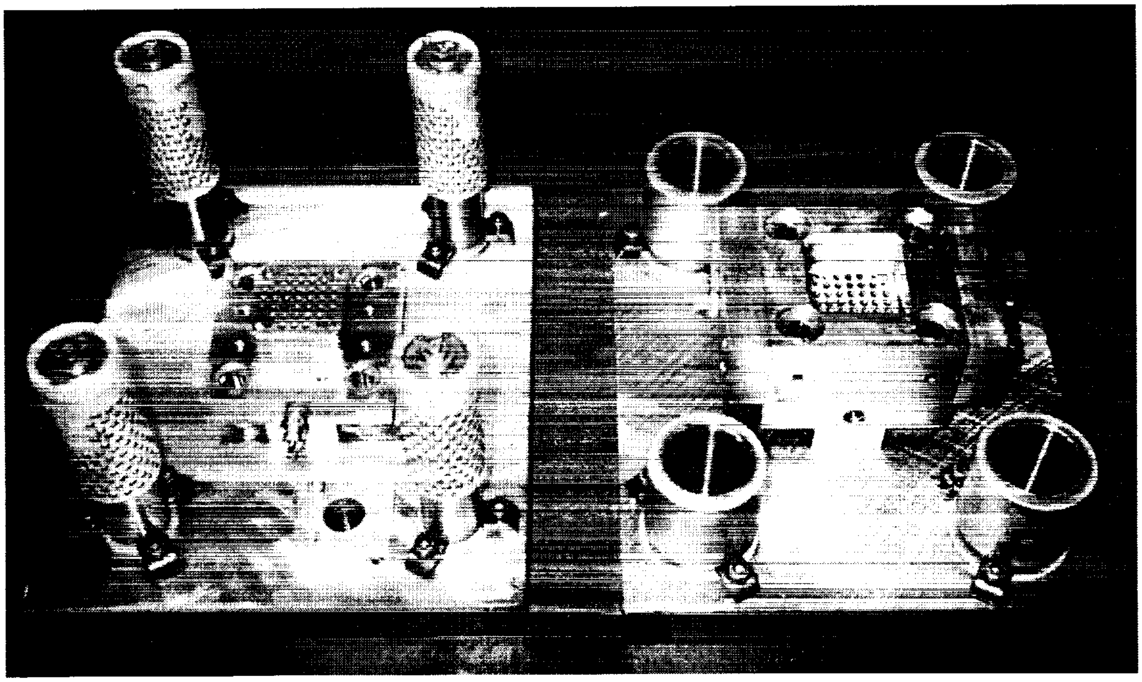

Figure 3.2 RTM Transverse Fixture for Steady-State Permeability Measurements

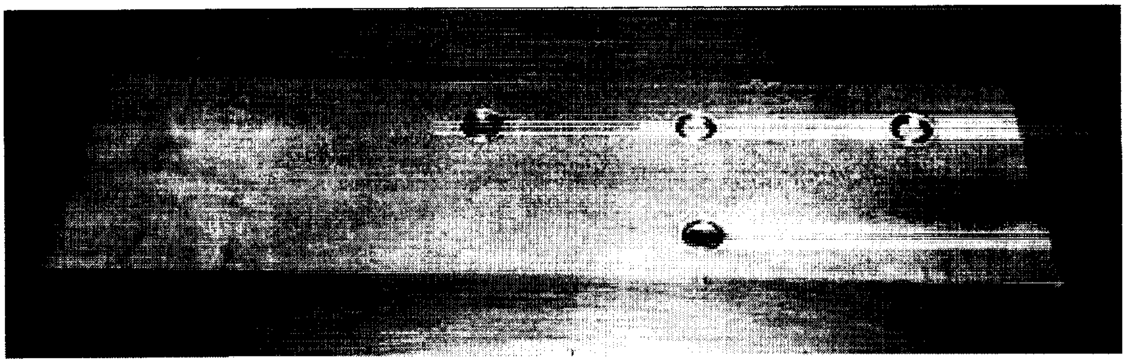

Figure 3.3 VARTM In-Plane Fixture for Advancing Front Permeability Measurements

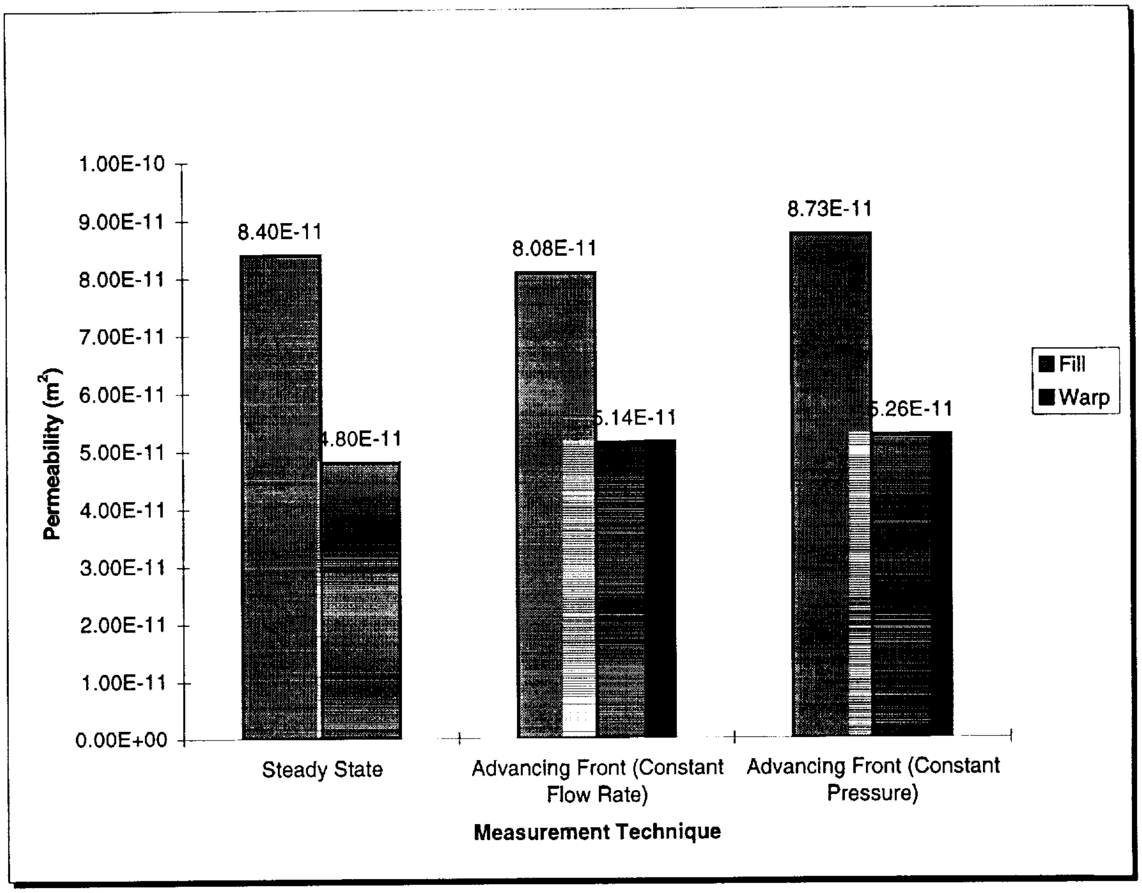

Figure 3.4 In-Plane Permeability Measurement Technique Comparison for 1523 E-glass at a Fiber Volume Fraction of 0.49

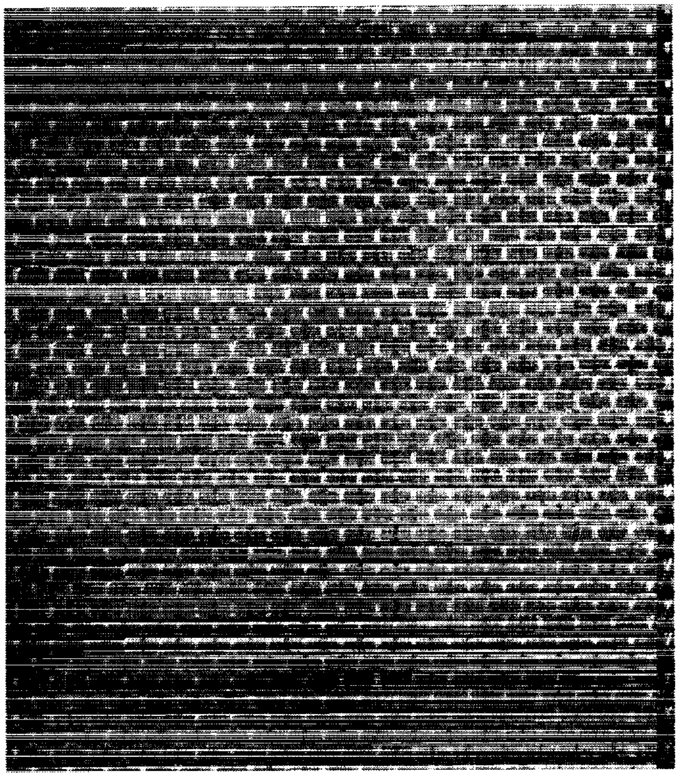

Figure 3.5 Close-Up of Nylon High-Permeable Distribution Medium

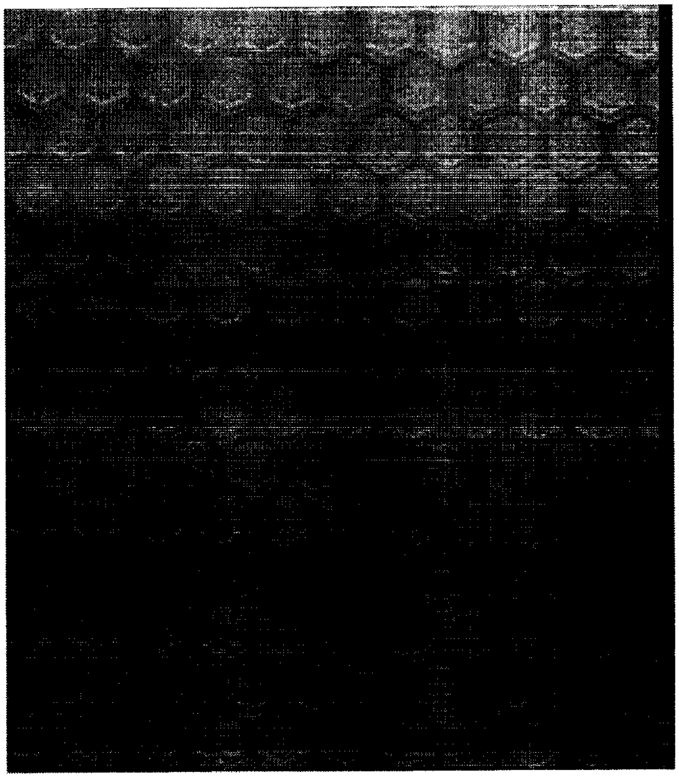

Figure 3.6 Close-Up of Seemann High-Permeable Distribution Medium

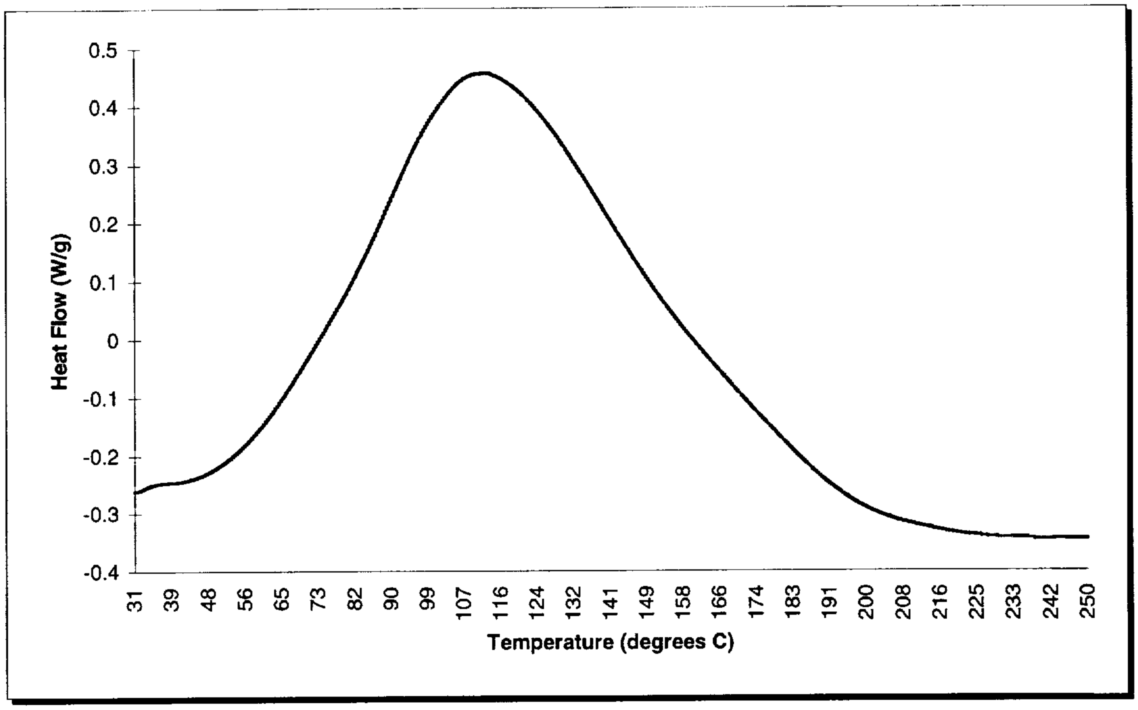

Figure 3.7 Dynamic DSC Scan of Virgin L-10 at 10°C/min from 25°C to 350°C

The total heat of reaction was 347 J/g.

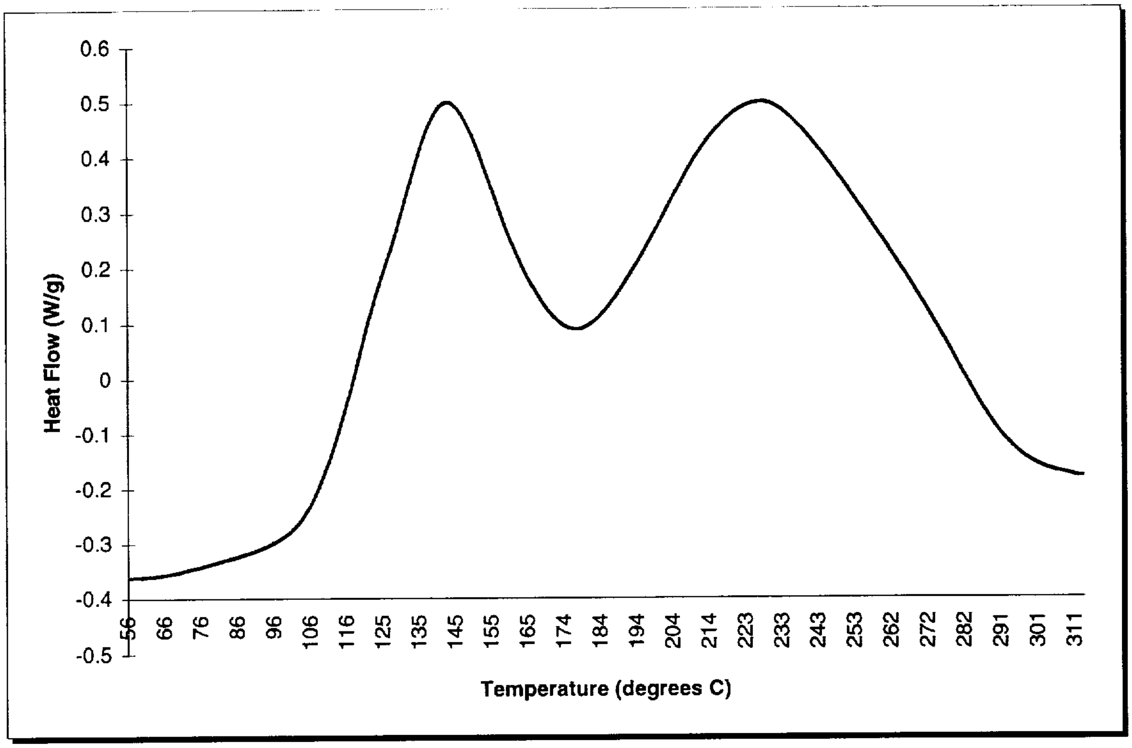

Figure 3.8 Dynamic DSC Scan of Virgin SC-36 at 10°C/min from 25°C to 350°C

The total heat of reaction was 573 J/g.

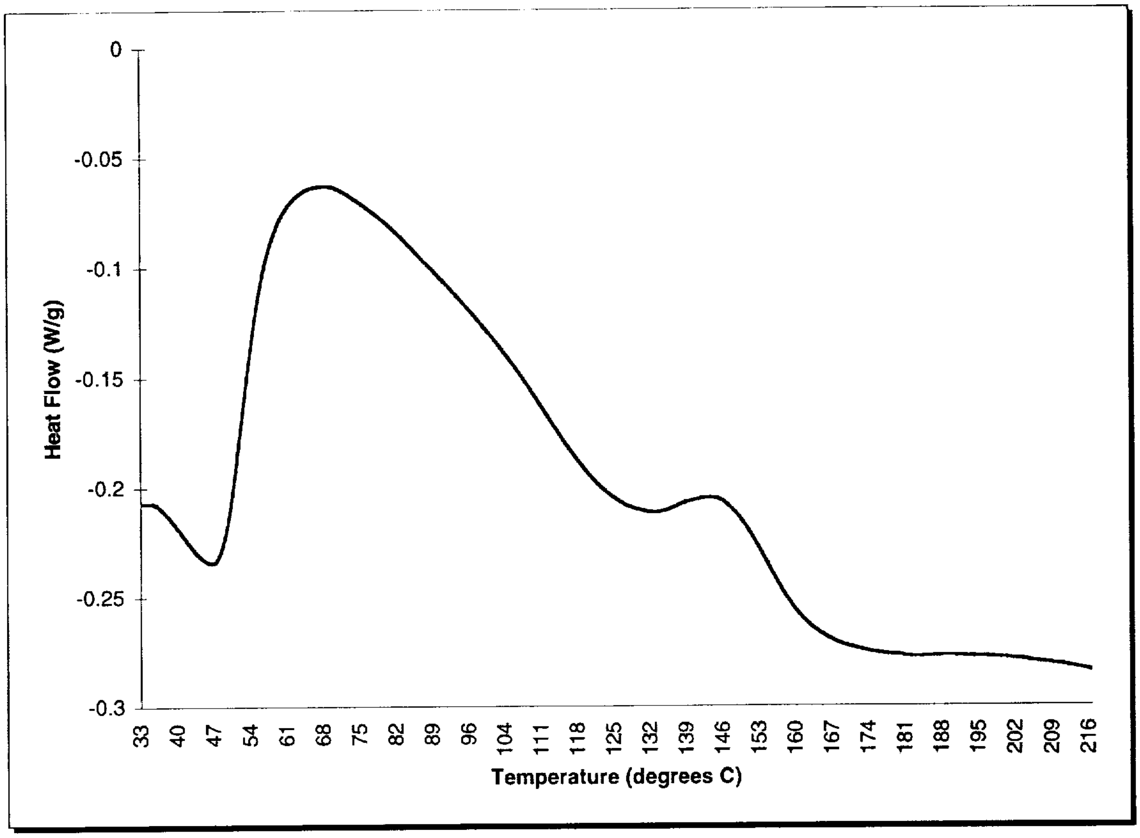

Figure 3.9 Residual Dynamic DSC Scan of 510A-40 at 10°C/min from 25°C to 220°C

The residual heat of reaction was 47 J/g.

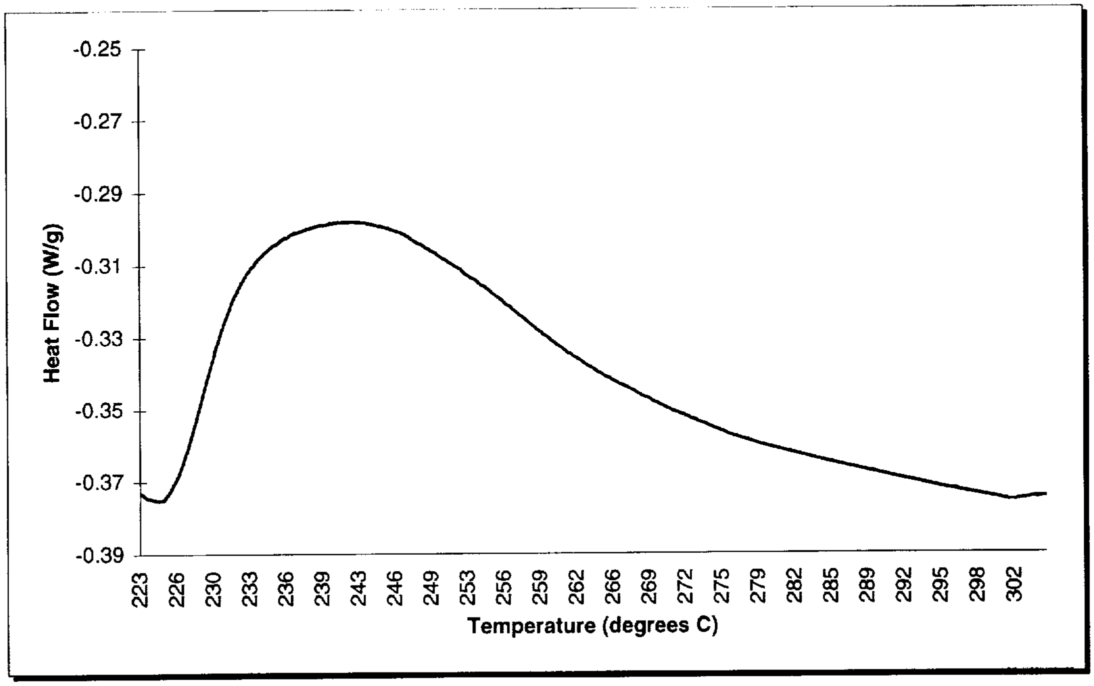

Figure 3.10 Residual Dynamic DSC Scan of L-10 at 10°C/min from 25°C to 350°C

The residual heat of reaction was 16 J/g.

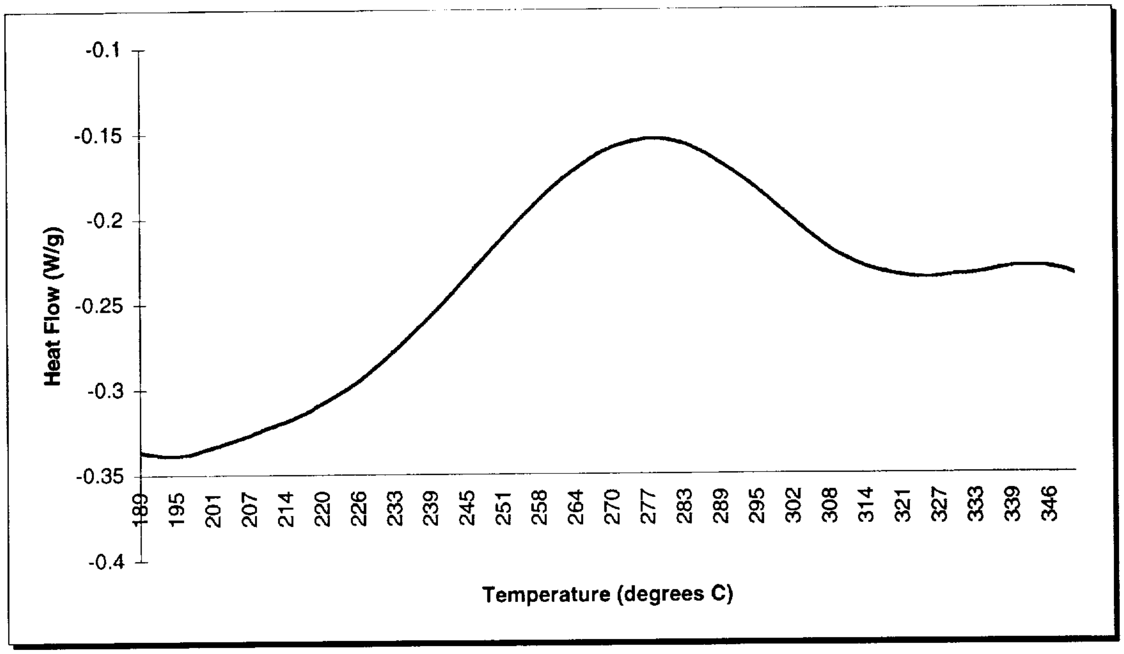

Figure 3.11 Residual Dynamic DSC Scan of SC-36 at 10°C/min from 25°C to 350°C

The residual heat of reaction was 41 J/g.

Table 3.1 Measured Permeability Data for Fiber Preform Systems

Fiber Preform	Permeability (m^2)
8-Stack Multiaxial Warp Knit ($v_f = 0.55$)	
Parallel to the stitching	1.32 E-11
Perpendicular to the stitching	5.89 E-12
Through-the-thickness	1.47 E-12
4-Tube Surface-Lock Braided ($v_f = 0.58$)	
Parallel to the stitching	1.58 E-11
Perpendicular to the stitching	5.60 E-12
Through-the-thickness	6.47 E-13
14-Tube Surface-Lock Braided ($v_f = 0.58$)	
Parallel to the stitching	9.94 E-12
Perpendicular to the stitching	6.43 E-12
Through-the-thickness	1.24 E-12
4-Tube Center-Lock Braided ($v_f = 0.58$)	
Parallel to the stitching	6.36 E-12
Perpendicular to the stitching	2.95 E-12
Through-the-thickness	1.17 E-12
14-Tube Center-Lock Braided ($v_f = 0.58$)	
Parallel to the stitching	1.60 E-11
Perpendicular to the stitching	5.20 E-12
Through-the-thickness	8.92 E-13
1523 E-glass ($v_f = 0.49$)	
Warp	4.80 E-11
Fill	8.40 E-11
Through-the-thickness	8.58 E-13

Table 3.2 Viscosity Measurements of Selected Resin Systems

Resin System (Temperature)	Viscosity (Pa·s)
510A-40 (25°C)	0.45
L-10 (25°C)	0.15
SC-36 (25°C)	3.80
SC-36 (43°C)	0.25

Chapter 4 VARTM Model Development

4.1 Finite Element Computer Code

A finite element code exists at Virginia Tech, which is named 3DINFIL (42). It is a comprehensive, three-dimensional, computer simulation model of the Resin Film Infusion (RFI) and Resin Transfer Molding (RTM) processing techniques. It utilizes the FE/CV method with eight-noded brick elements. The FE/CV method has the geometric flexibility of the finite element method and the exact global mass conservation of the finite volume method. It is a moving boundary method that does not need to be remeshed at each time step. It is, unfortunately, not accurate at the interface because it averages the flow rates entering and exiting each control volume. This inaccuracy often requires mesh refinements near the interface (42).

3DINFIL can be used to predict the flow front location of the resin, the thermal profiles in the preform and tooling, and the degree of cure and viscosity of the resin. This code consists of three separate models: the flow of the resin through the preform, the heat transfer within the preform and tooling, and the cure kinetics and viscosity of the resin. PATRAN software is used as a pre-processor to create the preform and tool geometries and the finite element mesh, and to apply the material properties and boundary conditions.

In the flow model, the three-dimensional, principal permeability tensor for each material is required, along with a parameter input file. This file includes such important parameters as the initial viscosity of the resin and the pressure and temperature processing cycles. Once the code has been compiled and run, PATRAN is used for post-processing and visualization of the results.

The three-dimensional flow model is used to calculate the pressure and velocity fields of the resin in the preform. This information is then used to track the progression of the flow front during processing. Assumptions used in the flow model are:

1. The preform is a heterogeneous and anisotropic porous material. (Anisotropic is defined as the variation of a property within a medium being dependent on direction.)
2. The flow is quasi-static.
3. Inertial effects are neglected, i.e. low Reynold's number.
4. The fluid is Newtonian and incompressible.
5. The fluid does not leak from the mold set-up.

The continuity equation is written as:

$$\frac{\partial v_i}{\partial x_i} = 0 \tag{4.1}$$

where, v_i is the i^{th} component of the interstitial velocity vector. As mentioned earlier, there exists a relationship between this interstitial velocity and the superficial velocity. This relationship can be written as:

$$v_i = \frac{q_i}{\phi} \tag{4.2}$$

where, q_i is the i^{th} component of the superficial velocity vector, and ϕ is the porosity of the preform. For flow through a porous medium, the conservation of momentum equation can be replaced by Darcy's Law (8):

$$q_i = -\frac{S_{ij}}{\eta}\frac{\partial P}{\partial x_j} \tag{4.3}$$

Substitution of eqs. (4.2) and (4.3) into the continuity equation, eq. (4.1), yields a second order, partial governing differential equation for constant ϕ:

$$\frac{\partial}{\partial x_i}\left(\frac{S_{ij}}{\eta}\frac{\partial P}{\partial x_j}\right) = 0 \tag{4.4}$$

The boundary conditions necessary to solve eq. (4.4) are:

1. A flow front pressure condition: $P_{flowfront} = 0$
2. A constant pressure condition at the inlet: $P_{inlet} = P$
3. The velocity normal to the wall at the boundary is zero: $\vec{v} \cdot \vec{n} = 0$ where, $\vec{n}$ is the vector normal to the boundary wall.

Eight-noded brick elements are used in 3DINFIL. Each node is surrounded by a control volume which is either empty, partially full, or completely full. Fill factors are used to represent this fill condition. The fill factor is the ratio of the fluid in the control volume to the total volume of the control volume. It varies from 0 to 1, with 1 being completely full.

3DINFIL calculates the pressure fields of the resin in the preform by imposing the boundary conditions to solve the Galerkin approximation of the governing differential equation. Next, the velocities at the centroid of each element are found by the use of Darcy's Law. The volumetric flow rate can then be found from the velocity and area vectors of the control volume. The final step in 3DINFIL is the updating of the fill factors and the creation of the next time step. A detailed account of the 3DINFIL computer code, as well as the FE/CV method, can be found in Reference 42.

4.2 Finite Element Computer Code Modifications

Modifications to 3DINFIL were made to represent the VARTM processing physics more accurately. These modifications included the effects of capillary pressure and gravity. This was necessary due to the low pressures used for infiltration (~1 atm) causing small pressure gradients throughout the preform. These modifications were incorporated by the following two changes:

1. The boundary condition at the flow front was modified to incorporate capillary pressure:

$$P_{flowfront} = \frac{2}{r_h} \gamma_{lv} \cos\theta \qquad (4.5)$$

where, r_h is the hydraulic radius of the fiber bundle, defined as the cross-sectional area normal to flow divided by the perimeter presented to the fluid. If the geometry of a unidirectional fiber bundle is considered, r_h can be defined based on two different flow directions: flow parallel to the fibers and flow perpendicular to the fibers. For this research, the case for flow perpendicular to a unidirectional fiber bundle was chosen. This was due to the fact that the impregnation of the 1523 E-glass preforms, used in the capillary pressure modeling, occurred primarily in the transverse direction. Thus, r_h was determined to be:

$$r_h = r\left(\frac{\phi}{1-\phi}\right) \tag{4.6}$$

where, r is the radius of the 1523 E-glass fiber, and is equal to 9 E-06 m (92).

2. The governing differential equation was modified to incorporate gravity:

$$\frac{\partial}{\partial x_i}\left(\frac{S_{ij}}{\eta}\frac{\partial P}{\partial x_j} - \frac{S_{ij}}{\eta}\rho g_j\right) = 0 \tag{4.7}$$

where, ρg_j is the pressure due to gravity. The finite element method was used to numerically solve eq. 4.7. The finite element formulation was based on the procedure outlined by Reddy (97) and expressed for an element e as:

$$\left[K_{ij}^e\right]\left[P_j^e - \rho g_j^e\right] = \left[F_i^e\right] \tag{4.8}$$

where,

$$K_{ij}^e = \int_{\Omega_e} \frac{S_{ij}}{\eta} N_{\alpha,i} N_{\beta,j} d\Omega \tag{4.9}$$

and

$$F_i^e = \int_{\Gamma_e} QN_\alpha d\Gamma + \int_{\Omega_e} \frac{S_{ij}}{\eta} \rho g_j N_{\alpha,i} d\Omega \qquad (4.10)$$

where, Ω_e is the domain of an element, Γ_e is the surface of an element, P_j^e is the pressure at each node, ρg_j^e is the pressure due to gravity at each node, Q is the specified flux through the face of an element, and N is a linear interpolation function.

Once the necessary gravity coding changes were finished, the model was first verified against an analytical model. This one-dimensional analytical model was derived from Darcy's Law with gravity, as shown below:

$$q = \frac{-S}{\eta}\left[\frac{dP}{dy} - \rho g\right] \qquad (4.11)$$

where, the flow is one-dimensional in positive y, and g is acting in negative y. Assuming a constant pressure gradient, eq. (4.11) can be written as follows:

$$q = \frac{S}{\eta}\left[\frac{-\Delta P}{y} + \rho g\right] \qquad (4.12)$$

Rewriting q in terms of the interstitial velocity and porosity yields:

$$\frac{dy}{dt} = \frac{S}{\eta\phi}\left[\frac{P_i - P_f}{y} + \rho g\right] \tag{4.13}$$

Integrating eq. (4.13) gives:

$$\int_0^y \frac{1}{\frac{P_i - P_f}{y} + \rho g}\, dy = \int_0^t \frac{S}{\eta\phi}\, dt \tag{4.14}$$

Eq. (4.14) was solved for the infiltration time as a function of preform height. Mathcad was used to solve eq. (4.14) for a 0.5 m high, isotropic column (S = 8.4 E-11 m^2 and ϕ = 0.50). The resin viscosity value was 0.45 Pa·s, and the corresponding specific gravity was 1.22. The change in pressure was 99.5 kPa. All of these values were chosen arbitrarily.

The one-dimensional analytical model results were compared against results from a three-dimensional, finite element model using the modified 3DINFIL code. Two cases were examined in this verification. The first case was for flow without gravity, and the second case was for flow against gravity. All of the parameters in the finite element analysis remained the same as the analytical model except for the three-dimensional preform geometry. To make the three-dimensional model act more "one-dimensionally", the three-dimensional preform base was constructed to be 1 cm wide in the x- and z-direction. Also, a 1 mm high resin film was placed at the base of the preform. This film was constructed to be the exact width of the preform base. It was hoped that these geometry considerations would enable a plug flow in the y-direction and allow these models to be comparable with each other for this verification. Figures 4.1 and 4.2 illustrate this "one-dimensional" geometry used by the modified code.

As was envisioned, the verification was exact for the case without gravity. Both the analytical and 3DINFIL model predicted the same infiltration time of 3,365 seconds. Figure 4.3 shows the 3DINFIL modeled results. It can also be seen from these results that a "one-dimensional" plug flow did occur.

For the case with flow against gravity, the results were nearly identical. The analytical model predicted an infiltration time of 3,506 seconds, while the modified 3DINFIL code predicted an infiltration time extremely close to this value, 3,509 seconds. The 3DINFIL modeled results for flow against gravity are shown in Figure 4.4. For all intents and purposes, this verification was proven successful considering the insignificance of this 0.08% error.

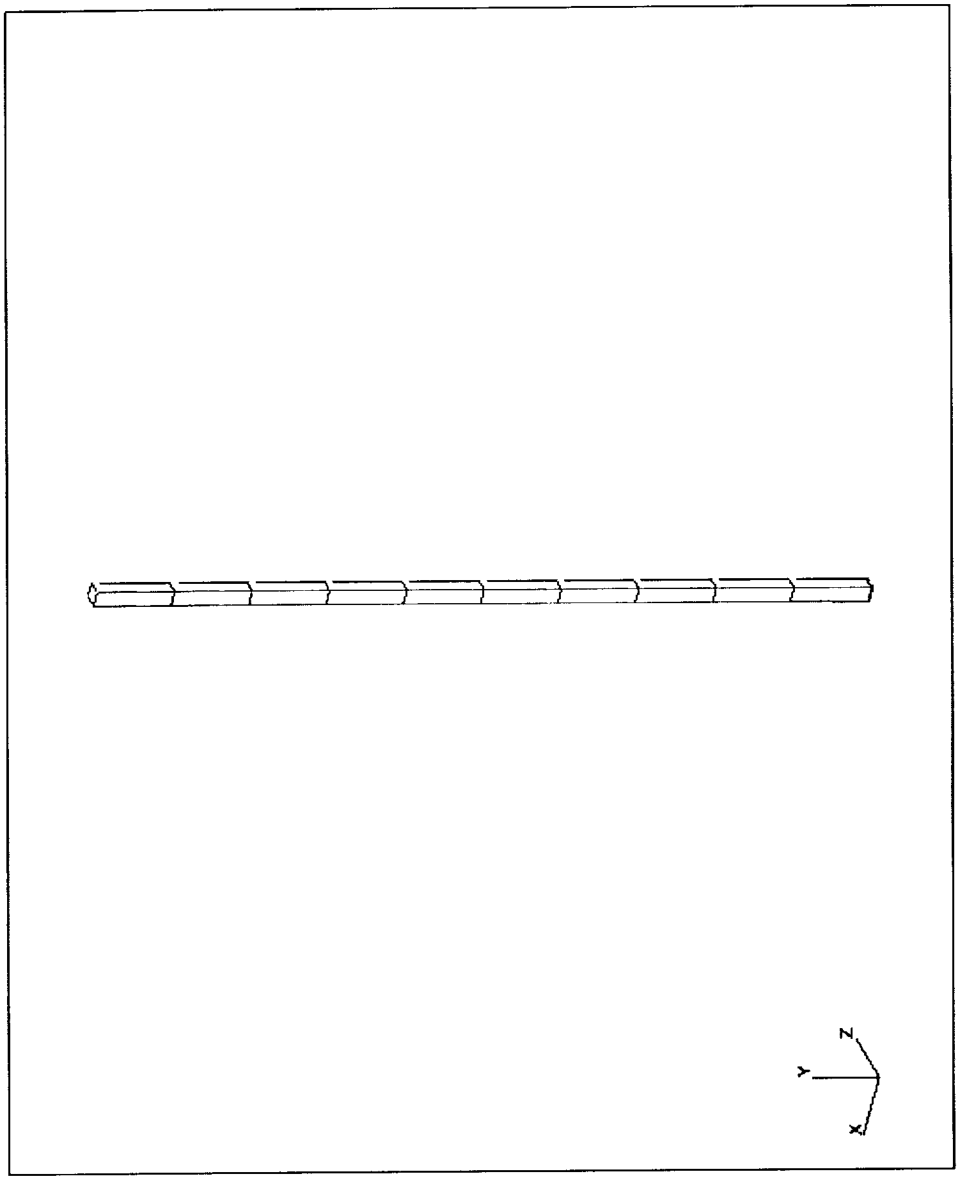

Figure 4.1 Finite element mesh of a “one-dimensional” preform. This mesh consisted of 48 nodes and 11 elements.

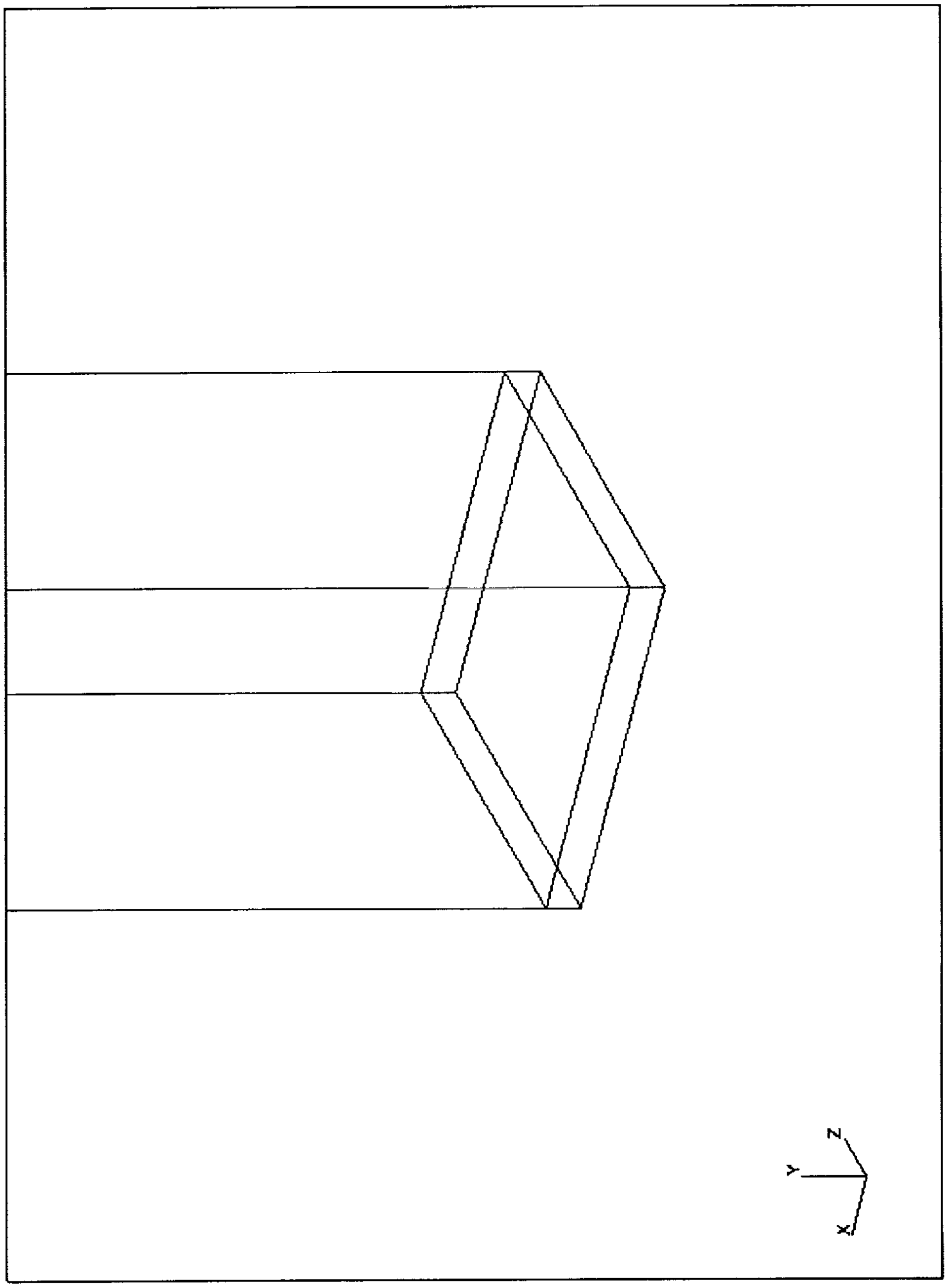

Figure 4.2 Close-up of the "one-dimensional" preform mesh. The 1 mm high resin film is located at the base of the preform.

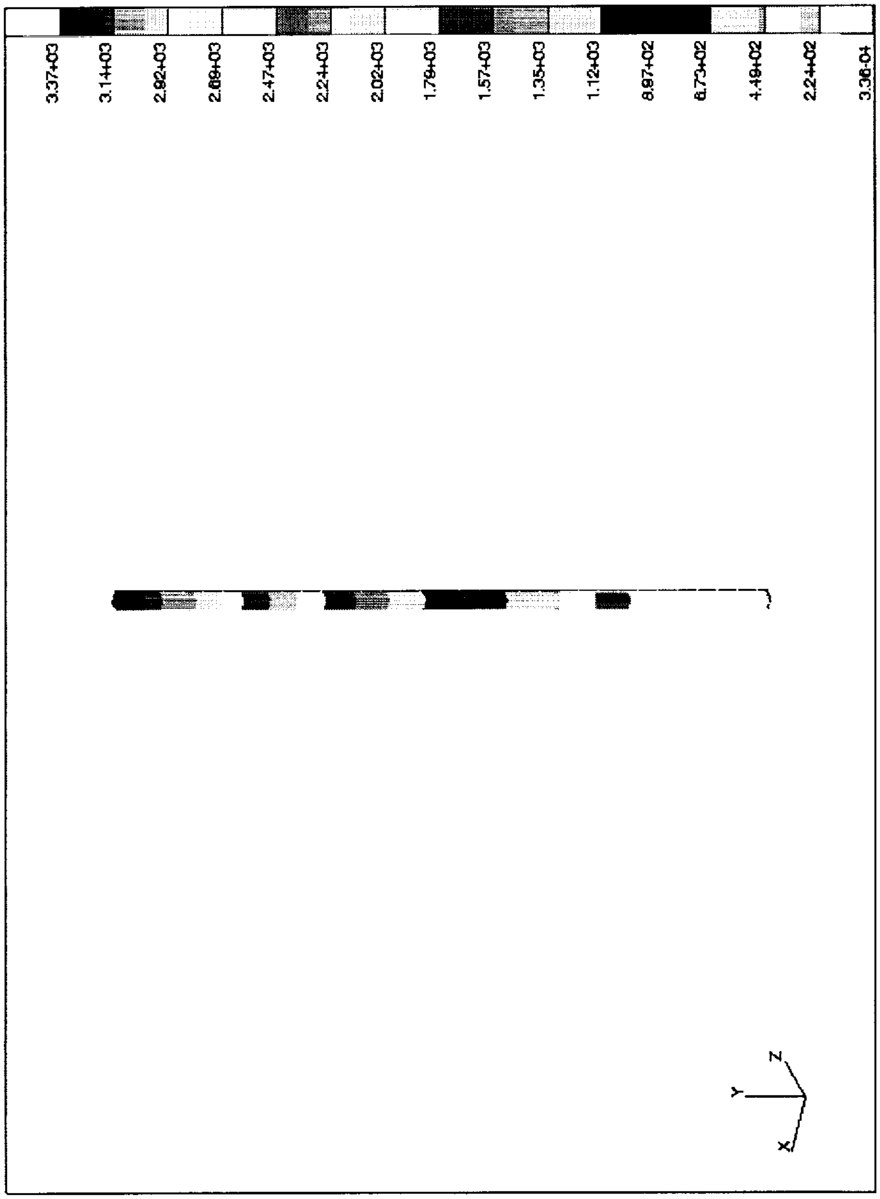

Figure 4.3 Flow front simulation of a 0.5 m high, "one-dimensional" composite panel without gravity. The colored bands represent the flow front location as a function of time, in seconds. The simulated infiltration time was 3,365 seconds.

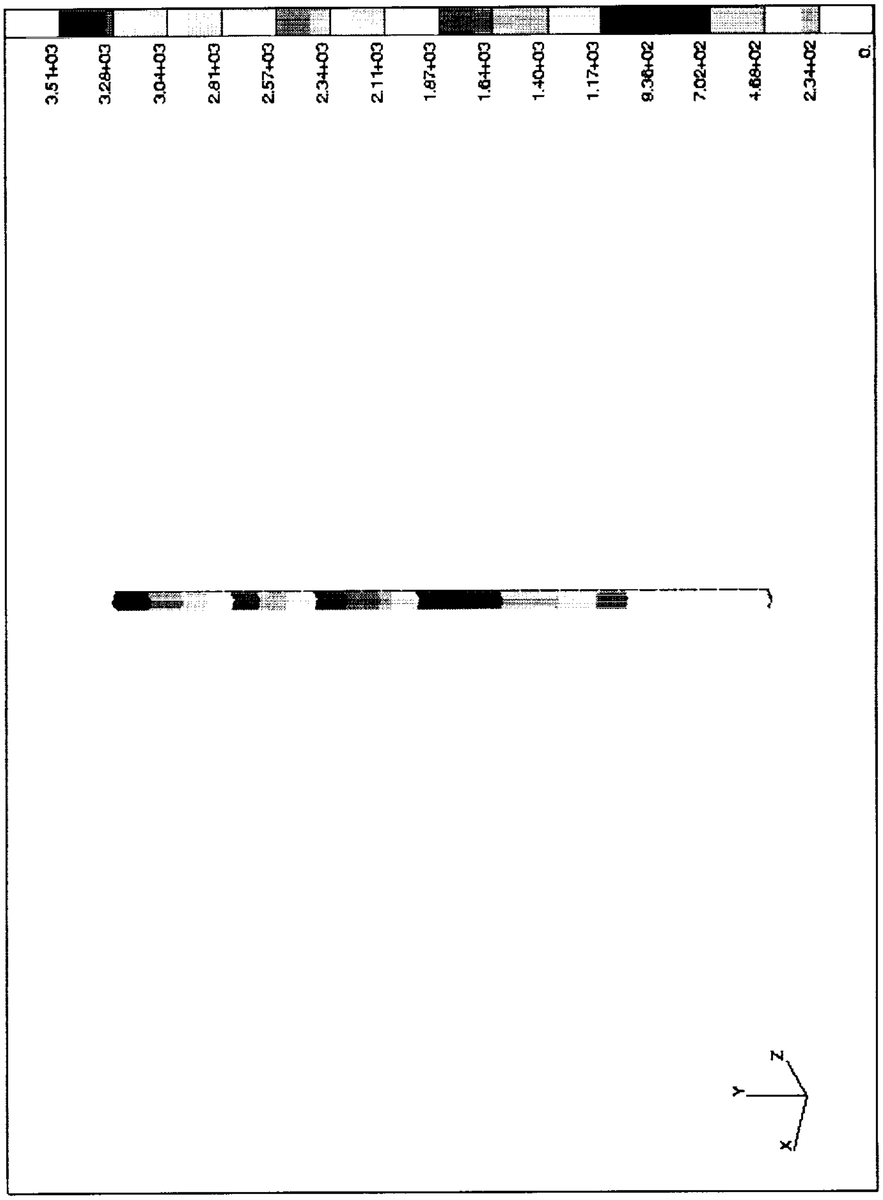

Figure 4.4 Flow front simulation of a 0.5 m high, "one-dimensional" composite panel with gravity acting in -y. The colored bands represent the flow front location as a function of time, in seconds. The simulated infiltration time was 3,509 seconds.

Chapter 5 VARTM Model Verification

5.1 Experimental VARTM Processing

Experimental verification of the computer code was performed to validate the model. For this verification to happen, a VARTM process had to be developed for the lab environment. Figure 5.1 shows the experimental set-up used for manufacturing flat composite panels.

In this set-up, a 66.04 cm long by 17.78 cm wide, dry, fibrous preform is laid onto an open-faced, aluminum tool plate. Then, a porous peel-ply is placed on top of the preform, but underneath a 40.64 cm long by 12.70 cm wide, nylon high-permeable distribution medium. On top of this high-permeable medium is a vinyl resin distribution tube. This tube has four 3.175 mm diameter injection ports on 2.54-cm centers which allow for resin injection. The final step in the lay-up is the placement of a vacuum bag over the entire assembly.

Once the lay-up is complete, the processing can begin. First, a vacuum pump is turned on to expel any air from the preform assembly. After the system has equilibrated, the resin is allowed to flow through the resin distribution tube and across the high-permeable distribution medium. The resin then fills the preform in the transverse direction by "leaking" downward from the high-permeable distribution medium. Figures 5.2 through 5.5 show the progression of flow during the VARTM infiltration of a 10-ply, 1523 E-glass preform with the 510A-40 vinyl ester resin.

The vacuum source is left on until the resin system gels. Once the vacuum is turned off, the part may either cure at room temperature, or it can be placed in an oven to assist the curing process. The actual length of the panels produced using this set-up is only 45.72 cm. The extra 20.32 cm of material acts as both a vacuum breather and a resin bleeder. This excess material is trimmed off of the final product after cure.

Several types of panels were manufactured using this experimental VARTM process. The first series were 10-ply (2.97 mm thick) and 20-ply (5.94 mm thick), 1523 E-glass/510A-40 composite panels. Infiltration times were 330 and 585 seconds, respectively. These panels were subjected to a 24 hour, room temperature (25°C) cure after gel.

In the next series, 4-tube center-lock braided and surface-lock braided carbon panels (5.38 mm thick) and 14-tube center-lock braided carbon panels (17.07 mm thick) were manufactured. All three resins systems were used to manufacture these panels. A 4-tube center-lock braided panel with 510A-40 was infiltrated in 825 seconds, while a 14-tube center-lock braided panel with 510A-40 was infiltrated in 1,620 seconds. Also, a 4-tube surface-lock braided panel was infiltrated with the L-10 resin system in 210 seconds, and the same preform-type was infiltrated in approximately 360 seconds using the SC-36 resin system. The L-10 resin system was injected at room temperature, but required a two hour hold at 200°C to facilitate cure. The SC-36 resin system utilized a cure cycle that consisted of a 43°C injection, followed by a two hour hold at 82°C, then a two hour postcure at 177°C. It should be noted that infiltration times for all of the flat composite panels were obtained with a hand-held stopwatch.

In the final series of tests, more complex preform architectures, typical of aircraft structural composites, were fabricated by the VARTM process. The three-stiffener carbon fiber preform, shown in Figure 5.6, was infiltrated with SC-36 by the VARTM process. This preform consisted of a 60.96 cm long by 60.96 cm wide by 1.43 cm thick, multiaxial warp knit skin and three 9.05 cm high, 14-tube surface-lock braided stiffeners. These stiffeners were flared out at the bottom in order to create a flange that was equal to half the thickness of the 14-tube material. Each flange was then stitched to the skin, forming a preform.

Infiltration of this preform was accomplished by using the reusable vacuum bag designed and fabricated by Seemann Composites, shown in Figure 5.7. This bag is unique in that it contains both the high-permeable distribution medium, shown in Figure 3.6, and the required resin inlet and vacuum ports. The high-permeable medium was formed into the bottom of the vacuum bag, where intimate contact with the top surfaces of the exposed preform skin and stiffeners could be made.

Using this bag, injection occurs through the resin ports on the skin of the preform, and vacuum is pulled through the ports on the top of the stiffeners and at the outer perimeter seals. Resin inlet and vacuum outlet manifolds are used to handle the multiple ports. The SC-36 resin system requires that this entire assembly be placed inside an oven with primary inlet and outlet lines feeding through the wall from the outside lab environment. Figure 5.8 illustrates this set-up. Processing for these more complicated composite panels is similar to the simpler flat panels, except the finished product is the net size of the dry preform, resulting in no excess material. The reusable vacuum bag does not allow for visualization of the flow front, and sensors cannot be placed beneath the bag to provide infiltration times. Therefore, an infiltration time for the three-stiffener cannot be easily recorded.

The three-stiffener preform was infiltrated at 43°C with the SC-36 resin system. However, before the resin was able to completely gel, an exothermic reaction in the resin trap caused the vacuum outlet lines to rupture. Without full vacuum, the panel was not compressed sufficiently to produce an acceptable composite. Although there was sufficient resin present, the panel was too thick, and the surface finish was visibly “dry”. Even though the quality of the composite panel was not acceptable, complete infiltration of the complex-shaped preform was achieved by the VARTM process.

Optical micrographs and C-scans showed very little void present in the 1523 E-glass/510A-40 composite panels. These results are shown in Figures 5.9 and 5.10. C-scans proved not to be effective in the inspection of the stitched carbon panels due to the reflective nature of the complicated stitching. Optical microscopy, however, did provide some insight into the quality of the manufacturing process for the carbon composites. These are shown in Figures 5.11 and 5.12.

Four-point loading was used in order to measure the flexural properties of the 10-ply, 1523 E-glass/510A-40 composite panel and the 4-tube surface-lock braided panels with the L-10 and SC-36 resins. This loading system utilized two load points equally spaced from their adjacent supports, with a distance of one-third of the support span. The ASTM standard D 790 - 92 was used as the guidelines for testing. The specimens were deflected until rupture occurred in the outer fibers. The results from this testing was used as a measure of quality control only, to ensure the merit of this VARTM processing technique in producing quality composite panels.

A span-to-depth ratio of 40:1 was chosen. This was determined based on ASTM recommendations for high-strength reinforced composites in order to eliminate shear effects. Five specimens in both the longitudinal direction (principal axis of higher flexural strength, which is parallel to the stitching) and the transverse direction (principal axis of lower flexural strength, which is perpendicular to the stitching) were tested for each composite panel. In all cases, the area of rupture occurred in the area between the loading rollers and at the outer surfaces. This indicated that there were no stress concentrations due to the loading supports, and failure was due only to bending.

The flexural strength, S (MPa), was calculated as follows:

$$S = \frac{PL}{bd^2} \tag{5.4}$$

where, P is the load at the moment of break (N), L is the support span (mm), b is the width of beam (mm), and d is the depth of beam (mm).

The tangent modulus of elasticity, E, was calculated as follows:

$$E = \frac{0.21L^3m}{bd^3} \tag{5.5}$$

where, m is the slope of the tangent to the initial straight-line portion of the load-deflection curve (MPa).

For the 10-ply, 1523 E-glass/510A-40 composite panels, the sample size was 178 mm long, 25 mm wide, and 2.97 mm thick. The 4-tube surface-lock braided panels were the same length and width, but they were 5.38 mm thick. The 1523 E-glass/510A-40 composite panels and the 4-tube surface-lock braided panels with SC-36 contained no visual surface flaws. The 4-tube surface-lock braided panels with L10, however, exhibited some surface flaws. For all of the panels tested, these flaws had no bearing on the mechanical properties. Panels which had substantially more surface flaws tested as well as panels which had fewer or no flaws in both testing directions.

For the transverse, 4-tube surface-lock braided samples, the fracture line occurred near the middle and at the outer surface but always adjacent to a Kevlar stitch path. These stitchings provided a discontinuity in the carbon preform, thus, creating a path of least resistance when a force was applied. For the longitudinal case, rupture occurred near the middle of the sample and at the outer surface. The one notable difference was in the breaking strength when compared to the transverse samples. This value was increased, nearly double, due to the Kevlar stitching reinforcement. In all cases, the fracture line showed a break in the Kevlar fibers. Although the Kevlar stitching provided an area of fracture in the transverse case, it undoubtedly showed promise in increasing the strength of the composite when aligned along the longitudinal axis. The flexural results for all composite panels tested are shown in Table 5.1.

5.2 General Flow Model Verification

The VARTM flow model was first verified without the influence of capillary pressure or gravity. This verification examined two important factors. The first factor was the flow front pattern. It was desirable to have an accurate simulation of the flow front patterns during processing to determine the placement of resin/vacuum ports and also to examine possible areas where void formation may occur. The second factor was the infiltration time. This factor was necessary for one obvious reason: Without the verification of the simulated infiltration time, an accurate prediction of the experimental processing time would not be available.

The flow front patterns during the VARTM process were verified by comparing the modeled and observed flow patterns during infiltration of 10- and 20-ply, E-glass/510A-40 panels. The E-glass composites were chosen because of the relative ease in observing the flow front during processing. Figures 5.13 and 5.14 show the finite element meshes for the 10- and 20-ply E-glass preforms, respectively, while Figures 5.15 and 5.16 show the results of the models. When comparing these figures with Figures 5.2 through 5.5, which show the experimental flow front patterns, a few similarities can be noticed.

One similarity is in the progression of the resin within the high-permeable medium. This flow front pattern was shown, both theoretically and experimentally, to be a plug flow in the in-plane direction. Another related similarity was in the "leaking" flow of the resin from the high-permeable medium into the preform. Figures 5.3 and 5.4 show this phenomenon occurring experimentally. The change in intensity of the color of the resin, shown in the photos from left to right, is evidence of the "leaking" flow into the E-glass preform. This intensity increases as more resin volume is accumulated in the preform by the complete infiltration in the transverse direction. This phenomenon is somewhat corroborated by the modeled results of Figure 5.16. This 20-ply panel shows a better "leaking" flow front because of its added thickness. The resin can be seen to flow in the -y-direction with a graduated lead-lag from top to bottom. This lead-lag is responsible for filling the top preform layers first and the bottom layers last.

A final similarity, which is not clearly shown in these particular experimental photos, is in the last points to fill for both glass panels. These points were in the far corners of the preform away from the injection ports. These were the last points to fill because the resin fills the entire high-permeable medium first (Figure 5.4) while leaking through the preform located directly beneath it. Then, the resin proceeds to invade the remaining E-glass preform without the aid of the high-permeable medium in the in-plane direction. Complete infiltration of the corners occurs last because there is a longer distance to travel from the "local resin source", or high-permeable medium. These last fill points are clearly shown to occur at the far corners of the composite panel in the modeled results of Figures 5.15 and 5.16.

Infiltration times give a much more quantitative measure for model verification compared to the flow front pattern observations. The measured infiltration times for several panels were presented in section 5.1. All of the flat panels processed in the lab were simulated by 3DINFIL, and the modeled fill times were found to be within 10% of recorded infiltration times. The simulations and their respective meshes are shown in Figures 5.13 through 5.22.

The model calculated infiltration times for the 10- and 20-ply E-glass preforms were within 8% of measured times, and the 4-tube center-lock braided panel with 510A-40 and the 4-tube surface-lock braided panel with SC-36 were both within 9% of their respective measured times. The predicted fill time for the 4-tube surface-lock braided preform infiltrated with L-10 was 10% higher than the measured fill time. This 8 to 10% over prediction also occurred with the thickest panel modeled, the 14-tube center-lock braided preform. The predicted fill time for this panel was 9% higher than the measured time.

5.3 Capillary Pressure Model Verification

The capillary pressure was modeled using the boundary condition modification that was discussed in Section 4.2 of Chapter 4. The subsequent verification was performed on the 10- and 20-ply, 1523 E-glass/510A-40 composite panels. These panels were chosen because of the simplicity of their unidirectional fiber bundles and plain weave architecture.

The capillary pressure was calculated for the transverse impregnation of the 1523 E-glass fiber bundles by the 510A-40 resin system. Based on the porosity of the 1523 E-glass fabric and the surface tension and contact angle values for the 1523 E-glass/510A-40 system, the capillary pressure was calculated to be 5.6 kPa, and it was assumed to remain constant throughout processing. This calculated capillary pressure was considered to be an additive term to the injection pressure of 94.5 kPa, which was the maximum obtainable vacuum pressure in the lab.

Figure 5.23 shows the influence of capillary pressure on the infiltration of a 10-ply, 1523 E-glass fabric preform with the 510A-40 resin system. It can be seen from this figure that the calculated infiltration time is now within 2% of the measured infiltration time of 330 seconds, instead of the 8% margin shown in Figure 5.14.

Figure 5.24 shows the capillary pressure effect on the infiltration time for the 20-ply E-glass preform. The calculated infiltration time is now within 3% of the measured time of 585 seconds. This is a substantial improvement compared to the 8% over prediction shown in Figure 5.16, when capillary pressure was neglected.

Based on these results, it is postulated that the capillary pressure may play a large role in VARTM processing. Further modeling of the capillary pressure could provide significant insight into this phenomenon. This effort assumed a constant capillary pressure using a static contact angle. In reality, this contact angle may change during processing. For example, the contact angle could increase in value as the viscous drag becomes significant, which would reduce the capillary pressure. Therefore, the capillary pressure generated during processing may be smaller than what was theoretically calculated here. Although this may be true, these results show the capability of the capillary pressure to reduce the simulated infiltration times by as great as 6% for low-pressure injection processes.

5.4 Gravity Model Verification

Since the gravity theory, finite element formulation, and coding were deemed correct by the verification of the modified 3DINFIL code with an analytical model, the next step was to examine the effect of gravity in previous models. This effect was found to be negligible in all cases. Re-examination of all flat panel models showed no change in predicted infiltration times with or without gravity forces present. The only noticeable effect was on the more complicated three-stiffener composite panel, but it was still negligible. The mesh and predicted infiltration time for this composite panel using the unmodified code are shown in Figures 5.25 and 5.26. (Only one-quarter of this panel was modeled because of symmetry.) Figure 5.27 shows the predicted infiltration time using the modified code. For this panel, the gravity slowed infiltration by 0.37%, from 1,547 seconds to 1,553 seconds. In this work, it was assumed that any change in infiltration time by less than 1% was negligible.

Figure 5.1 Experimental VARTM Processing Set-Up for a

10-ply, 1523 E-glass Composite Panel

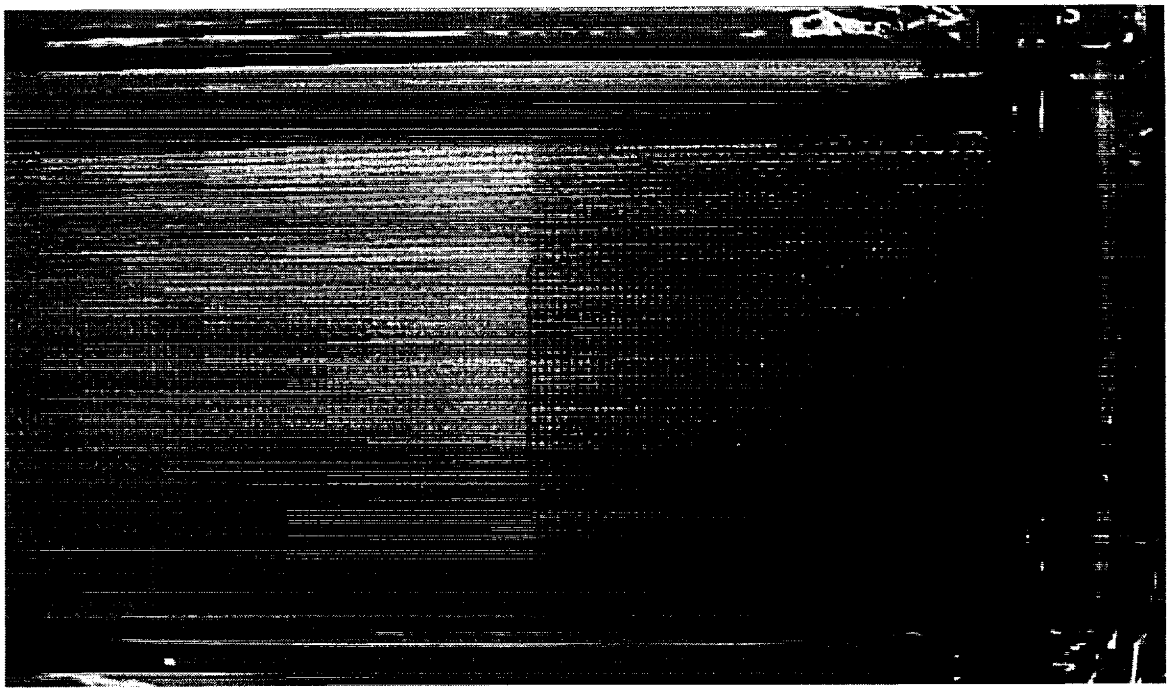

Figure 5.2 Resin enters high-permeable distribution medium.

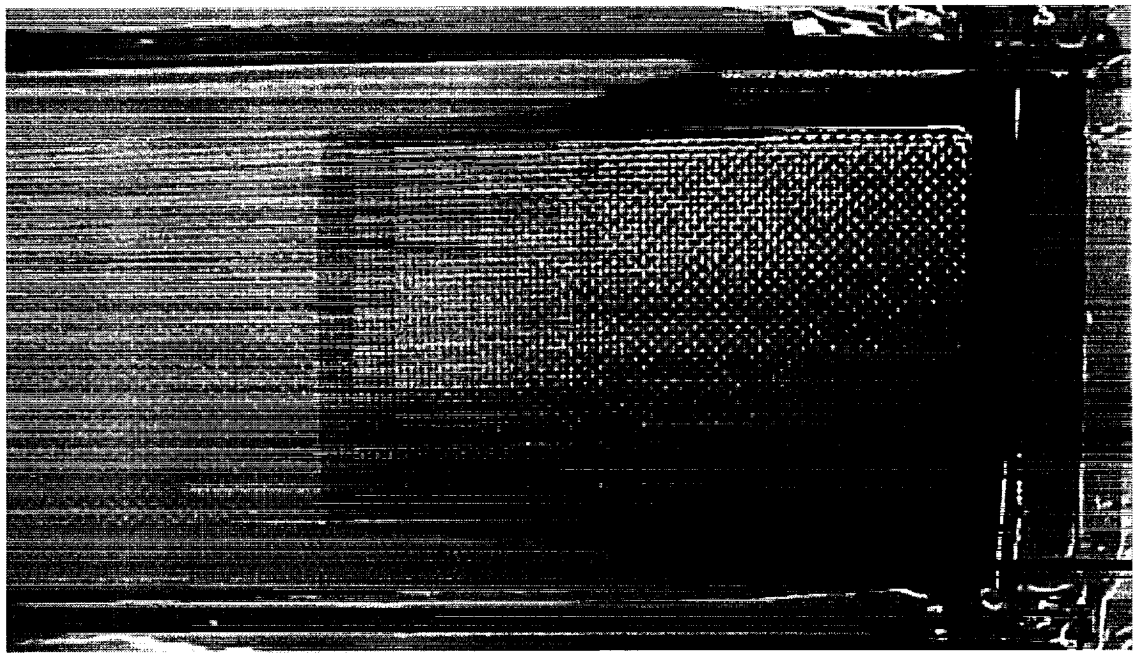

Figure 5.3 Resin begins to "leak" through preform.

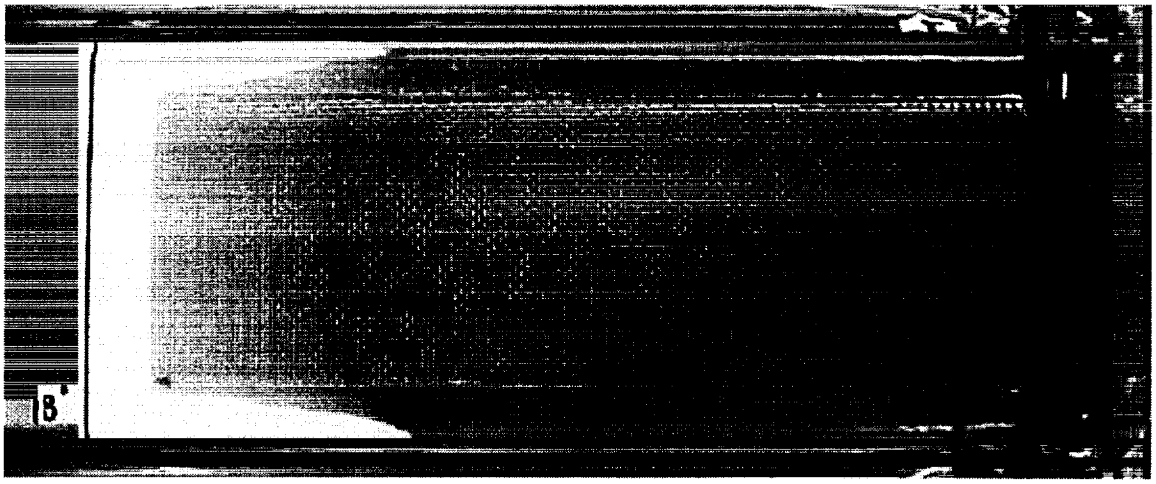

Figure 5.4 Resin completely fills high-permeable distribution medium.

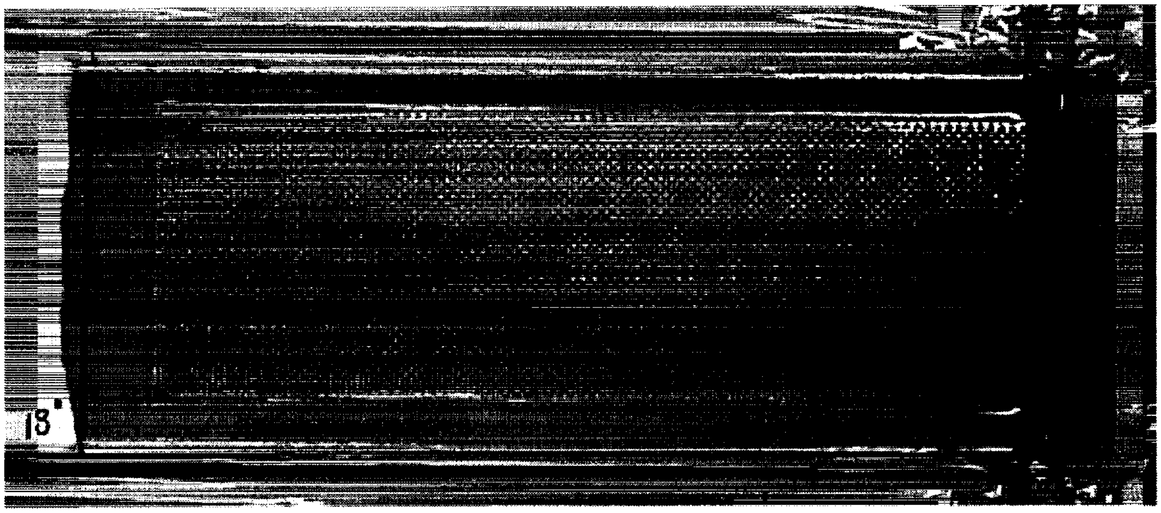

Figure 5.5 Composite panel is successfully infiltrated.

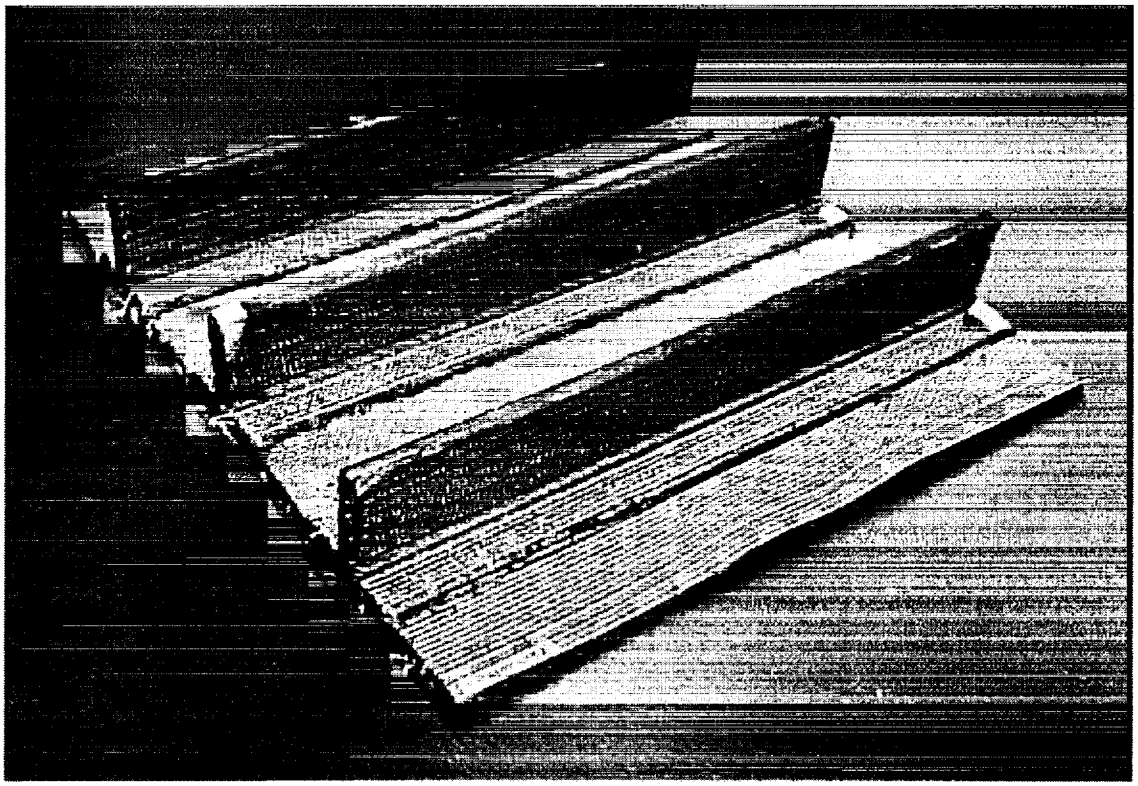

Figure 5.6 Three-Stiffener Carbon Fiber Perform

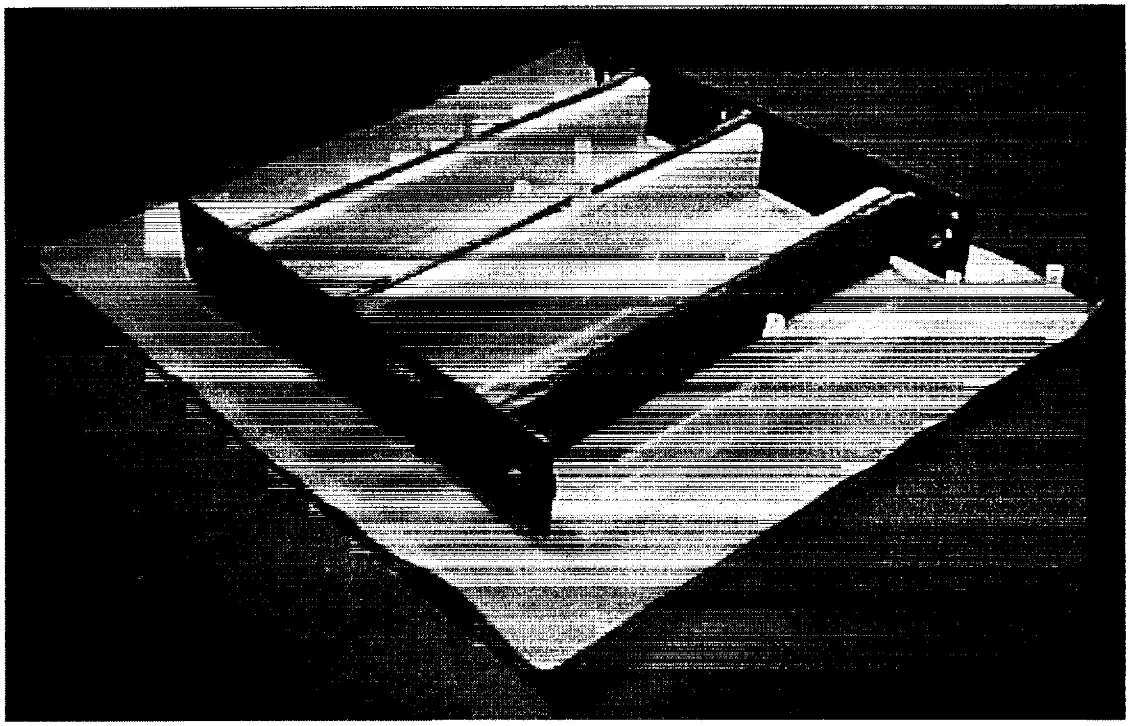

Figure 5.7 Three-Stiffener Vacuum Bag

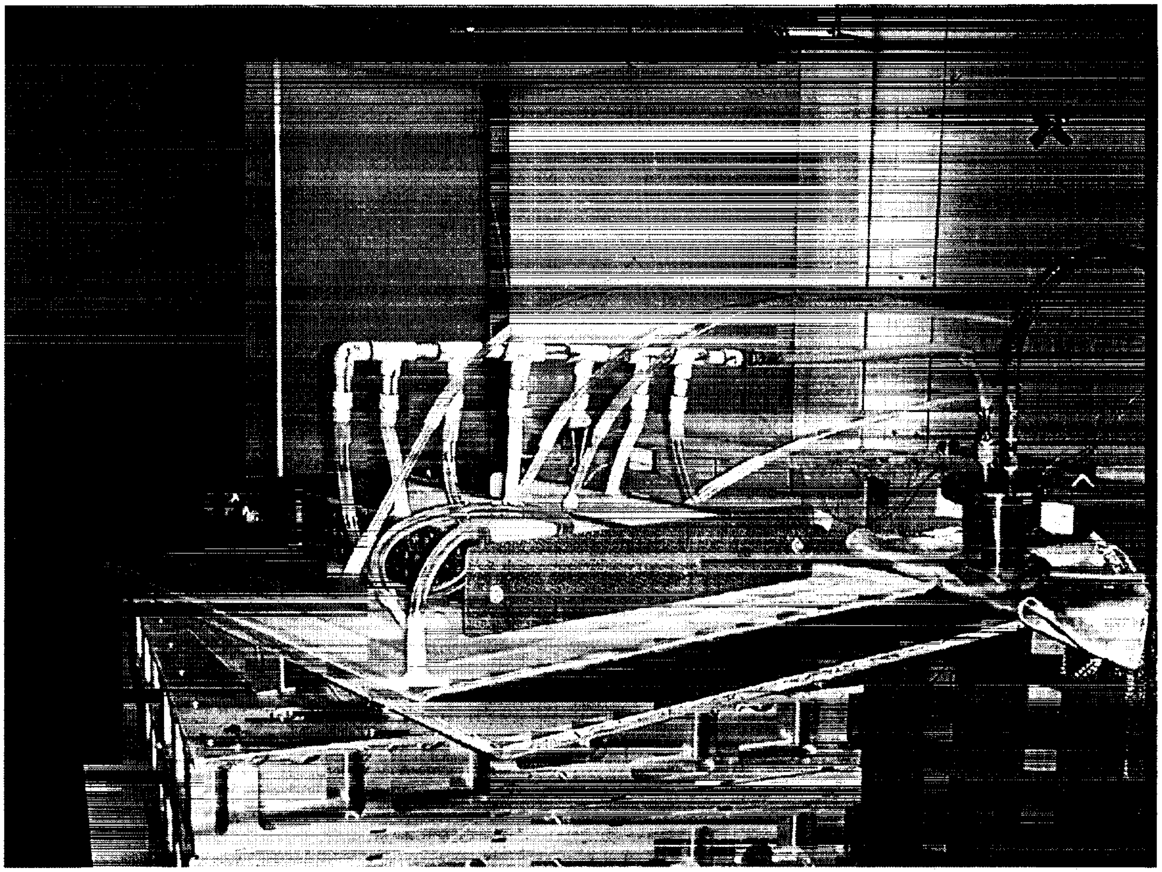

Figure 5.8 Experimental VARTM Processing Set-Up for a Three-Stiffener Carbon Panel

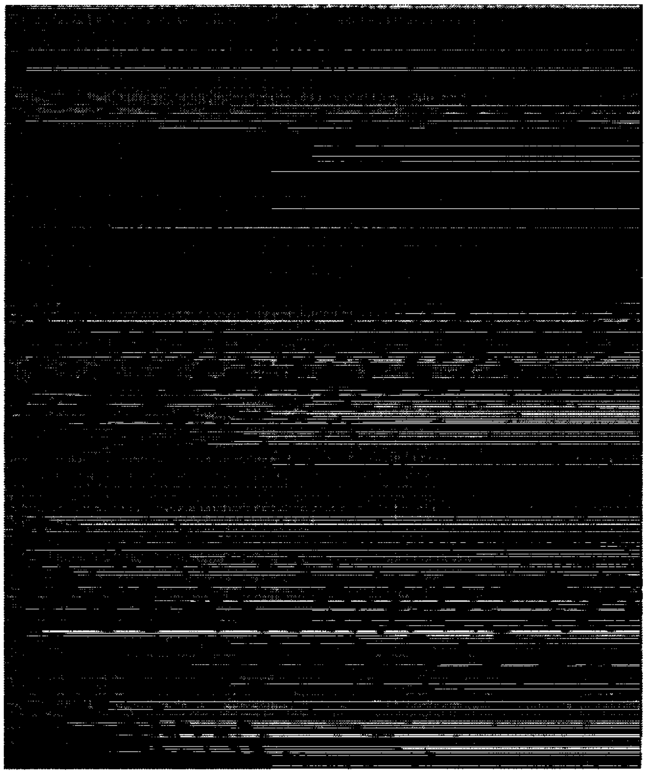

Figure 5.9 Optical Micrograph of 1523 E-glass/510A-40 Composite Panel

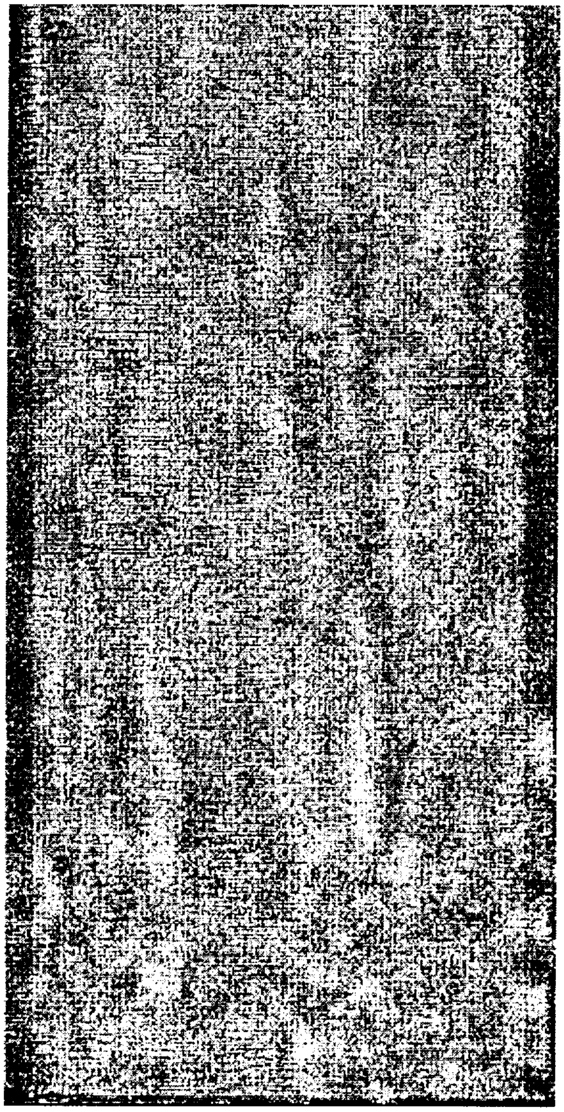

Figure 5.10 C-scan Image of 1523 E-glass/510A-40 Composite Panel

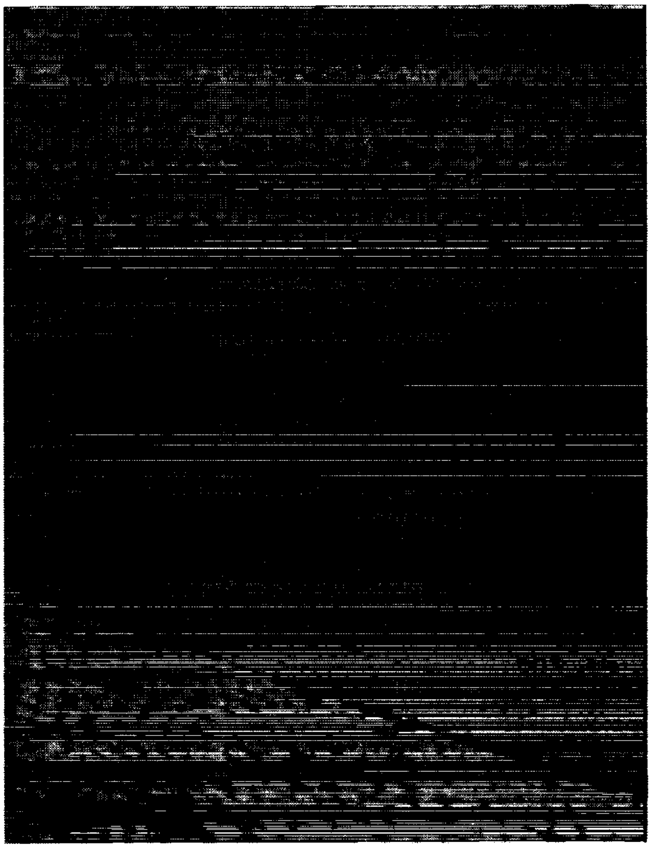

Figure 5.11 Optical Micrograph of 4-Tube Surface-Lock Braided Panel with L-10 Resin

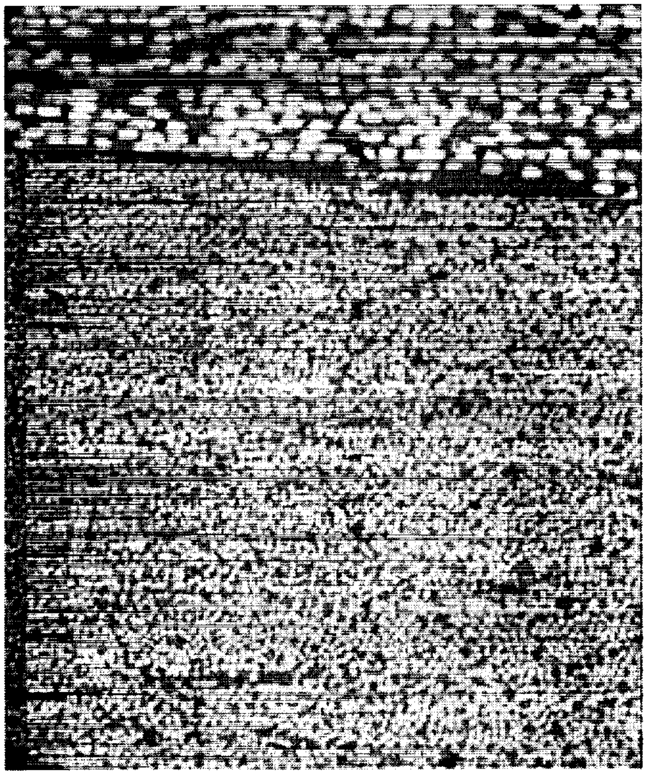

Figure 5.12 Optical Micrograph of 4-Tube Surface-Lock Braided Panel with SC-36 Resin

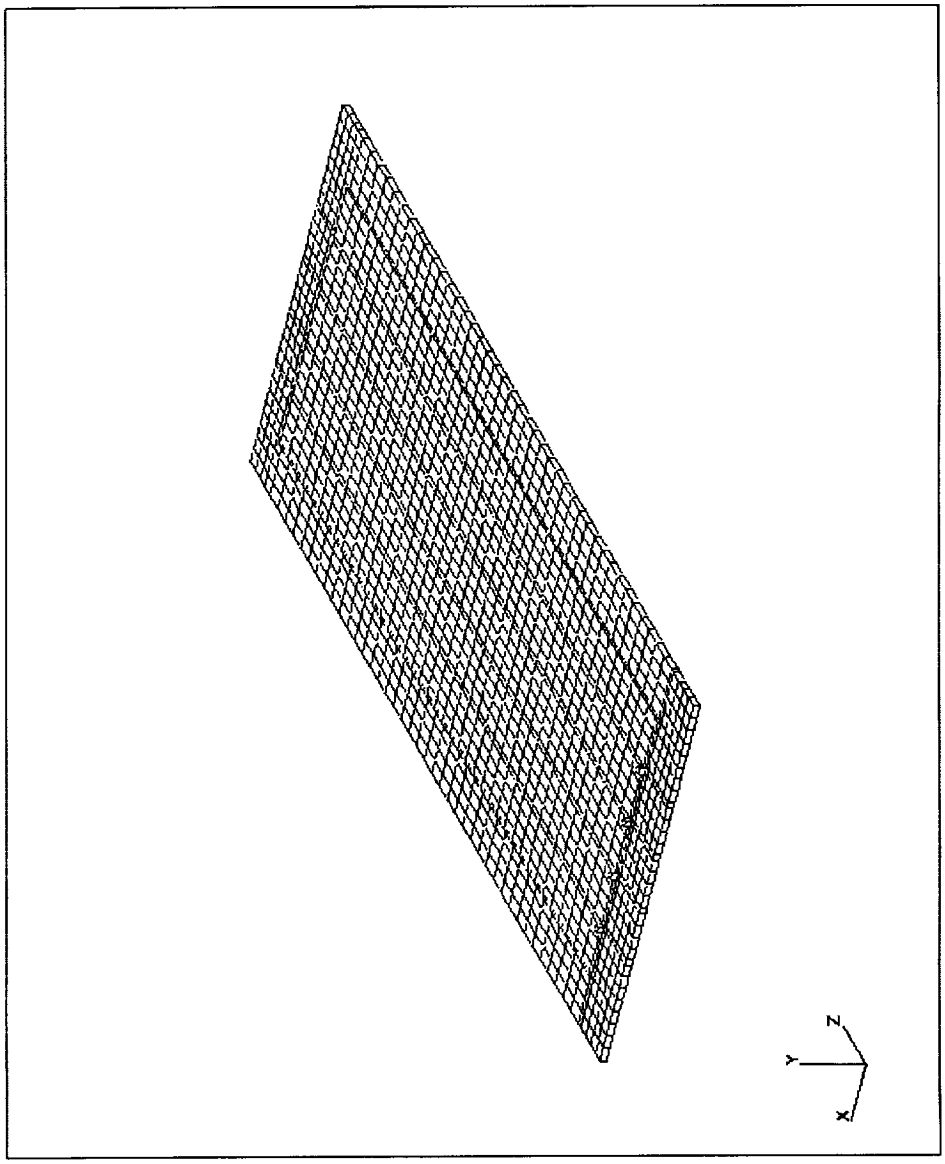

Figure 5.13 Finite element mesh of a 10-ply, 1523 E-glass preform. This mesh consisted of 4,366 nodes and 2,556 elements.

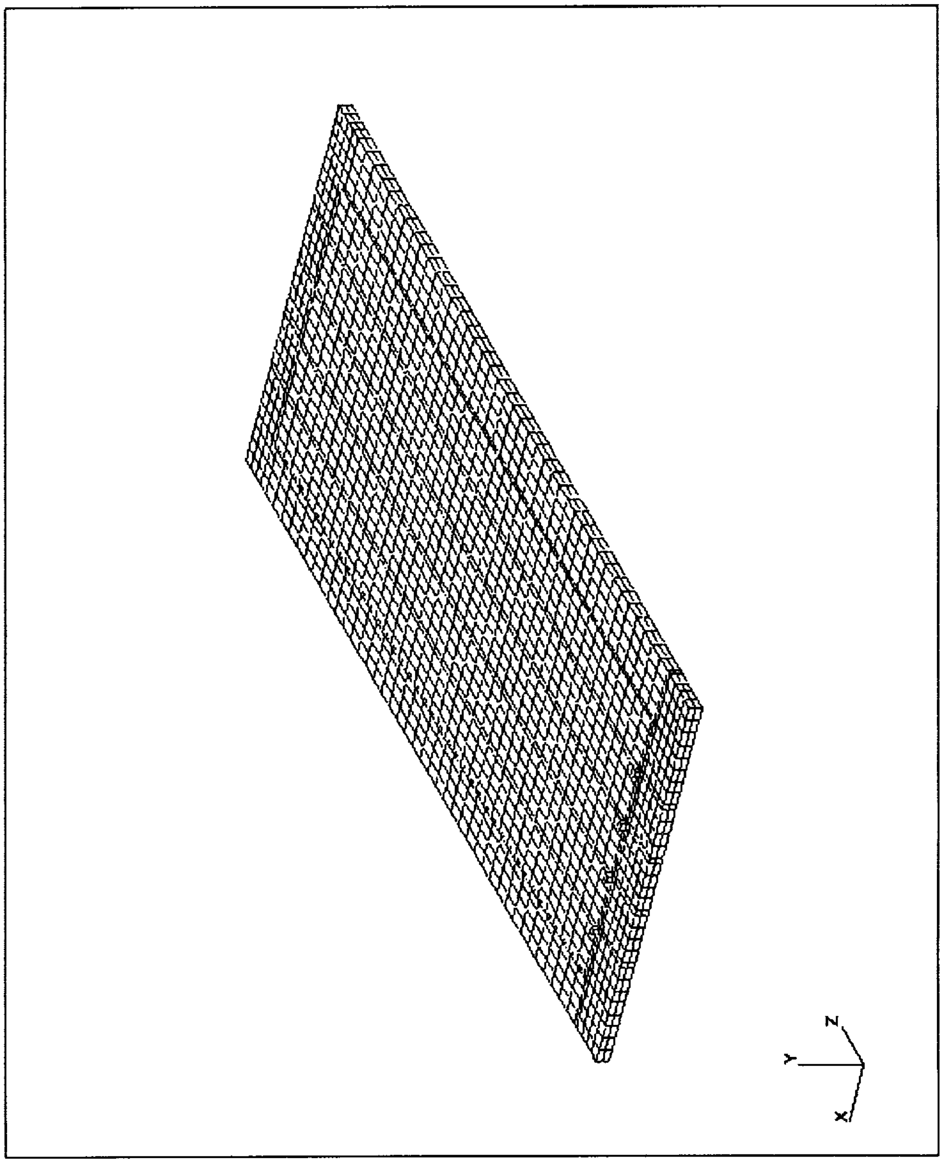

Figure 5.14 Finite element mesh of a 20-ply, 1523 E-glass preform. This mesh consisted of 6,016 nodes and 4,124 elements.

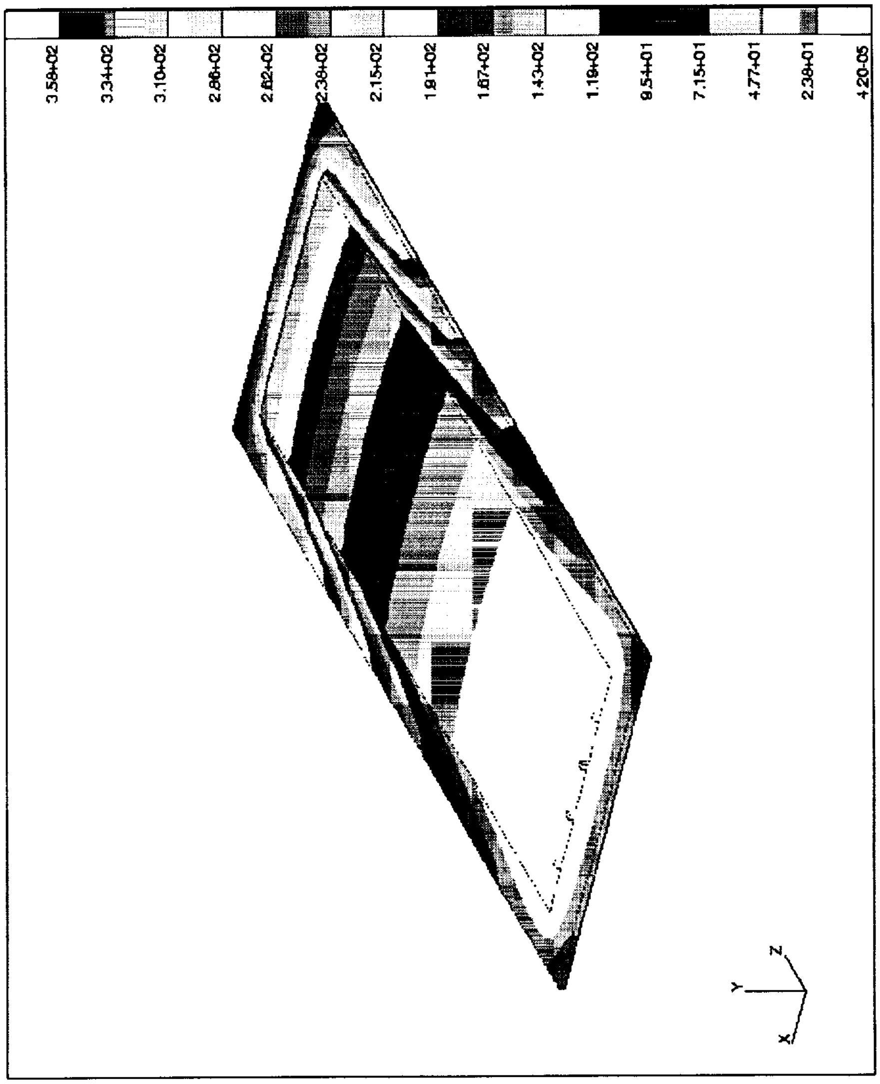

Figure 5.15 Flow front simulation of a 10-ply, 1523 E-glass/510A-40 composite panel. The colored bands represent the flow front location as a function of time, in seconds. The simulated infiltration time was 358 seconds.

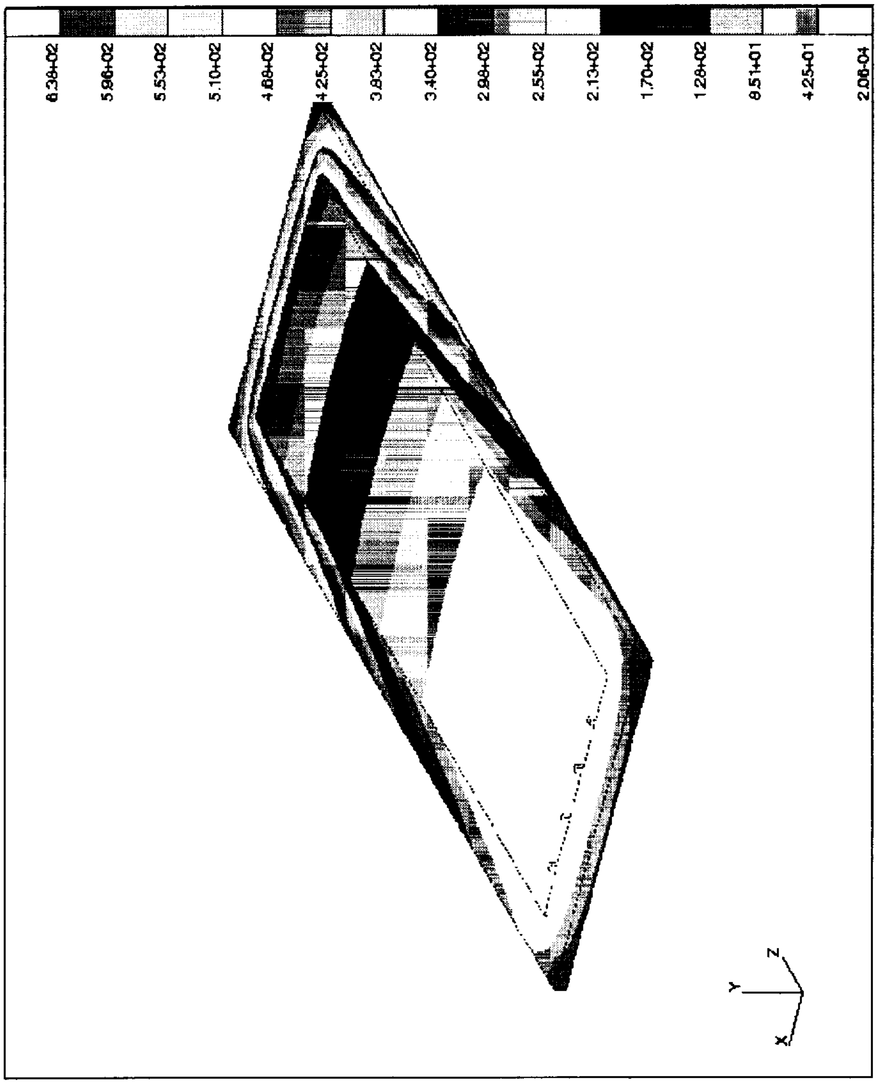

Figure 5.16 Flow front simulation of a 20-ply, 1523 E-glass/510A-40 composite panel. The colored bands represent the flow front location as a function of time, in seconds. The simulated infiltration time was 638 seconds.

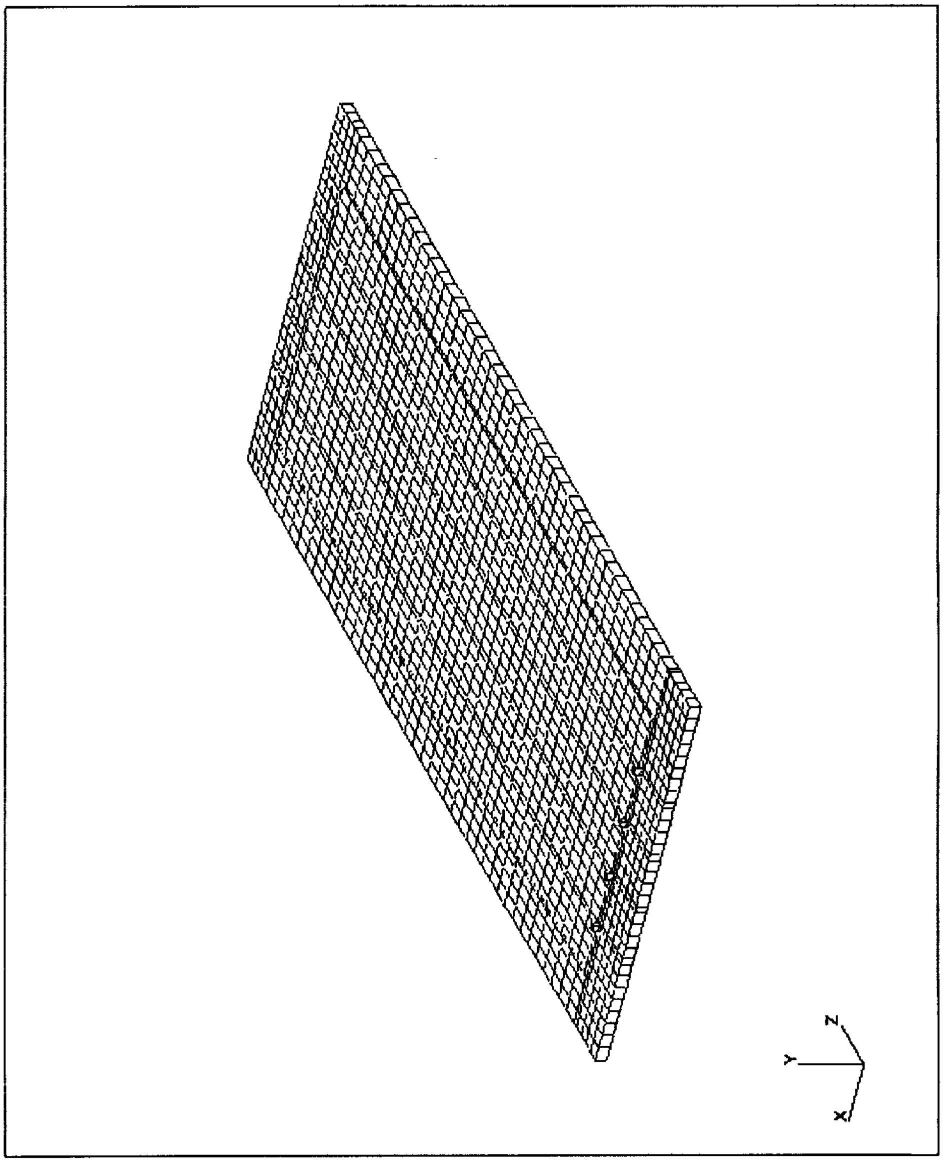

Figure 5.17 Finite element mesh of both a 4-tube center-lock braided and surface-lock braided preform. This mesh consisted of 4,366 nodes and 2,556 elements.

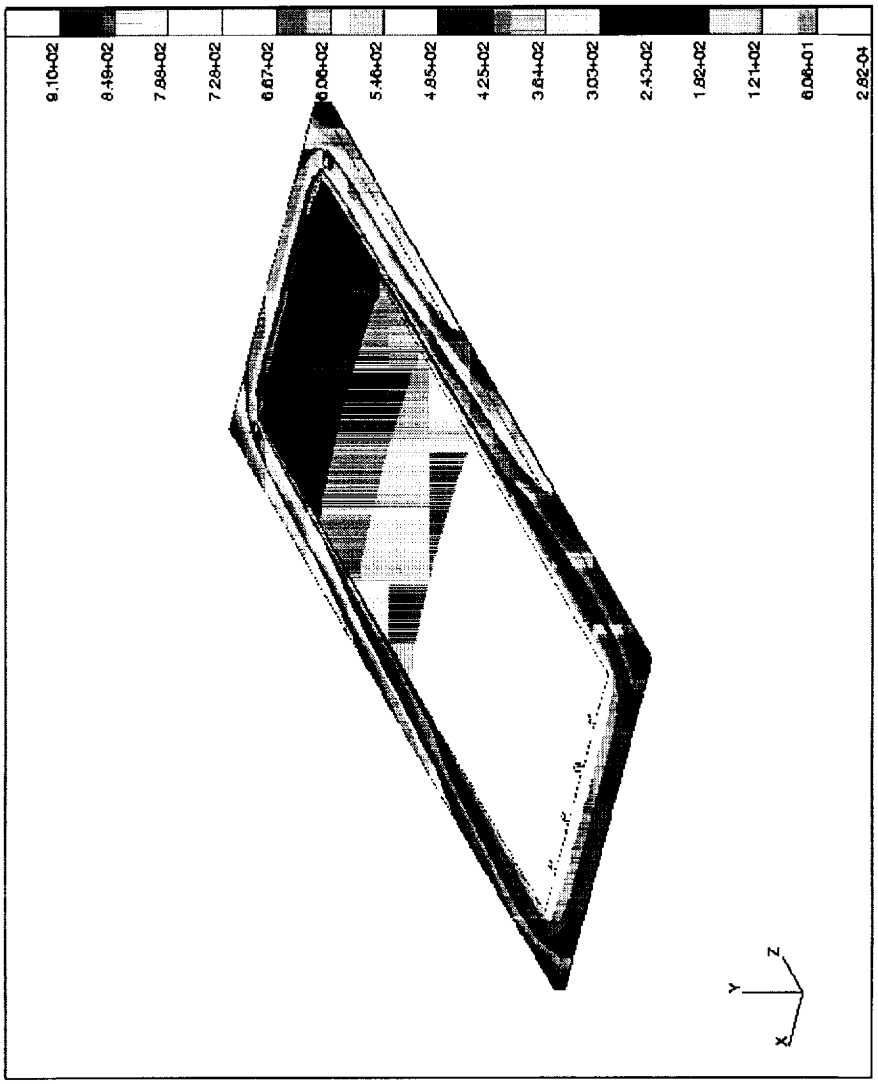

Figure 5.18 Flow front simulation of a 4-tube center-lock braided panel with 510A-40. The colored bands represent the flow front location as a function of time, in seconds. The simulated infiltration time was 910 seconds.

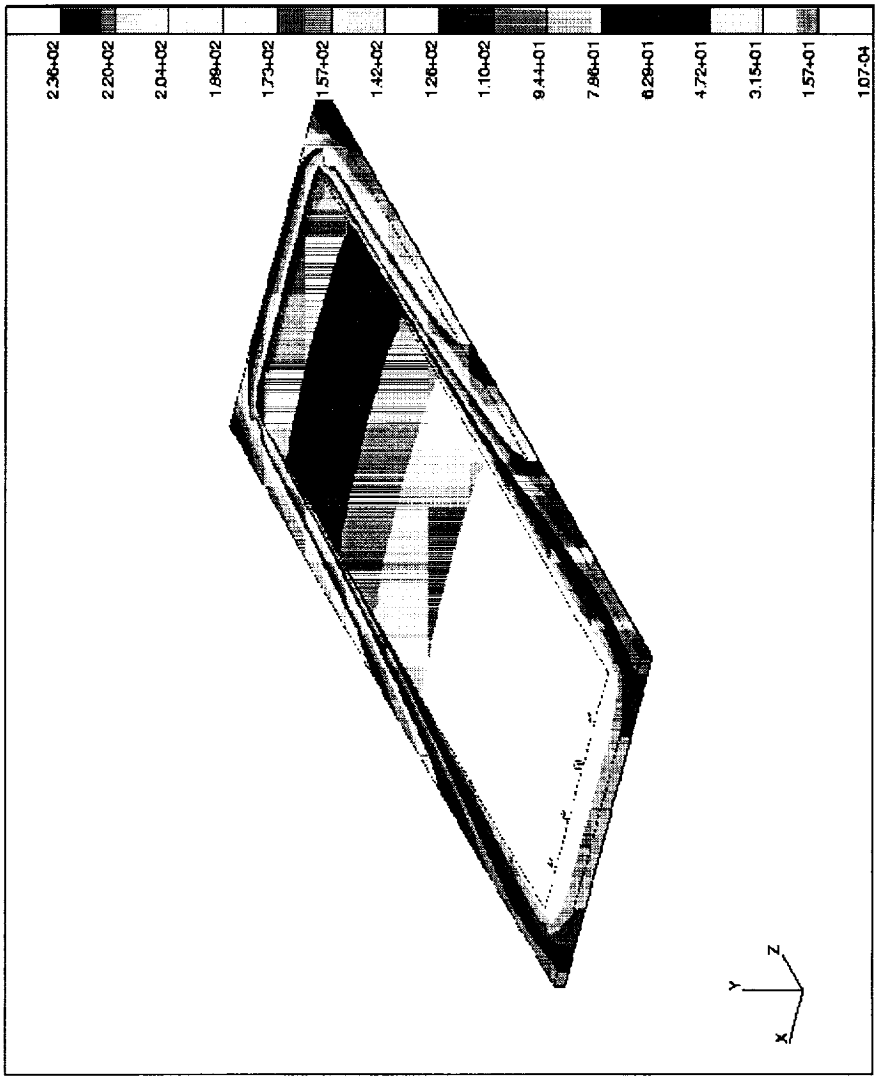

Figure 5.19 Flow front simulation of a 4-tube surface-lock braided panel with L-10. The colored bands represent the flow front location as a function of time, in seconds. The simulated infiltration time was 236 seconds.

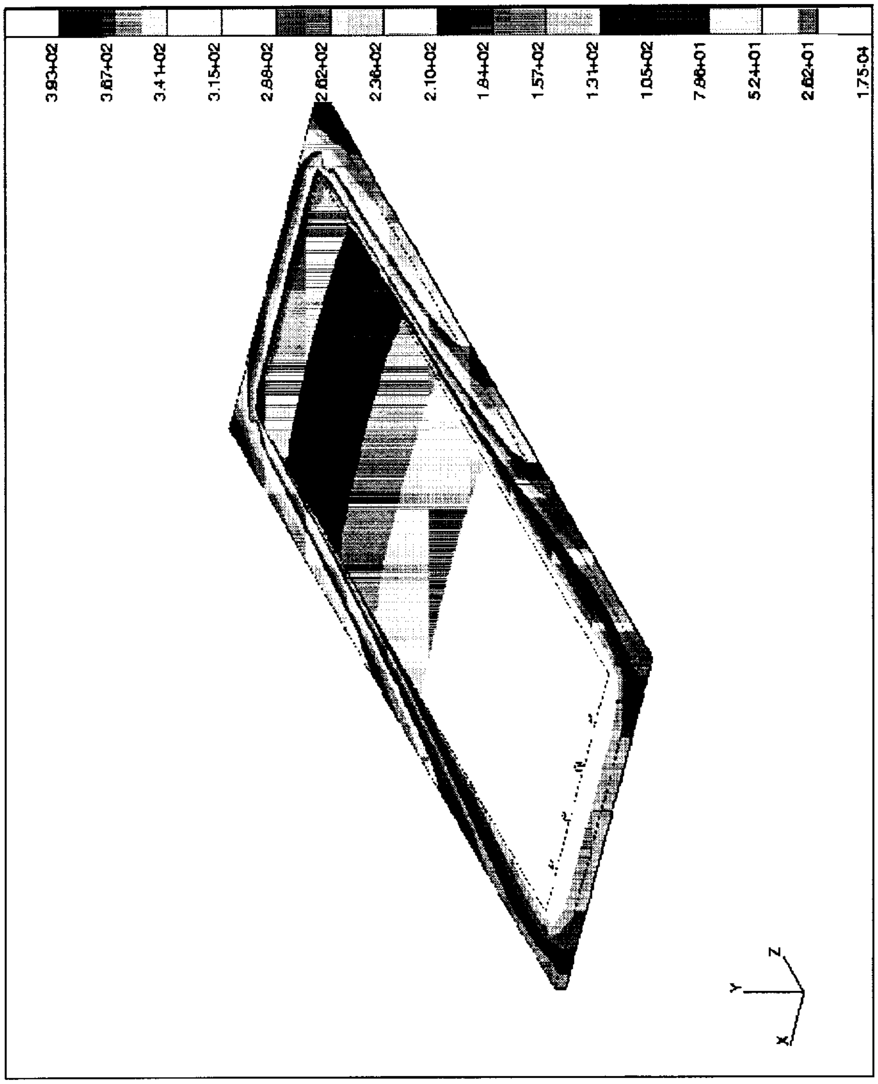

Figure 5.20 Flow front simulation of a 4-tube surface-lock braided panel with SC-36. The colored bands represent the flow front location as a function of time, in seconds. The simulated infiltration time was 393 seconds.

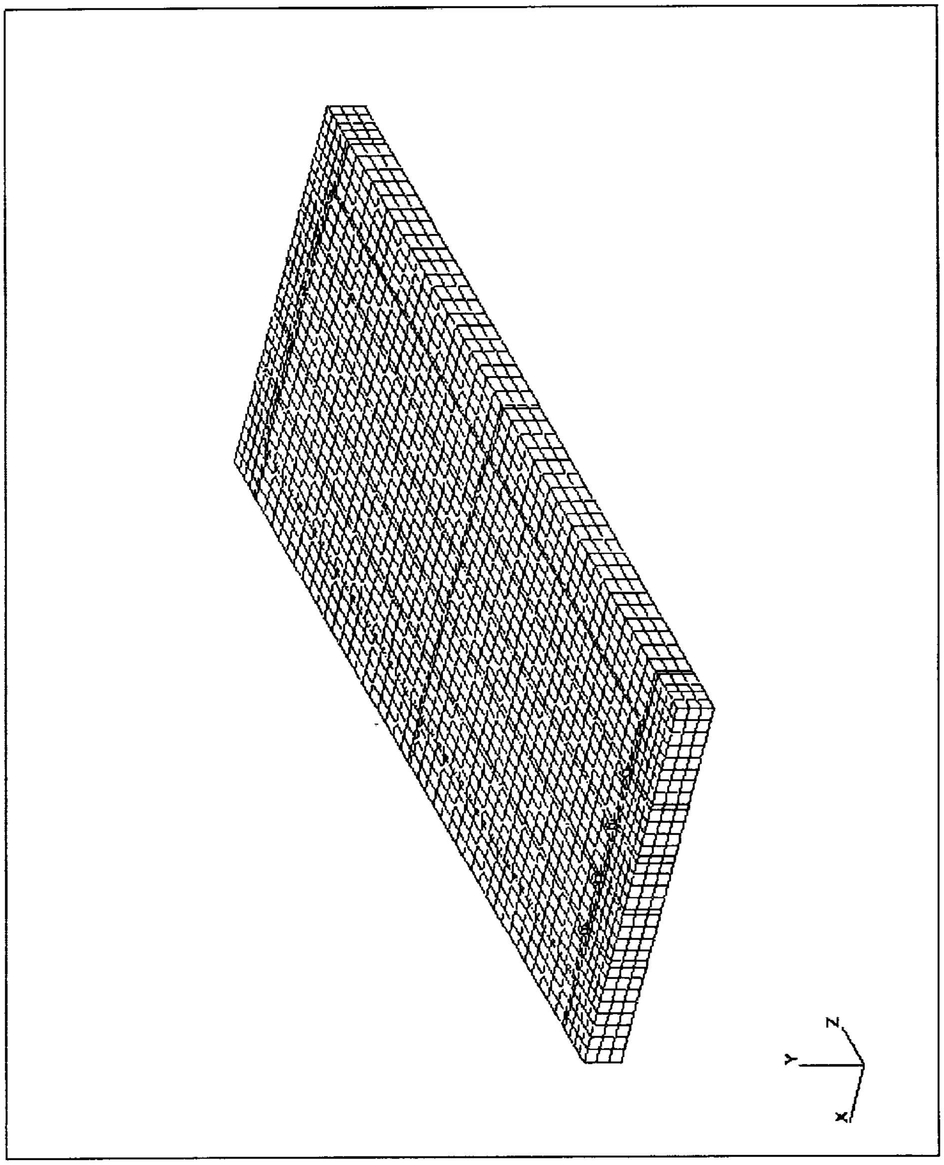

Figure 5.21 Finite element mesh of the 14-tube center-lock braided preform. This mesh consisted of 7,980 nodes and 5,932 elements.

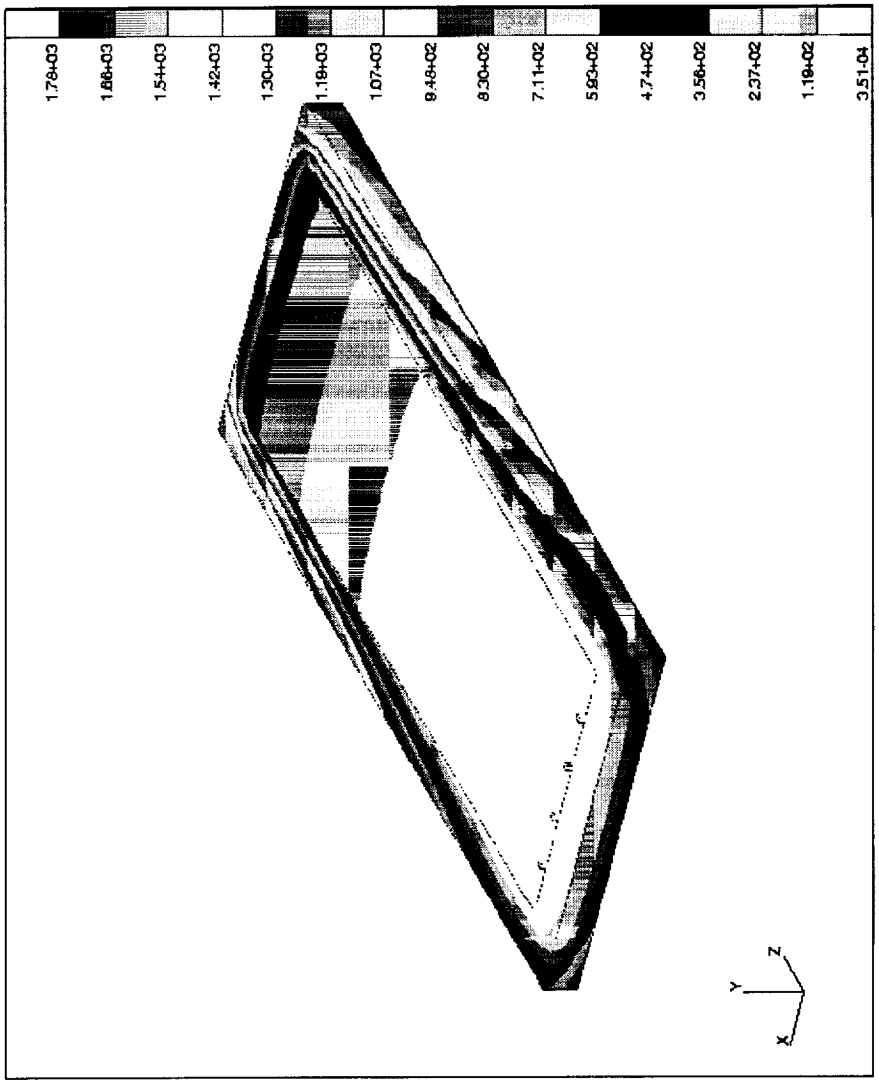

Figure 5.22 Flow front simulation of a 14-tube center-lock braided panel with 510A-40. The colored bands represent the flow front location as a function of time, in seconds. The simulated infiltration time was 1,778 seconds.

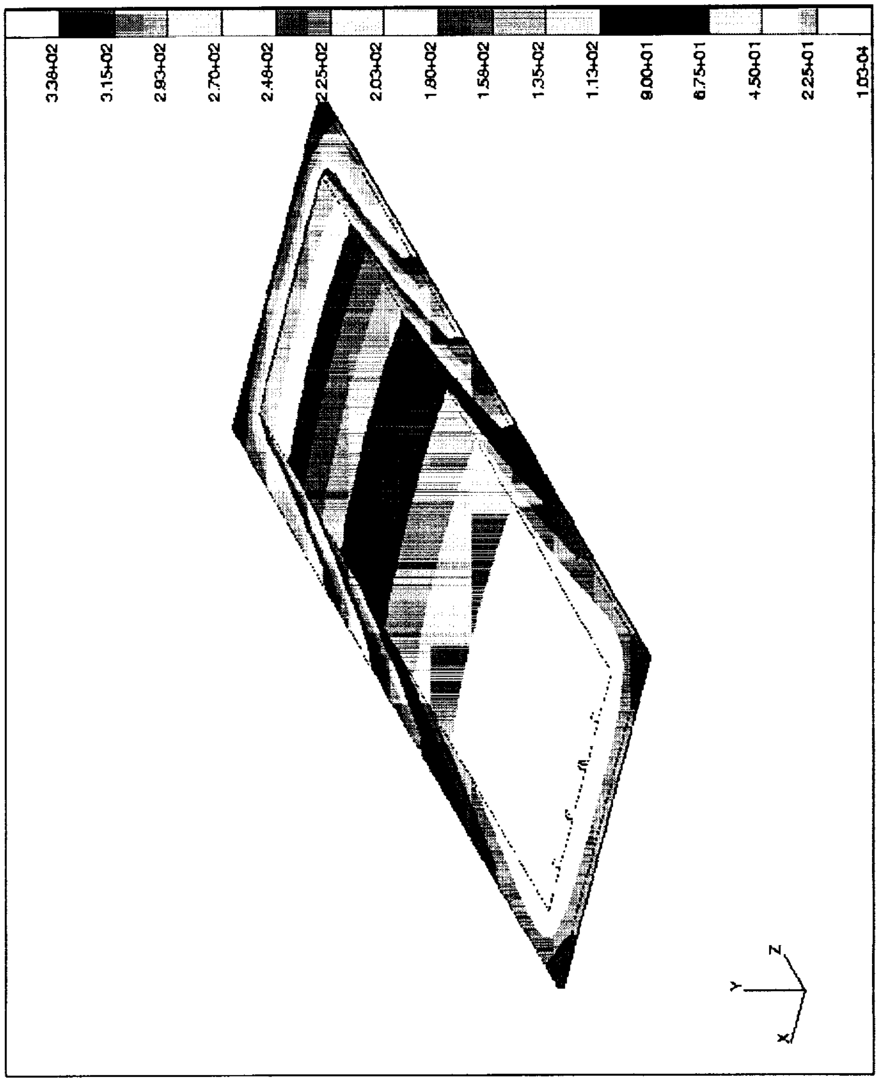

Figure 5.23 Flow front simulation of a 10-ply, 1523 E-glass/510A-40 composite panel with a capillary pressure of 5.6 kPa. The colored bands represent the flow front location as a function of time, in seconds. The simulated infiltration time was 338 seconds.

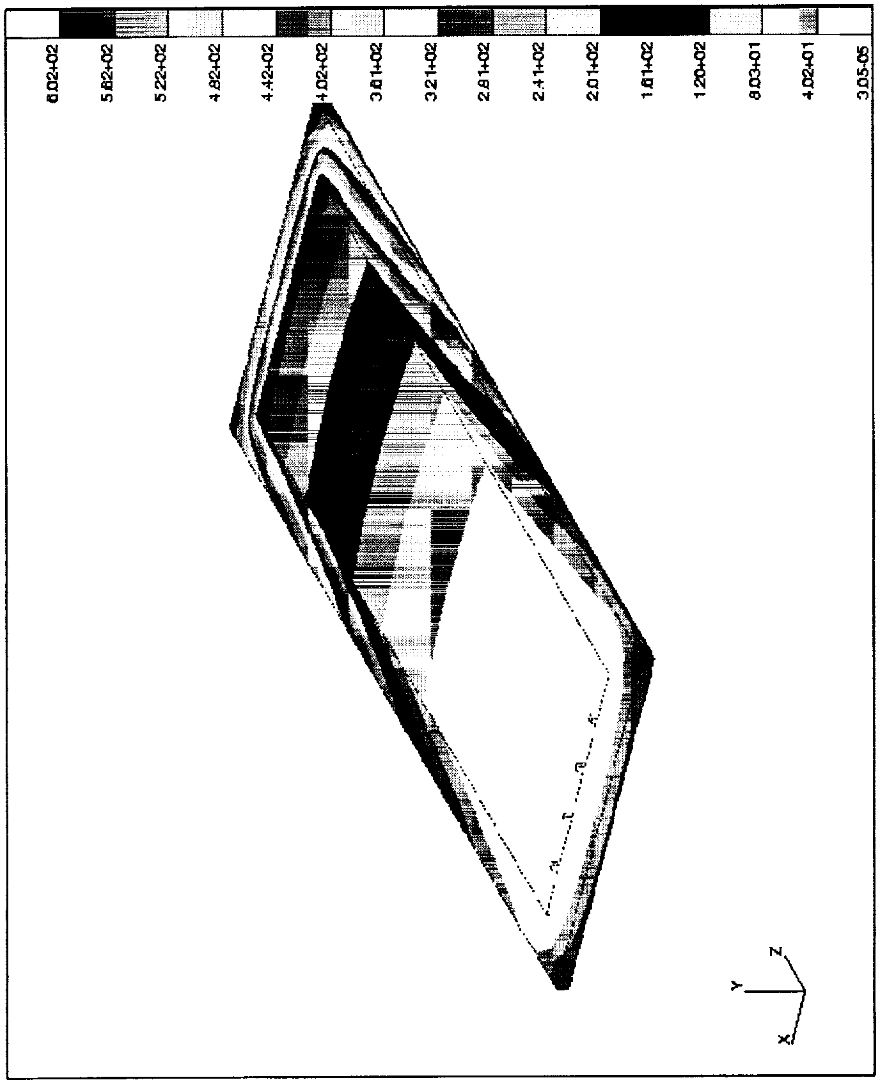

Figure 5.24 Flow front simulation of a 20-ply, 1523 E-glass/510A-40 composite panel with a capillary pressure of 5.6 kPa. The colored bands represent the flow front location as a function of time, in seconds. The simulated infiltration time was 602 seconds.

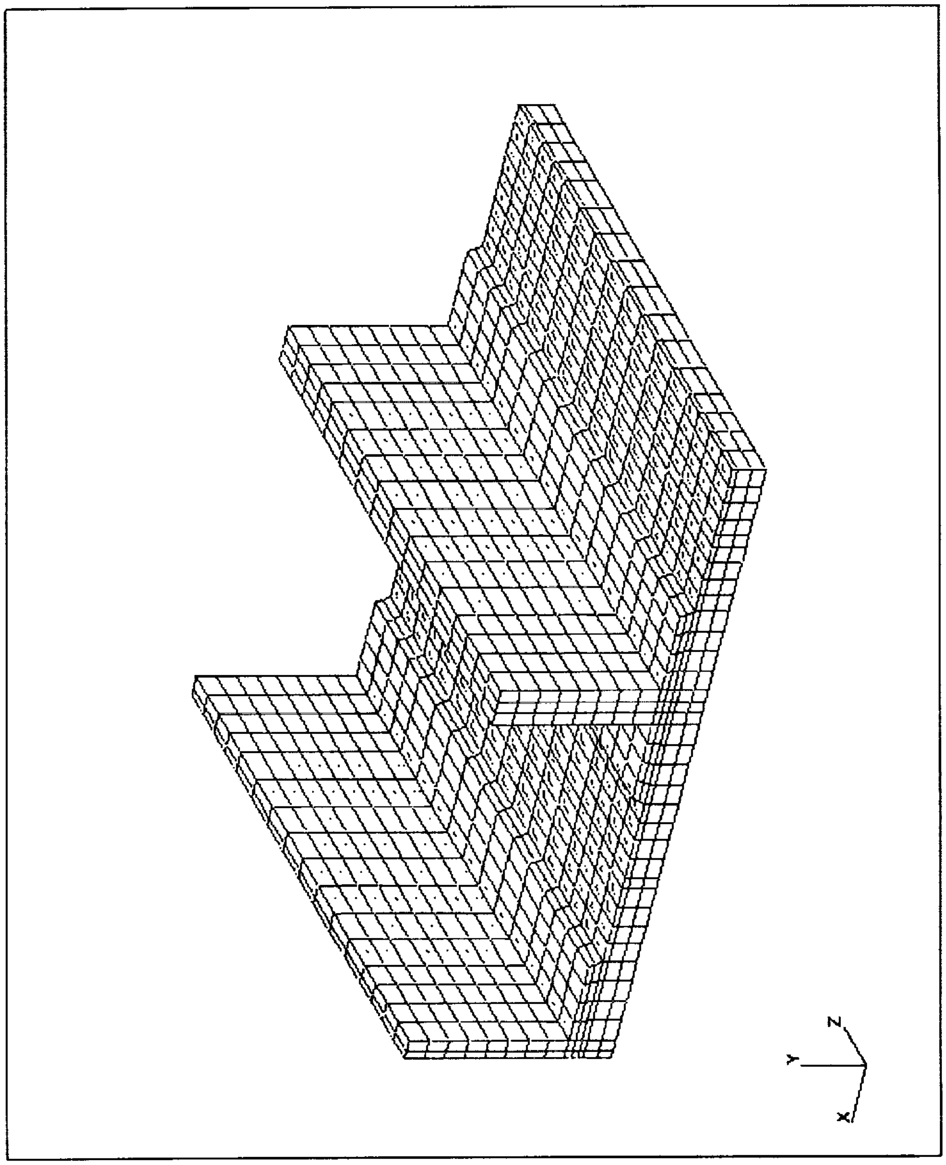

Figure 5.25 Finite element mesh of a three-stiffener preform. This mesh consisted of 4,046 nodes and 2,864 elements.

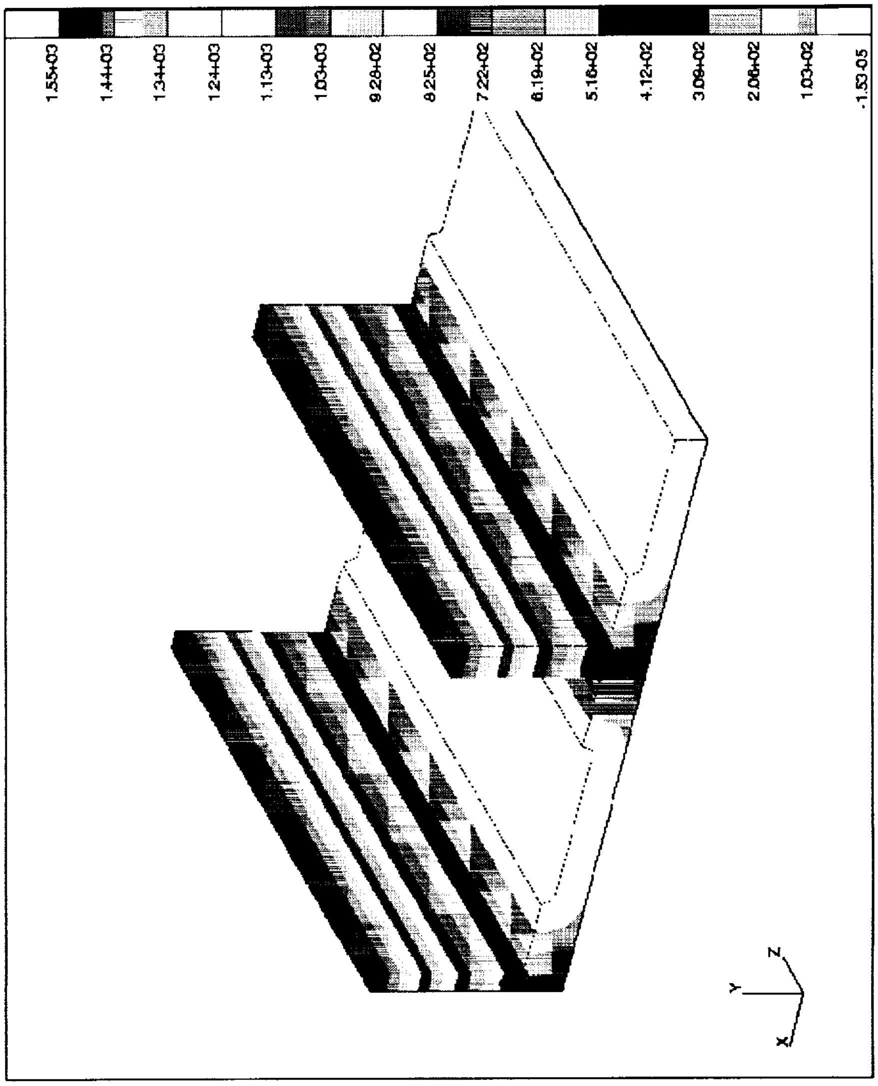

Figure 5.26 Flow front simulation of a three-stiffener composite panel with SC-36 without gravity. The colored bands represent the flow front location as a function of time, in seconds. The simulated infiltration time was 1,547 seconds.

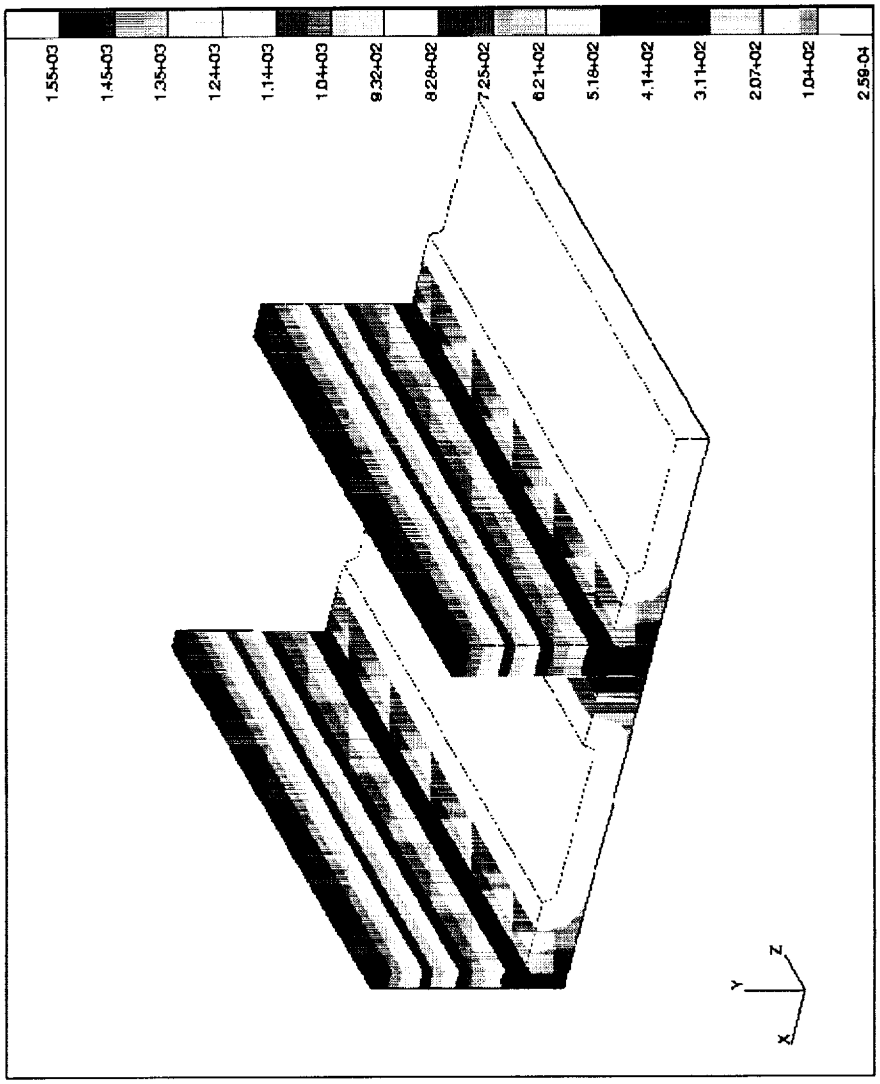

Figure 5.27 Flow front simulation of a three-stiffener composite panel with SC-36 and gravity acting in -y. The colored bands represent the flow front location as a function of time, in seconds. The simulated infiltration time was 1,553 seconds.

Table 5.1 Four-Point Flexural Results of Composite Panels

Composite Panel	Strength (MPa)	Modulus (GPa)
1523 E-glass/510A-40 (longitudinal and transverse)	293±19	28.5±1.8
4-tube/L-10 (transverse)	315±12	25.6±1.0
4-tube/L-10 (longitudinal)	559±15	51.1±4.0
4-tube/SC-36 (transverse)	289±9	22.0±1.4
4-tube/SC-36 (longitudinal)	640±69	45.2±2.7

Chapter 6 VARTM Process Analysis

The 3DINFIL computer code is a powerful process analysis tool. A process analysis tool enables the user to determine such important process constraints as the location and type of injection ports and the permeability and location of the high-permeable media. In this chapter, boundary condition modifications were performed to illustrate the capabilities of the computer code as a process analysis tool.

6.1 Injection Port Location

The effect of injection port location on preform infiltration was evaluated using the model for the 14-tube center-lock braided preform infiltrated with the 510A-40 resin system as a basis (See Section 5.2). The locations of the four injection ports were moved to new positions on the preform, and the infiltration results were compared with the original model which incorporated the injection ports at the edge of the preform (Figure 5.22).

The first case examined was to simply move the four resin injection ports from the edge of the high-permeable medium to the center of the high-permeable medium. Figure 6.1 shows the finite element mesh for this case, and Figure 6.2 shows the modeled results.

This configuration was a vast improvement over the original case, reducing infiltration time by 48%.

The second case examined was to position the four resin injection ports along the longitudinal axis of the preform. The injection ports were now aligned perpendicular with the original case, but remained in the center of the high-permeable medium. Figures 6.3 and 6.4 display the mesh and modeled results, respectively. This configuration was a further improvement compared to the original case, reducing processing time by more than 50%.

It can be seen from the center-injection configurations that the flow front patterns are becoming more parallel with the tool plate as the flow proceeds through the thickness of the preform. This was not the case with the original configuration, Figure 5.22, which shows an irregular flow pattern through the thickness of the preform. These irregular patterns can cause void entrapment when the uneven flow fronts coalesce. The new center-injection configurations produce a more desirable infiltration condition because they do not allow for great amounts of void entrapment due to irregular flow front patterns.

6.2 Injection Port Type

The effect of injection port type was investigated by replacing the individual resin inlet ports (point source) with an injection tube (line source). The resin injection tube was 27.66 cm long and 1.27 cm wide, and based on the configurations for injection port location discussed in Section 6.1, was placed in the center of the high-permeable medium. Figure 6.5 shows the finite element mesh of this model. For the 14-tube preform, the line source configuration resulted in a 64% reduction in infiltration time compared to the original point source configuration shown in Figure 5.22. In addition to the reduction in infiltration time, the flow front patterns through the thickness of the preform were more uniform than any of the other cases investigated. The resin flow front was almost parallel to the tool plate during infiltration.

6.3 High-Permeable Resin Distribution Medium Permeability

The permeability of the high-permeable medium was changed from that of the nylon, 2.92 E-09 m^2, to that of the Seemann reusable bag material, 3.45 E-09 m^2 (these permeability values were reported in Section 3.1). This change had very little effect on the modeled results using the line source configuration of Section 6.2. The infiltration time was reduced by only 1% compared to the nylon model in Section 6.2, and the flow front pattern was virtually the same. These results are shown in Figure 6.7.

6.4 High-Permeable Resin Distribution Medium Location

The location of the high-permeable distribution medium was examined using a model of a one-stiffener preform. This modeled preform consisted of a 30.48 cm long by 20.35 cm wide by 1.43 cm thick multiaxial warp knit skin and one 9.05 cm high, 14-tube surface-lock braided stiffener. This model was constructed to have a geometry complicated enough to see the effect of changing the medium location but simple enough to save computational time. Due to geometric symmetry, only one-quarter of the preform was modeled. Four different high-permeable medium locations were examined. The permeability of the Seemann high-permeable distribution medium was used in the simulations.

In the first simulation model, the high-permeable medium was placed on the preform skin parallel with the tool plate (Figure 6.8). The model predicted an infiltration time of 1,529 seconds, and a uniform resin flow front throughout the skin, flange, and stiffener regions (Figure 6.9). This model also illustrated that a single vacuum port along the top of the stiffener would be sufficient.

In the next model, the high-permeable medium was located on the flange of the preform, parallel with the tool plate (Figure 6.10). Although this model predicted a 20% decrease in infiltration time (Figure 6.11) compared to the first case, it is probably not the best overall configuration. One reason for this is that two vacuum ports are required. One vacuum port would be necessary to pull the resin up into the stiffener, while a second vacuum port would be necessary to allow the resin to infiltrate the corners of the skin. Another problem with this configuration is the potential for void entrapment. When injection occurs in the flange region, voids may become entrapped by the merging of two mirror-image flow fronts. Only one flow front is depicted in Figure 6.11 because of symmetry.

In the third model, the high-permeable medium is located both on top of the flange, as described in case two, and also on part of the stiffener, perpendicular to the flange. The medium forms an “L” with both sections of equal length. Figure 6.12 shows the finite element mesh used for this configuration. This configuration was created in order to decrease infiltration time compared to the last case. The simulation is shown in Figure 6.13. The infiltration time was reduced by only 1% over the last configuration, and still had all of the same problems as before, i.e. multiple vacuum ports and possible void entrapment.

The final configuration examined the placement of the high-permeable medium on the top of the stiffener, shown in Figure 6.14. The simulation showed that a uniform flow front would result, and only one vacuum port would be required for complete preform infiltration (Figure 6.15). The only draw back was in the total infiltration time. The time required to fill the preform was nearly 4.5 times longer than the first case.

6.5 VARTM of a Three-Stiffener Preform

A simulation model for resin infusion of a three-stiffener preform by the VARTM process was constructed. Details of the three-stiffener preform are given in Section 5.1. The results of the VARTM process analysis study in Sections 6.1 through 6.4 were used as a guide in the placement of the high-permeable distribution medium and resin injection and vacuum ports. The model incorporated a Seemann high-permeable distribution medium located on the preform skin with a resin injection line in the center of the medium. Also, vacuum lines were located on top of the stiffener surfaces parallel with the tool plate. The finite element mesh is shown in Figure 6.16, and the results of the simulation are shown in Figure 6.17. The predicted infiltration time is 1,547 seconds. Coincidentally, this configuration was used to successfully infiltrate the three-stiffener composite panel discussed in Chapter 5.

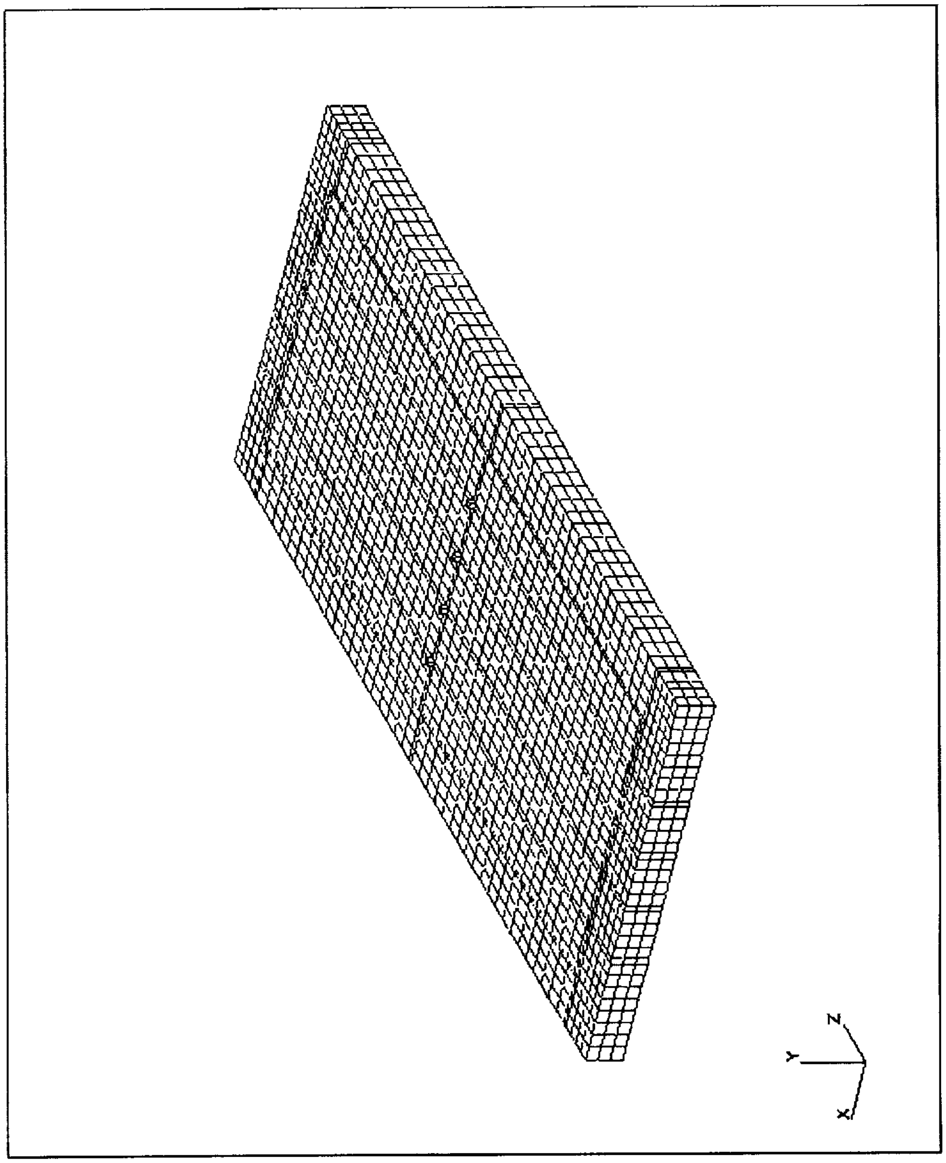

Figure 6.1 Finite element mesh of a 14-tube center-lock braided preform with four-port center-injection. This mesh consisted of 7,980 nodes and 5,932 elements.

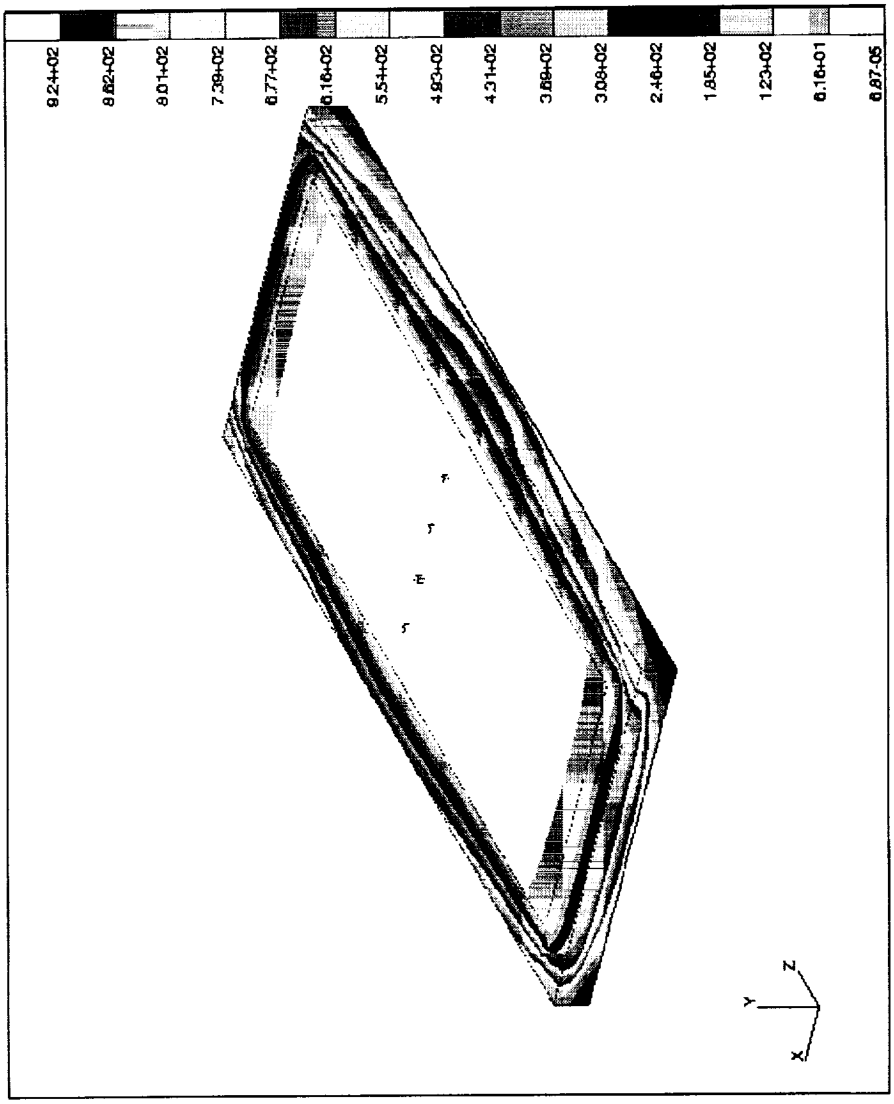

Figure 6.2 Flow front simulation of a 14-tube center-lock braided panel with four-port center-injection. The colored bands represent the flow front location as a function of time, in seconds. The simulated infiltration time was 924 seconds.

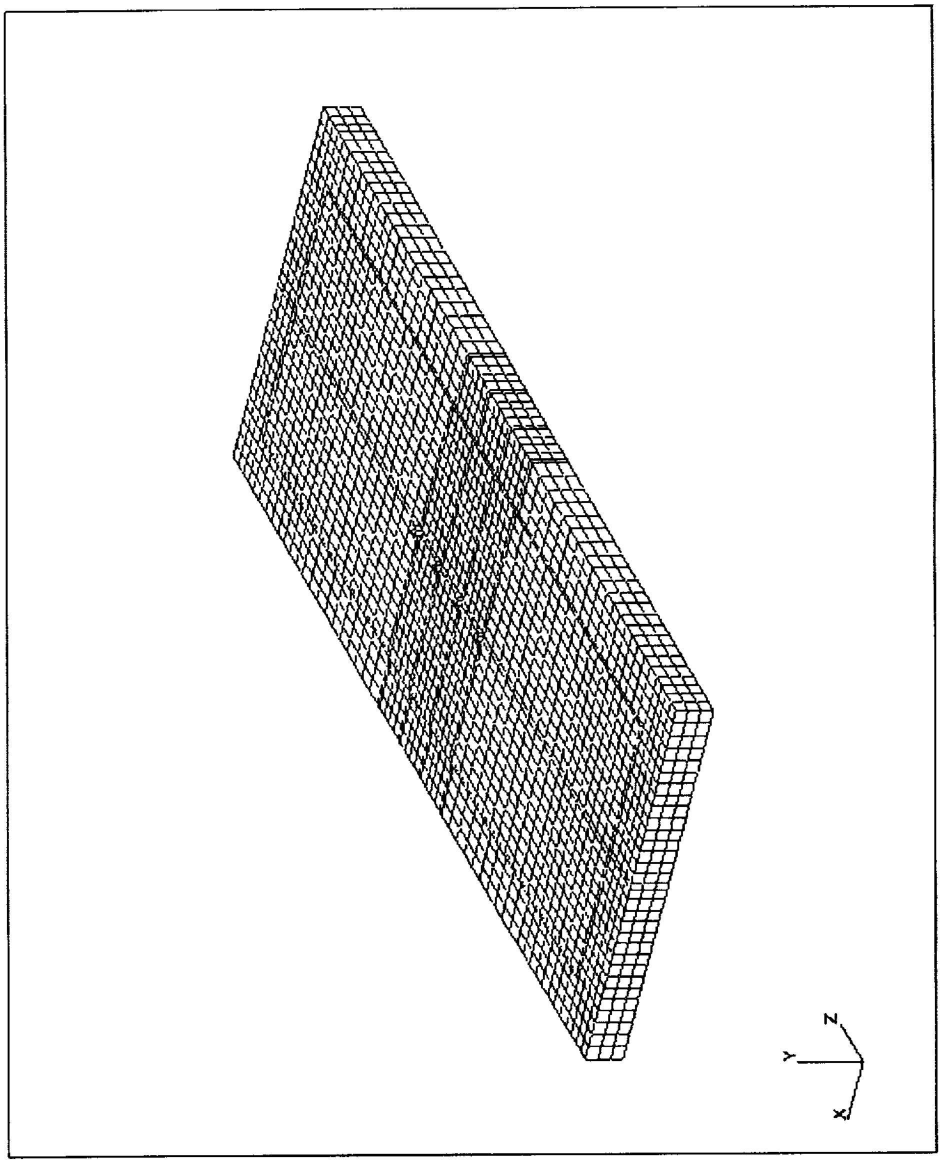

Figure 6.3 Finite element mesh of a 14-tube center-lock braided preform with four-port center-injection perpendicular to edge-injection. This mesh consisted of 9,096 nodes and 6,780 elements.

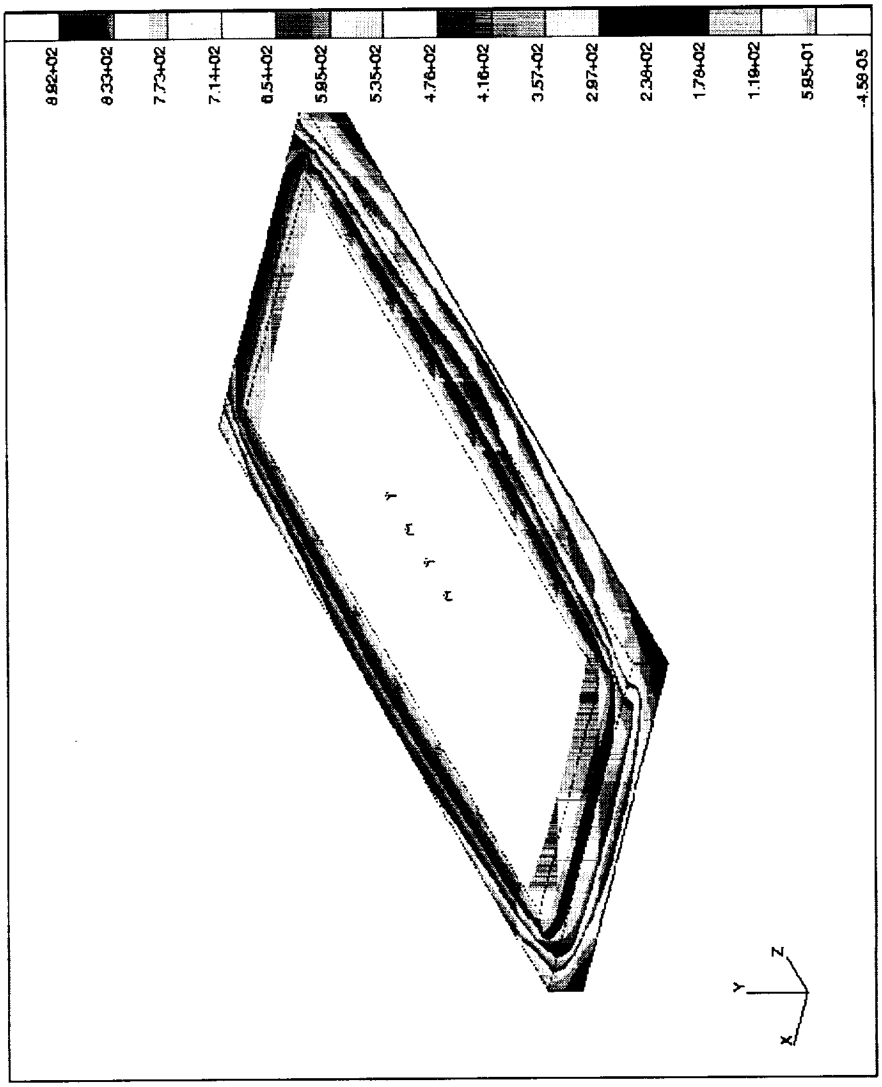

Figure 6.4 Flow front simulation of a 14-tube center-lock braided panel with four-port center-injection perpendicular to edge-injection. The colored bands represent the flow front location as a function of time, in seconds. The simulated infiltration time was 892 seconds.

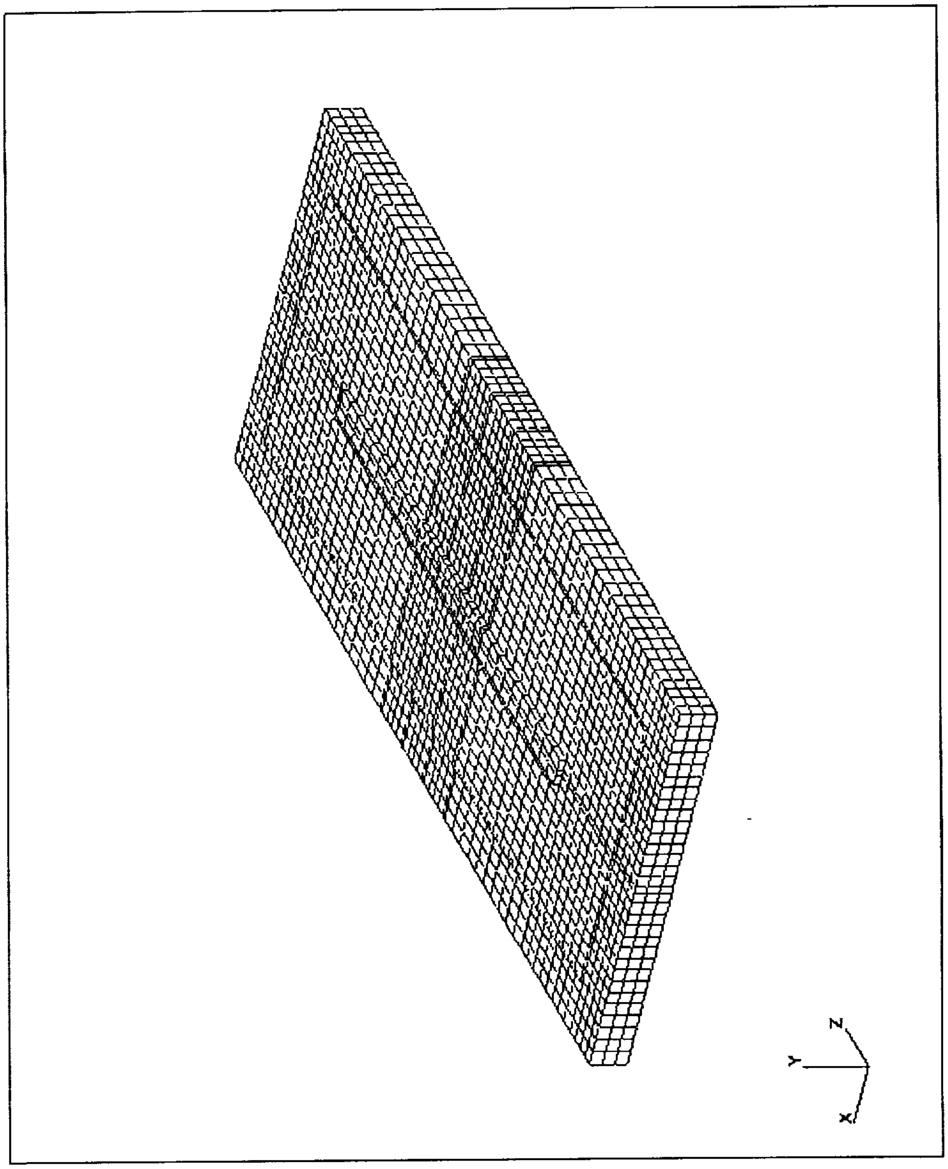

Figure 6.5 Finite element mesh of a 14-tube center-lock braided preform with line source injection. This mesh consisted of 9,228 nodes and 6,884 elements.

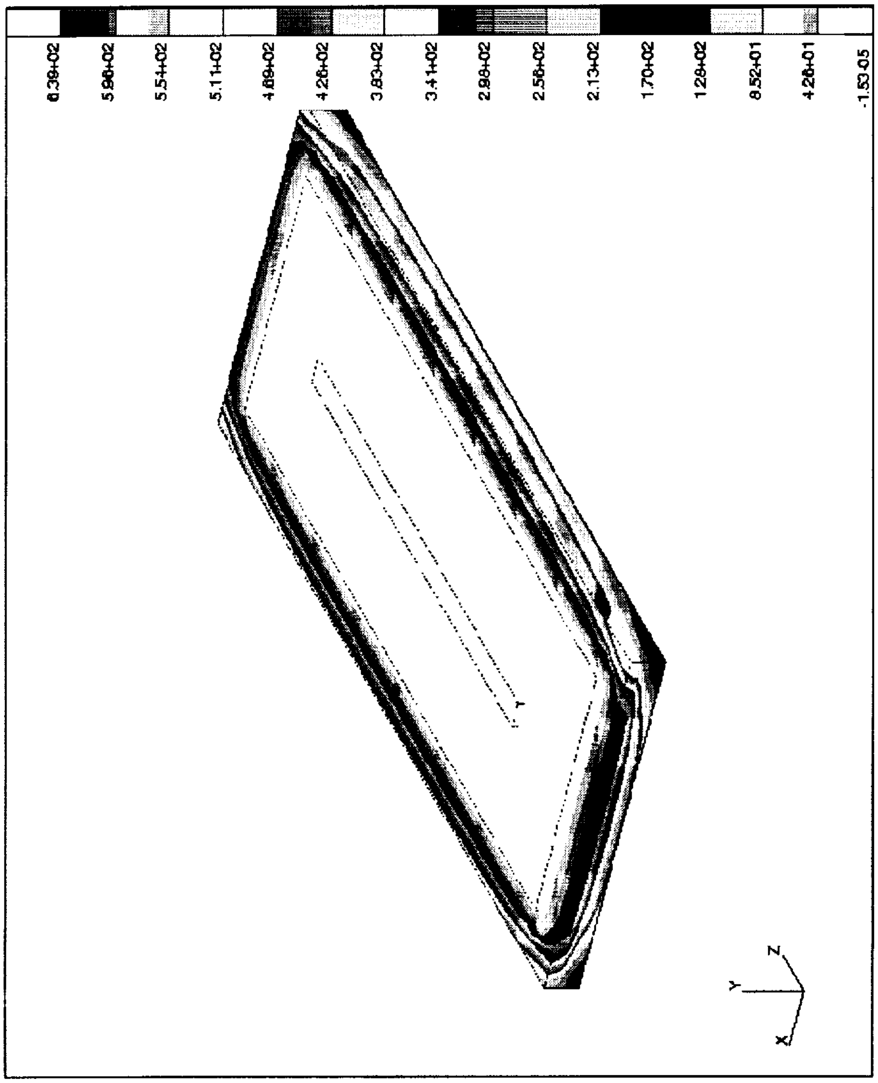

Figure 6.6 Flow front simulation of a 14-tube center-lock braided panel with line source injection and a nylon high-permeable medium. The colored bands represent the flow front location as a function of time, in seconds. The simulated infiltration time was 639 seconds.

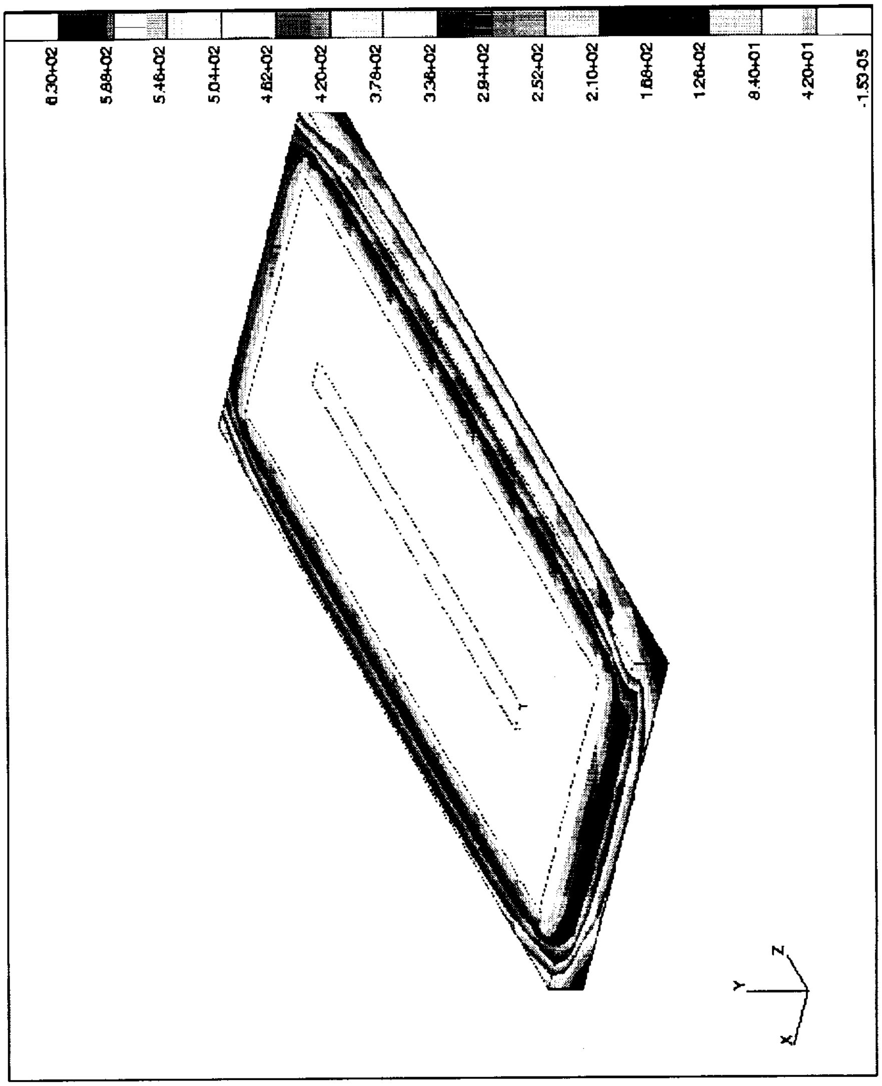

Figure 6.7 Flow front simulation of a 14-tube center-lock braided panel with line source injection and a Seemann high-permeable medium. The colored bands represent the flow front location as a function of time, in seconds. The simulated infiltration time was 630 seconds.

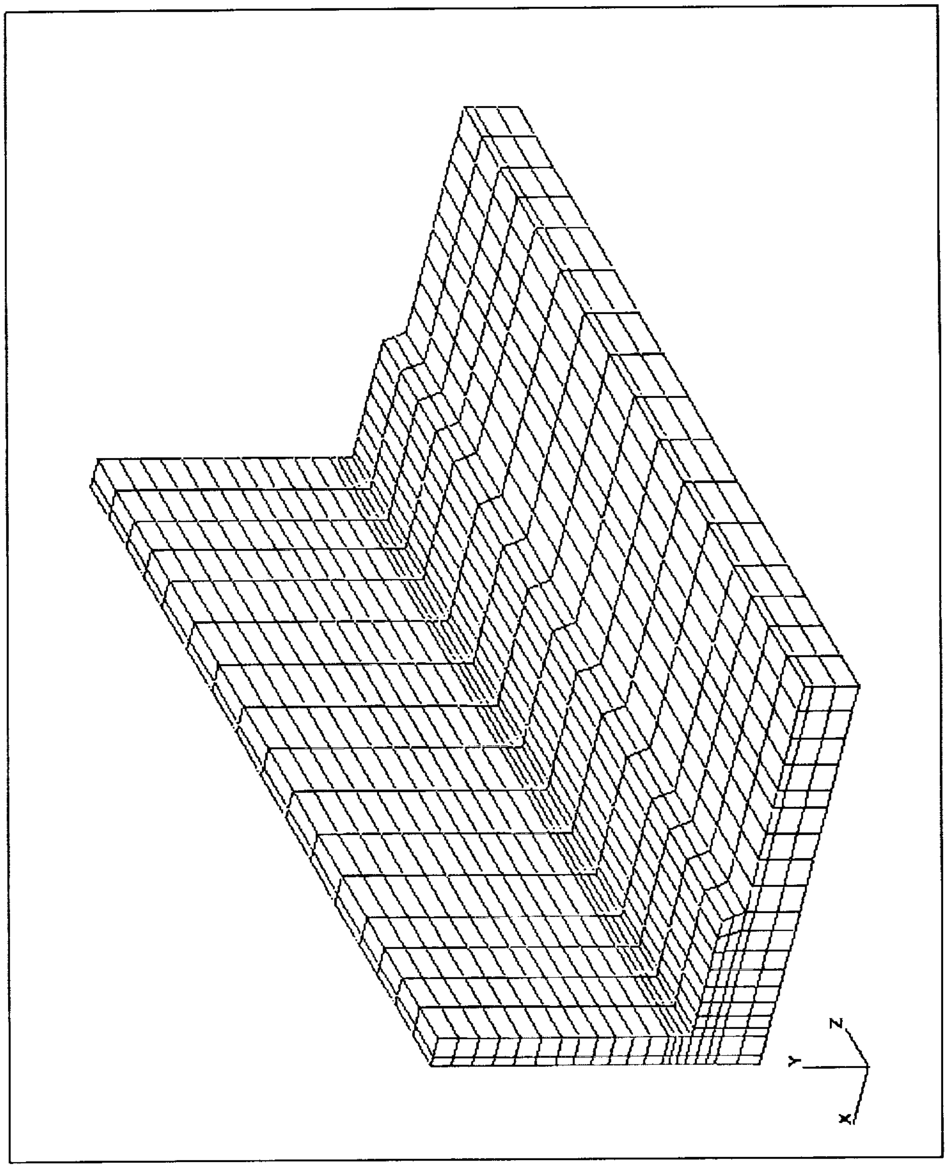

Figure 6.8 Finite element mesh of a one-stiffener preform with the high-permeable medium located on the preform skin. This mesh consisted of 2,499 nodes and 1,712 elements.

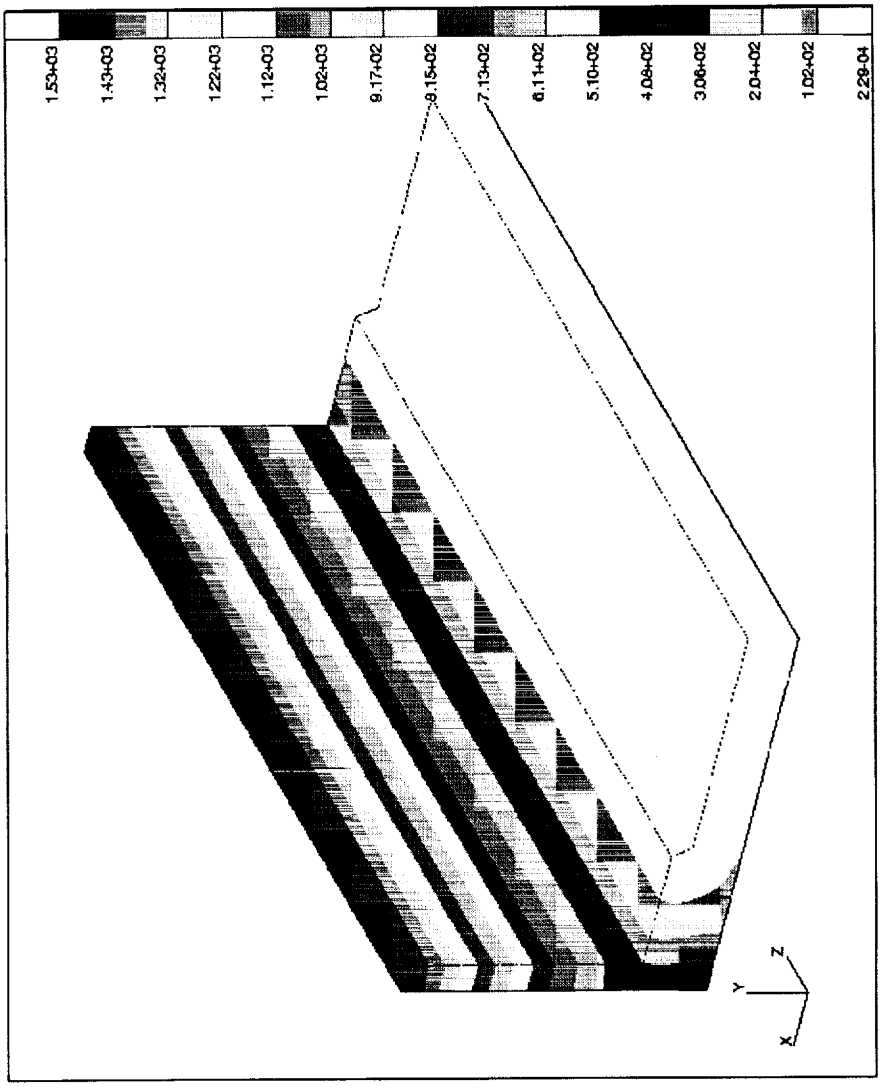

Figure 6.9 Flow front simulation of a one-stiffener panel with the high-permeable medium located on the preform skin. The colored bands represent the flow front location as a function of time, in seconds. The simulated infiltration time was 1,529 seconds.

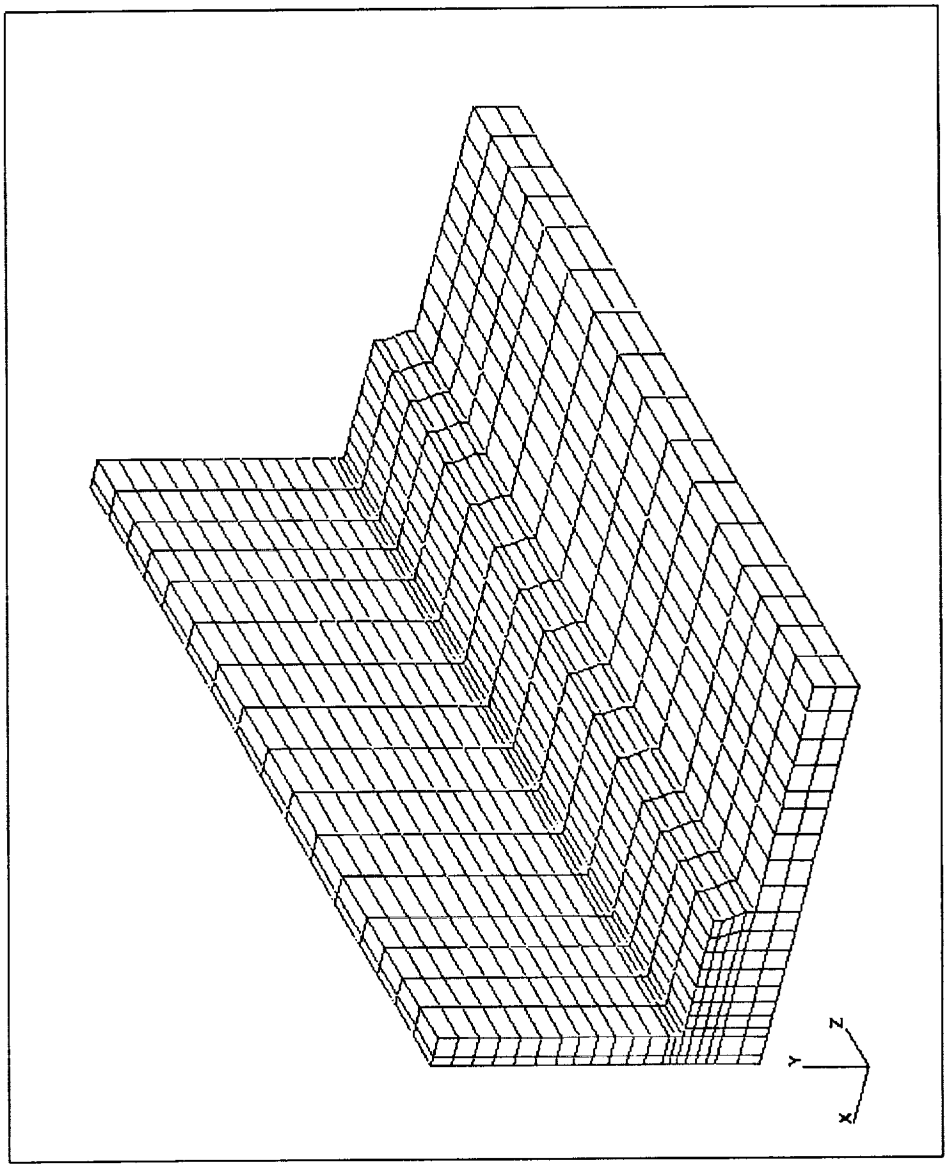

Figure 6.10 Finite element mesh of a one-stiffener preform with the high-permeable medium located on the flange. This mesh consisted of 2,482 nodes and 1,696 elements.

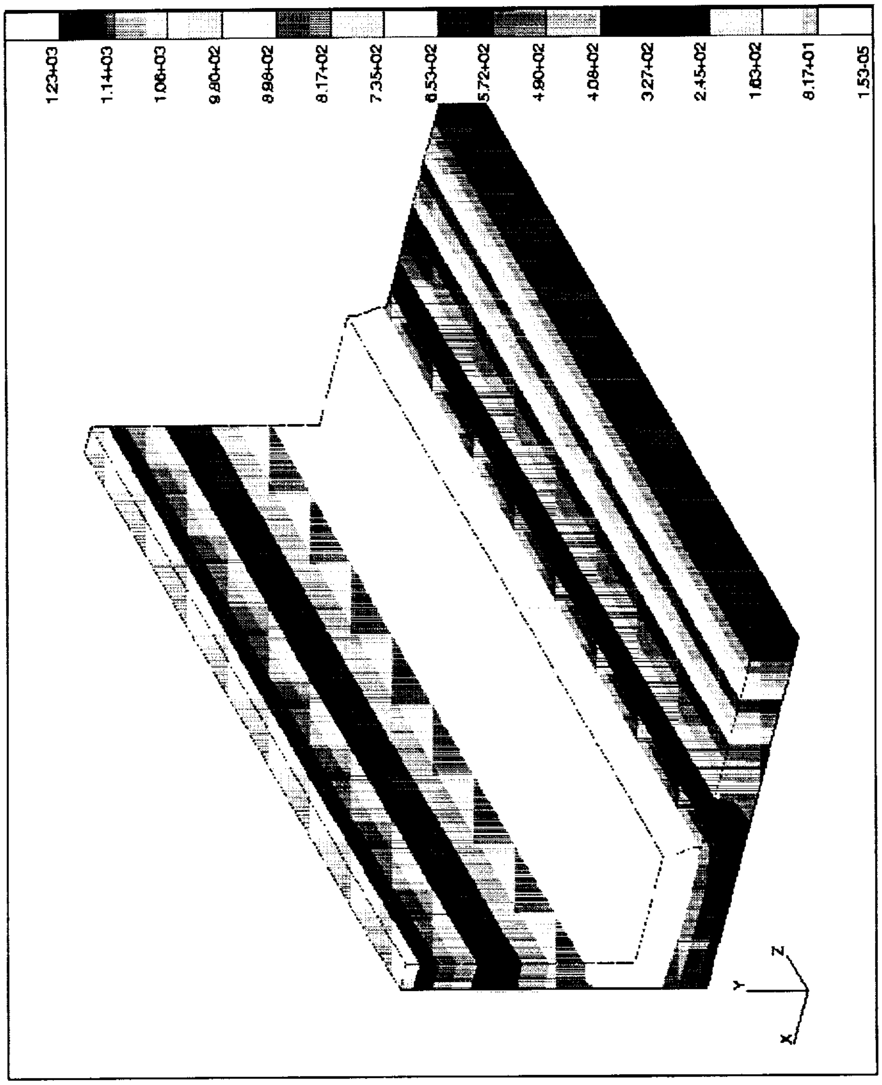

Figure 6.11 Flow front simulation of a one-stiffener panel with the high-permeable medium located on the flange. The colored bands represent the flow front location as a function of time, in seconds. The simulated infiltration time was 1,225 seconds.

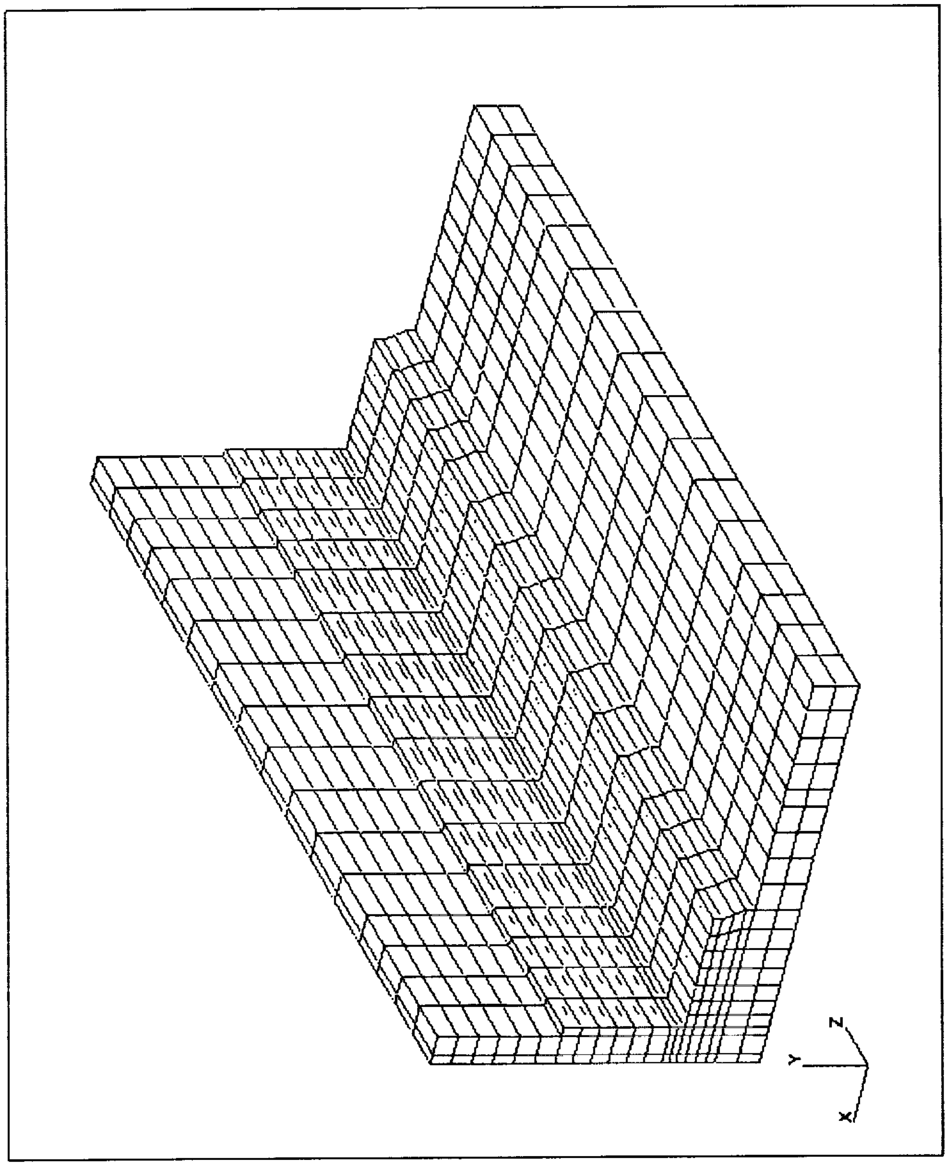

Figure 6.12 Finite element mesh of a one-stiffener preform with the high-permeable medium located on the flange and stiffener. This mesh consisted of 2,618 nodes and 1,824 elements.

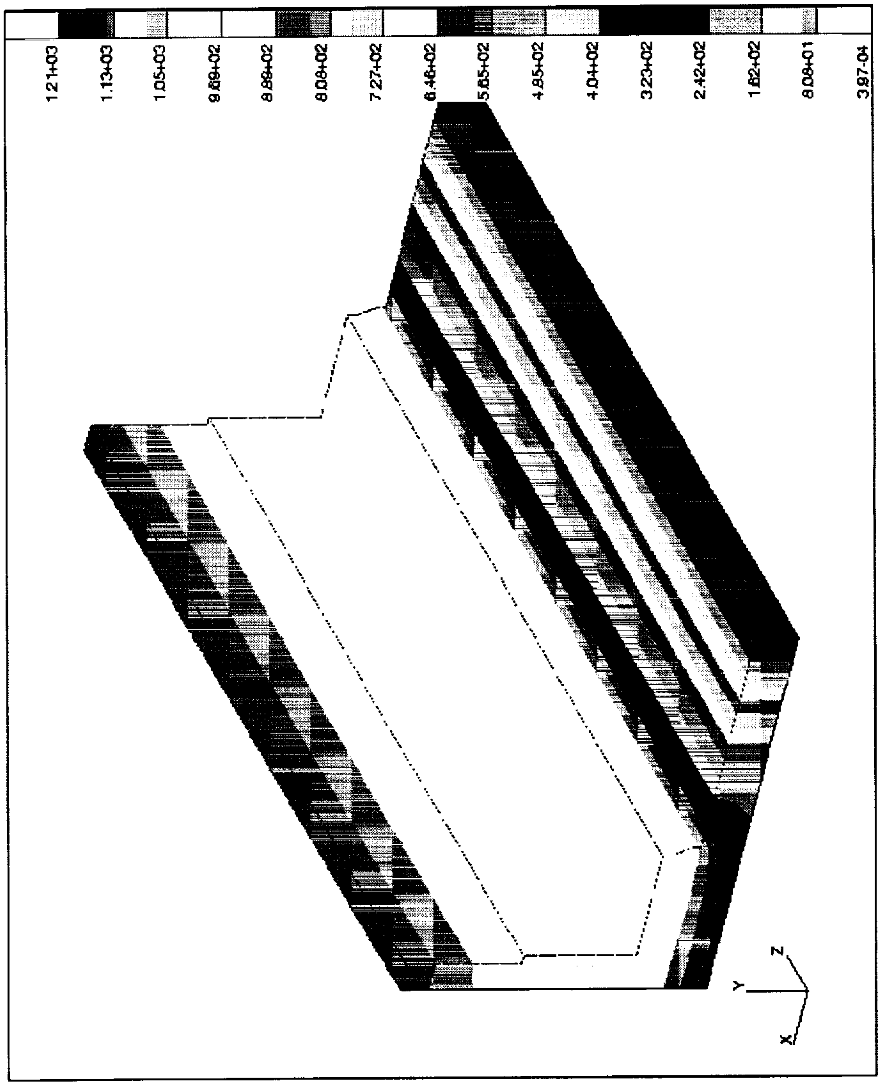

Figure 6.13 Flow front simulation of a one-stiffener panel with the high-permeable medium located on the flange and stiffener. The colored bands represent the flow front location as a function of time, in seconds. The simulated infiltration time was 1,212 seconds.

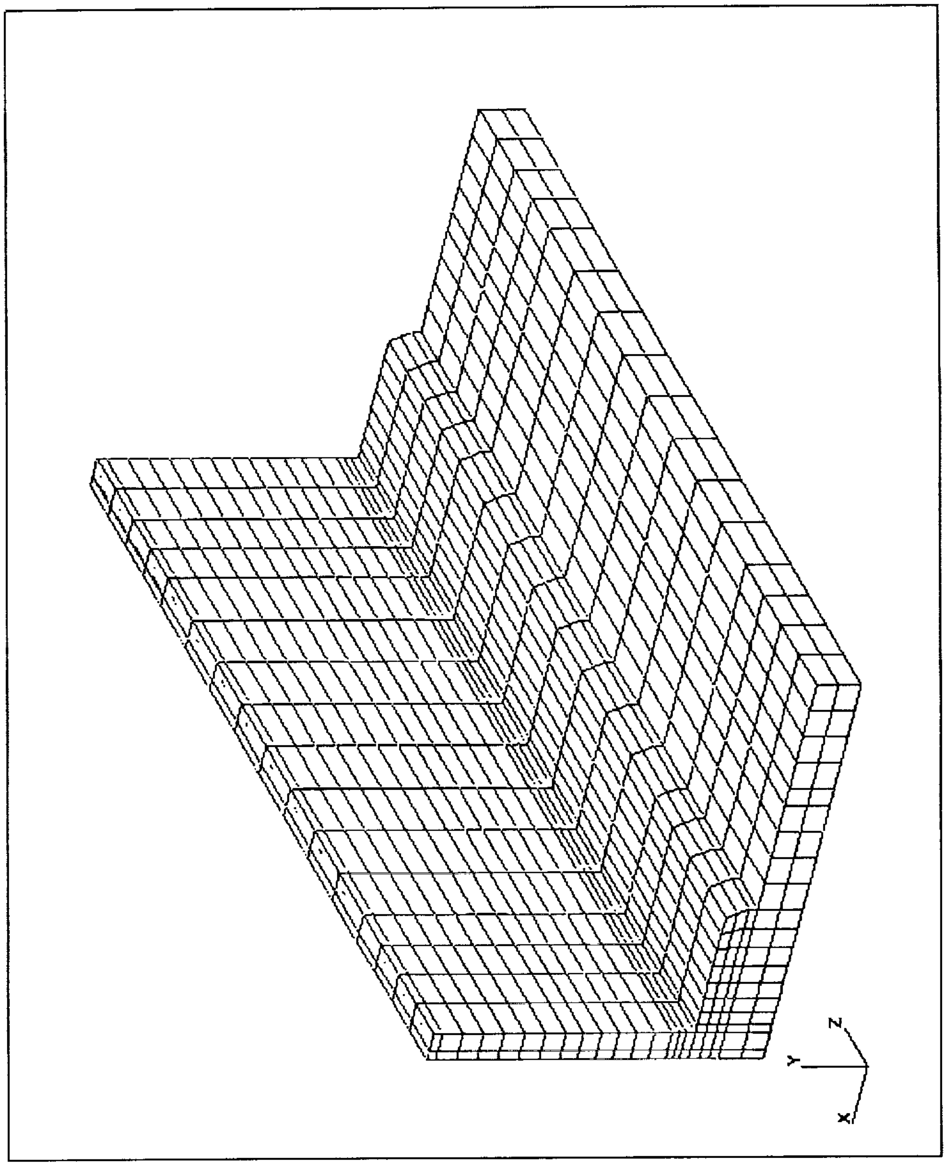

Figure 6.14 Finite element mesh of a one-stiffener preform with the high-permeable medium located on top of the stiffener. This mesh consisted of 2,397 nodes and 1,600 elements.

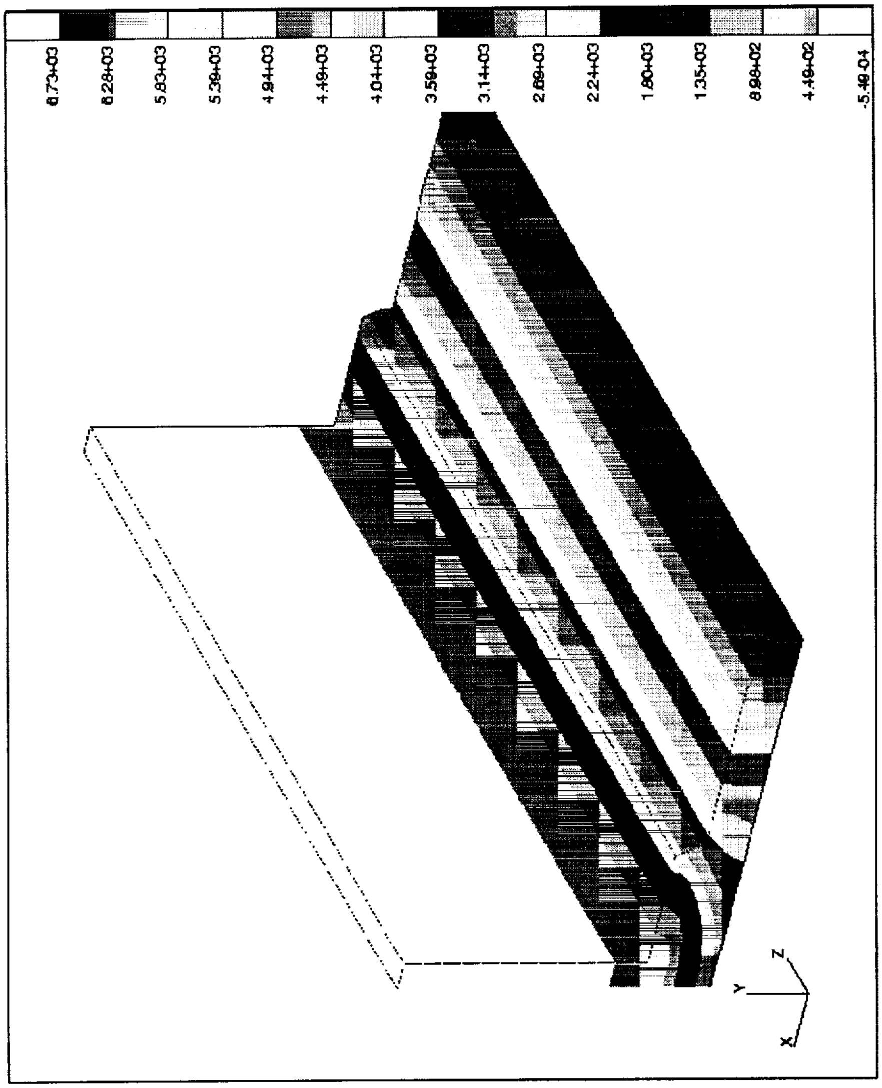

Figure 6.15 Flow front simulation of a one-stiffener panel with the high-permeable medium located on top of the stiffener. The colored bands represent the flow front location as a function of time, in seconds. The simulated infiltration time was 6,732 seconds.

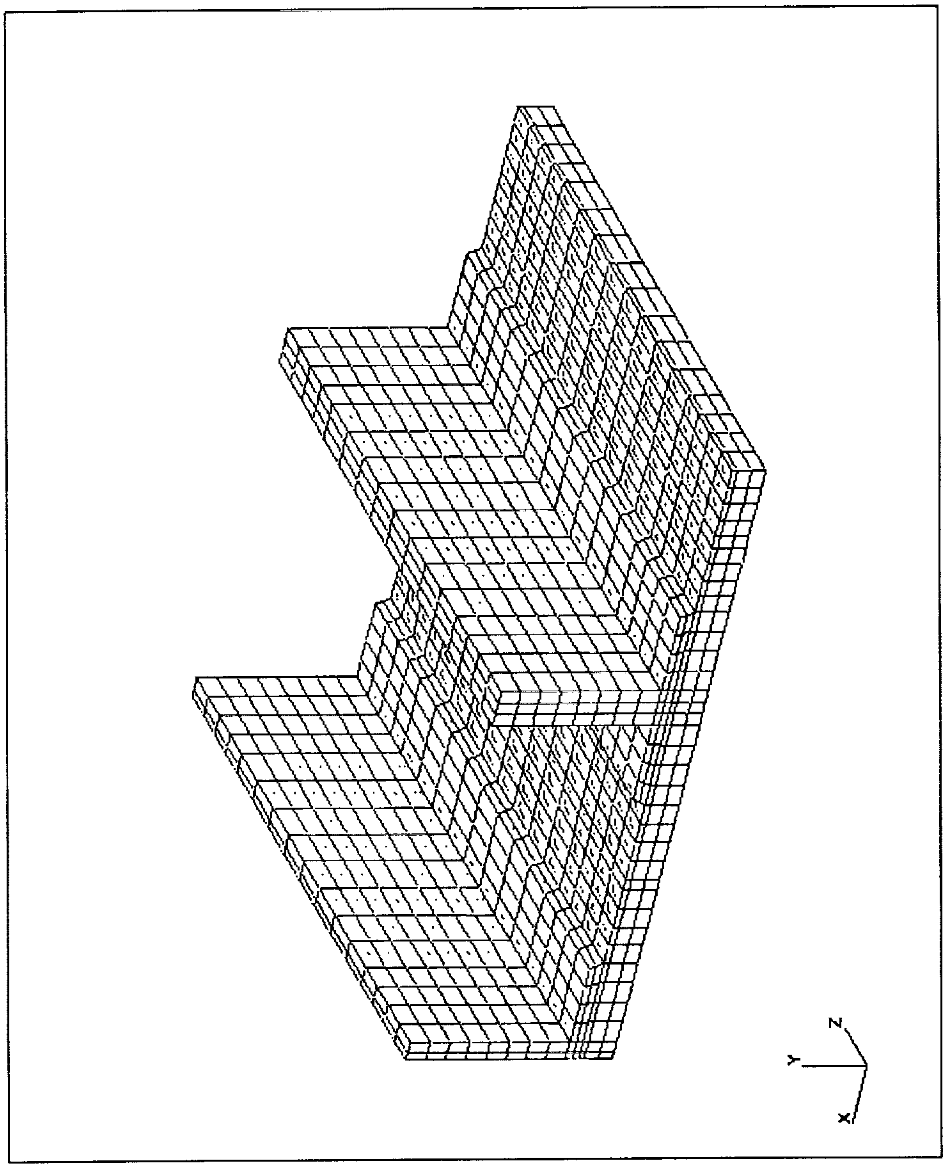

Figure 6.16 Finite element mesh of a three-stiffener preform with the high-permeable medium located on the preform skin. This mesh consisted of 4,046 nodes and 2,864 elements.

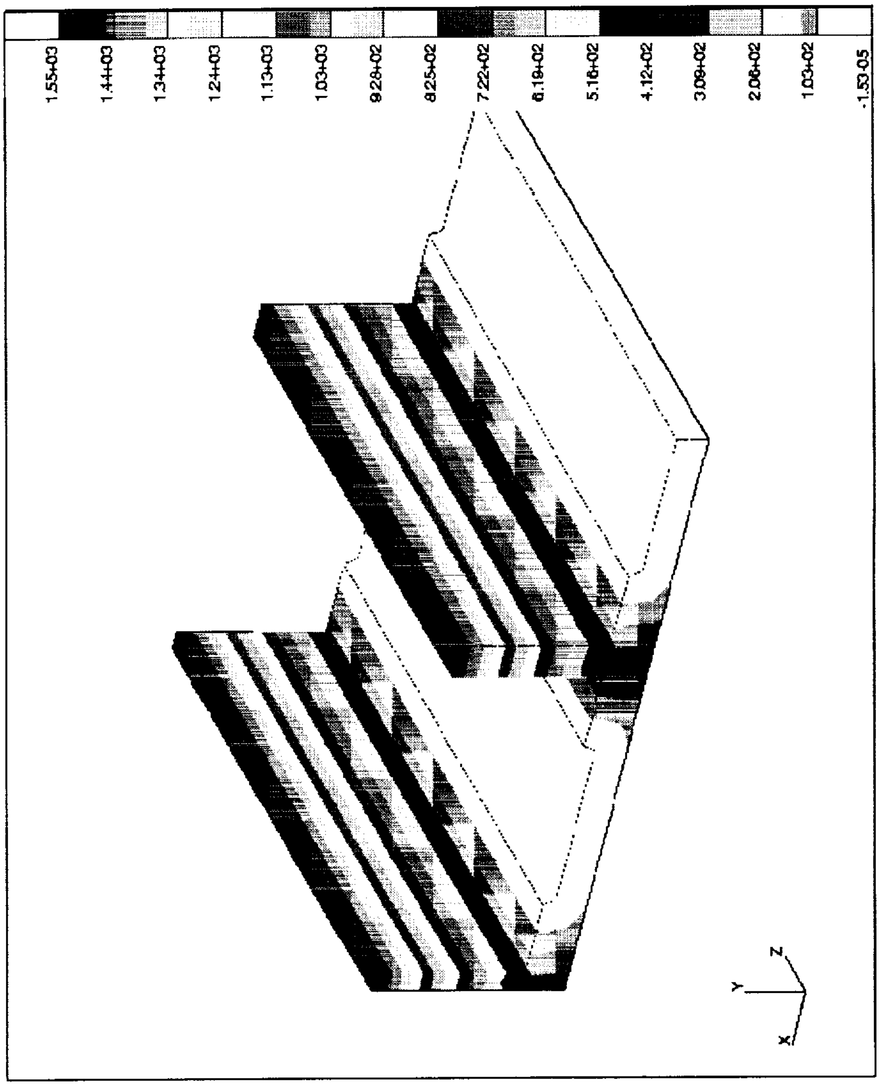

Figure 6.17 Flow front simulation of a three-stiffener panel with the high-permeable medium located on the preform skin. The colored bands represent the flow front location as a function of time, in seconds. The simulated infiltration time was 1,547 seconds.

Chapter 7 Summary

Vacuum-Assisted Resin Transfer Molding (VARTM) has evolved from Resin Transfer Molding (RTM) technologies in order to overcome some of RTM's inherent flaws. In the VARTM process, a vacuum bag is used as one of the tool surfaces. This eliminates the need for precise matched-metal mold making that is crucial in conventional RTM. The exact fit of the vacuum bag to the preform drastically reduces resin rich areas, and it also allows for a more efficient way of trapping and controlling VOC emissions. A final advantage of VARTM lies in the low injection pressures (~1 atm). These low pressures allow for little movement of the reinforcement during processing, which produces a better quality part. The VARTM process is currently implemented in the manufacturing of Naval structural components (masts, hulls, and bridgedecks), automobile chassis and body components, transportation infrastructure, railroad cars, and turbine blades.

A great deal of work still needs to be done on efforts to reduce the costly trial-and-error methods of VARTM processing that are currently in practice today. A computer simulation model of the VARTM process would provide a cost-effective tool in the manufacturing of composites utilizing this technique. Therefore, the objective of this work was to develop and verify a three-dimensional, VARTM model and to use this model as a process analysis tool.

The permeability is an important preform material property required in many composite processing flow simulations. This quantity is defined as the property of a porous material which characterizes the ease with which a fluid may be made to flow through the material by an applied pressure gradient. Both, the steady-state and advancing front permeability measurement techniques were utilized in this work. These techniques were based on Darcy's Law:

$$q_i = -\frac{S_{ij}}{\eta}\frac{\partial P}{\partial x_j}$$

where, q_i is the i^{th} component of the superficial velocity vector of the fluid, S_{ij} is the permeability tensor of the porous medium, η is the viscosity of the fluid, and $\frac{\partial P}{\partial x_j}$ is the pressure gradient across the porous medium.

Three derivatives of the steady-state and advancing front permeability measurement techniques were implemented in order to determine the validity of using one technique over another. These derivatives were:

1. Steady-state, constant flow rate, closed, steel mold
2. Advancing front, constant flow rate, closed, steel mold

3. Advancing front, constant pressure, open-faced, aluminum tool plate with vacuum bag

In-plane permeability measurements of both the warp and fill directions were performed for a 10-ply, glass fabric preform. The results showed there was no decisive advantage in using one technique over another. The preferred permeability measurement technique was the steady-state, constant flow rate technique due to its proven success and its ease of use. This technique was used to determine the in-plane and transverse permeabilities for all fiber systems.

The permeabilities of the high-permeable distribution media were also measured. Due to the high permeability of these materials, a new permeability measurement protocol had to be devised. This protocol consisted of two separate measurements. A radial flow, advancing front technique with a center-port injection was first used to determine the orientation of the in-plane principal axes. Then, the in-plane principal permeabilities of the high-permeable distribution media were measured using the advancing front, constant pressure permeability measurement technique.

A finite element code exists at Virginia Tech, which is named 3DINFIL. It is a comprehensive, three-dimensional, computer simulation model of the Resin Film Infusion (RFI) and RTM processes. The three-dimensional flow model calculates the pressure and velocity fields of the resin in the preform, and uses this information to track the progression of the flow front during processing. An experimental VARTM process was developed for the lab environment to verify this computer model. Several flat panels were produced to verify the flow front patterns and infiltration times of the modeling effort. Quality assessment was also carried out on these panels. This assessment included the degree of cure, optical microscopy, C-scanning, and flexural testing.

Modifications to 3DINFIL were made to account for the low injection pressures (~1 atm) used in VARTM processing. These modifications were incorporated by the following two changes:

1. The boundary condition at the flow front was modified to incorporate capillary pressure:

$$P_{flowfront} = \frac{2}{r_h}\gamma_{lv}\cos\theta$$

where, r_h is the hydraulic radius of the fiber bundle, defined as the cross-sectional area normal to flow divided by the perimeter presented to the fluid.

2. The governing differential equation was modified to incorporate gravity:

$$\frac{\partial}{\partial x_i}\left(\frac{S_{ij}}{\eta}\frac{\partial P}{\partial x_j}-\frac{S_{ij}}{\eta}\rho g_j\right)=0$$

The capillary pressure model showed the capability to substantially reduce the original simulated infiltration times. Gravity, on the other hand, was proven to be negligible for all cases.

Finally, the VARTM model was used as a process analysis tool. This enabled the user to determine such important process constraints as the location and type of injection ports and the permeability and location of the high-permeable media. A process for the three-stiffener composite panel was proposed. This configuration evolved from the variation of the process constraints in the modeling of simple flat panels, followed by more complicated one-stiffener panels. The configuration was proposed by considering such factors as: infiltration time, the number of vacuum ports, and possible areas of void entrapment.

Chapter 8 Conclusions

An existing three-dimensional, RFI/RTM model was modified to include VARTM simulation capabilities. Verifications were first performed to determine the accuracy of the flow front patterns and infiltration times. The flow front patterns were determined to be qualitatively accurate in both the high-permeable medium and the preform itself, demonstrating not only the "leaking" flow behavior, but also the last points to fill. Simulated infiltration times over predicted experimental times by 8 to 10% for all panels.

The influence of the capillary pressure and gravity on simulated infiltration times was also examined. The theoretical capillary pressure showed the capability to reduce the simulated infiltration times by as great as 6%. The gravity, on the other hand, was found to be negligible for all cases.

Finally, the VARTM model was used as a process analysis tool. This enabled the user to determine such important process constraints as the location and type of injection ports and the permeability and location of the high-permeable media. A process for a three-stiffener composite panel was proposed. This configuration evolved from the variation of the process constraints in the modeling of several different composite panels.

The configuration was proposed by considering such factors as: infiltration time, the number of vacuum ports, and possible areas of void entrapment.

References

(1) Hasko, G.H.; Dexter, H.B.; Loos, A.C.; Kranbuehl, D. *Journal of Advanced Materials* **1994**, 26 (1), 9-15.

(2) Lee, S.M., Ed. *International Encyclopedia of Composite Materials*; VCH: New York, 1990-91; 3, 108-118.

(3) Gabriele, M.C. *Plastics Technology* **1995**, 41 (3), 67-68.

(4) Seemann Composites' SCRIMP Promotional Information.

(5) Grossen, S. "Seemann Composites' Resin Infusion Molding Process" 1994, paper prepared for Dr. A.C. Loos, Virginia Tech.

(6) Mosher, P. *Book of Abstracts*, The 1996 ASME International Mechanical Engineering Congress and Exposition; ASME: New York, 1996; 74, 49-50.

(7) Gali, E. *Plastic Design Forum* **1982**, March/April, 47-56.

(8) Darcy, H. *Les Fontaines Publiques de la Villa de Dijon* **1856**.

(9) Fingerson, J.C. M.Sc. Thesis, Virginia Polytechnic Institute and State University, Blacksburg, VA, 1995.

(10) Carman, P.C. *Trans. Int. Chem. Eng.* **1937**, 15, 150-166.

(11) Kozeny, J. *Ber. Wien. Akad.* **1927**, 136a, 271.

(12) Gutowski, T.G.; Morigaki, T.; Cai, Z. *Journal of Composite Materials* **1987,** 21, 172-188.

(13) Gutowski, T.G.; Cai, Z.; Bauer, S.; Boucher, D.; Kingery, J.; Wineman, S. *Journal of Composite Materials* **1987**, 21, 650-669.

(14) Gebart, B.R. *Journal of Composite Materials* **1992**, 26, 1100-1133.

(15) Kim, Y.R.; McCarthy, S.P.; Fanucci, J.P.; Nolet, S.C.; Koppernaes, C. *22nd International SAMPE Technical Conference* **1990**, 22, 709-723.

(16) Ahn, K.J.; Seferis, J.C.; Berg, J.C. *Polymer Composites* **1991**, 12 (3), 146-152.

(17) Williams, J.G.; Morris, C.E.M.; Ennis, B.C. *Polymer Engineering and Science* **1974**, 14 (6), 413-419.

(18) Dave, R.; Houle, S. *Proceedings of the American Society for Composites Fourth Technical Conference*; Technomic: Lancaster, PA, 1990; 539-547.

(19) Bruschke, M.V.; Advani, S.G. *Polymer Composites* **1990**, 11 (6), 398-405.

(20) Bruschke, M.V.; Advani, S.G. *SAMPE Quarterly* **1991**, 23 (1), 2-11.

(21) Bruschke, M.V.; Advani, S.G. *Transport Phenomena in Material Processing*; ASME: New York, 1990; 149-158.

(22) Sadiq, T.A.K.; Advani, S.G.; Parnas, R.S. *Int. J. Multiphase Flow* **1995**, 21 (5), 755-774.

(23) Hammond, V.H. M.Sc. Thesis, Virginia Polytechnic Institute and State University, Blacksburg, VA, 1993.

(24) Foley, M.F.; Gutowski, T. *23rd International SAMPE Technical Conference* **1991**, 23, 326-340.

(25) Weideman, M.H. M.Sc. Thesis, Virginia Polytechnic Institute and State University, Blacksburg, VA, 1992.

(26) Adams, K.L.; Miller, B.; Rebenfeld, L. *Polymer Engineering and Science* **1986**, 26 (20), 1434-1441.

(27) Lam, R.C.; Kardos, J.L. *Proceedings of the American Society for Composites Third Technical Conference*; Technomic: Lancaster, PA, 1988; 3-11.

(28) Molnar, J.A.; Trevino, L.; Lee, L.J. *Proceedings of the 44th Annual Conference of the Composites Institute*; SPI: Washington, D.C., 1989; Paper 20A.

(29) Kim, S.W.; Lee, K.J.; Seferis, J.C.; Nam, J.D. *Advances in Polymer Technology* **1997**, 16 (3), 185-197.

(30) Adams, K.L.; Rebenfeld, L. *Polymer Composites* **1991**, 12 (3), 179-185.

(31) Batch, G.L.; Cumiskey, S. *Proceedings of the 45th Annual Conference of the Composites Institute*; SPI: Washington, D.C., 1990; Paper 9A.

(32) Wang, T.J.; Wu, C.H.; Lee, L.J. *Polymer Composites* **1994**, 15 (4), 278-288.

(33) Adams, K.L.; Russel, W.B.; Rebenfeld, L. *Int. J. Multiphase Flow* **1988**, 14, 203.

(34) Sun, X.; Li, S.; Lee, L.J. *Polymer Composites*, 19 (6) **1998** 807-817.

(35) Phelan, Jr., F.R. *Proceedings of the American Society for Composites Seventh Technical Conference*; Technomic: Lancaster, PA, 1992; 90-102.

(36) Fracchia, C.A.; Castro, J.; Tucker, III, C.L. *Proceedings of the American Society for Composites Fourth Technical Conference*; Technomic: Lancaster, PA, 1989; 157-166.

(37) Osswald, T.A.; Tucker, C.L. *International Polymer Processing* **1990**, 79-87.

(38) Bickerton, S.; Advani, S.G. *Composites Science and Technology* **1997**, 57, 23-33.

(39) Lee, L.J.; Young, W.B.; Lin, R.J. *Composite Structures* **1993**, 27, 109-120.

(40) Young, W.B. *Polymer Composites* **1994**, 15 (2), 118-127.

(41) MacRae, J.D. M.Sc. Thesis, Virginia Polytechnic Institute and State University, Blacksburg, VA, 1994.

(42) Caba, A.C. M.Sc. Thesis, Virginia Polytechnic Institute and State University, Blacksburg, VA, 1998.

(43) Calhoun, D.R.; Yalvac, S.; Wetters, D.G.; Wu, C.H.; Wang, T.J.; Tsai, J.S.; Lee, L.J. *Polymer Composites* **1996**, 17 (2), 251-264.

(44) Kang, M.K.; Lee, W.; Yoo, J.Y.; Cho, S.M. *Journal of Materials Processing & Manufacturing Science* **1995**, 3, 297-313.

(45) Gauvin, R.; Trochu, F.; Lemenn, Y.; Diallo, L. *Polymer Composites* **1996**, 17 (1), 34-42.

(46) Yousefi, A.; Lafleur, P.G.; Gauvin, R. *Polymer Engineering and Science* **1997**, 37 (5), 757-770.

(47) Gauvin, R.; Trochu, F. *Polymer Composites* **1998**, 19 (3), 233-240.

(48) Diallo, M.L.; Gauvin, R.; Trochu, F. *Polymer Composites* **1998**, 19 (3), 246-256.

(49) Friedrichs, B.; Guceri, S.I. *Polymer Engineering and Science* **1995**, 35 (23), 1834-1851.

(50) Chiu, H.T.; Wu, C.H.; Lee, J.L. *ANTEC '96 - 54th Annual Conference Proceedings*; SPE: Brookfield, CT, 1996; 1, 910-916.

(51) Ismail, Y.M.; Springer, G.S. *Journal of Composite Materials* **1997**, 31 (10), 954-977.

(52) Michaeli, W.; Dyckhoff, J. *Advanced Composites '93: International Conference*; TMS: Warrendale, PA, 1993; 749-754.

(53) Chui, W.K.; Glimm, J.; Tangerman, F.M.; Jardine, A.P.; Madsen, J.S.; Donnellan, T.M.; Leek, R. *SIAM Review* **1997**, 39 (4), 714-727.

(54) Chen, Y.F.; Stelson, K.A.; Voller, V.R. *Journal of Composite Materials* **1997**, 31 (11), 1141-1161.

(55) Young, W.B.; Chuang, M.T. *Journal of Composite Materials* **1995**, 29 (16), 2192-2215.

(56) Young, W.B.; Lai, C.L.; *Composites - Part A* **1997**, 28, 817-822.

(57) Binetruy, C.; Hilaire, B.; Pabiot, J. *Composites Science and Technology* **1997**, 57, 587-596.

(58) Binetruy, C.; Hilaire, B.; Pabiot, J. *Journal of Composite Materials* **1998**, 32 (3), 223-243.

(59)Young, W.B. *Journal of Composite Materials* **1996**, 30 (11), 1191-1209.

(60) Barrer, R.M. *Disc. Faraday Soc.* **1948**, 3 (61).

(61) Shaw, D.J. *Introduction to Colloid and Surface Chemistry*; Butterworth-Heinemann: Boston, 1992; 67.

(62) Dave, R. *Journal of Composite Materials* **1990**, 24, 22-41.

(63) Patel, N.; Rohatgi, V.; Lee, L.J. *Polymer Composites* **1993**, 14 (2), 161-172.

(64) Patel, N.; Rohatgi, V.; Lee, L.J. *Polymer Engineering and Science* **1995**, 35 (10), 837-851.

(65) Rohatgi, V.; Patel, N.; Lee, L.J. *Polymer Composites* **1996**, 17 (2), 161-170.

(66) Chang, C.Y.; Hourng, L.W.; Wu, C.J. *Journal of Reinforced Plastic Materials* **1997**, 16 (6), 566-586.

(67) Kalliadasis, S.; Chang, H.C. *Physics of Fluids* **1994**, 6, 12-23.

(68) Hourng, L.W.; Chang, C.Y. *Journal of Reinforced Plastics and Composites* **1998**, 17 (1), 2-25.

(69) Batch, G.L.; Chen, Y.T.; Macosko, C.W. *Journal of Reinforced Plastics and Composites* **1996**, 15, 1027-1051.

(70) Chang, C.Y.; Hourng, L.W. *Journal of Reinforced Plastics and Composites* **1998**, 17 (2), 165-182.

(71) Beckwith, S.W.; Hyland, C.R. *SAMPE Journal* **1998**, 34 (6), 7-19.

(72) Pike, T.; McArthur, M.; Schade, D. *28th International SAMPE Technical Conference* **1996**, 28, 374-380.

(73) Poe, Jr., C.C.; Dexter, H.B.; Raju, I.S. *Journal of Aircraft* **1999**, 36 (5), 876-884.

(74) Clarke, S. *29th International SAMPE Technical Conference* **1997**, 29, 21-31.

(75) Seemann, W.H. U.S. Patent 4 902 215, 1990.

(76) Seemann, W.H. U.S. Patent 5 052 906, 1991.

(77) Seemann, W.H. U.S. Patent 5 316 462, 1994.

(78) Seemann, W.H. U.S. Patent 5 439 635, 1995.

(79) Seemann, W.H. U.S. Patent 5 601 852, 1997.

(80) Seemann, W.H. U.S. Patent 5 702 663, 1997.

(81) Wienhold, P.D.; Wozniak, J.J. *SAMPE Journal* **1998**, 34 (1), 5-10.

(82) Nguyen, L.B.; Juska, T.; Mayes, J.S. *AIAA/ASME/ASCE/AHS/ASC Structures, Structural Dynamics, and Materials Conference*; AIAA: New York, 1997; 2, 992-1001.

(83) Kosmatka, J.B.; Hornbeck, B.; Policelli, F.; Bernetich, K. *28th International SAMPE Technical Conference* **1996**, 28, 1228-1239.

(84) Kosmatka, J.B. *Composite Structures* **1999**, 4 99-115.

(85) Bernetich, K.; Briggs, D.; Viskocil, S. *28th International SAMPE Technical Conference* **1996**, 28, 1240-1248.

(86) *Composites Technology* **1999**, September/October, 21-28.

(87) Lazarus, P. *41st International SAMPE Symposium and Exposition*; SAMPE: New York, 1996; 41, 1447-1458.

(88) Ni, J.; Sun, X..; Lee, L.J. *Polymer Composites*, 19 (6) **1998** 818-829.

(89) Le Comte, A. U.S. Patent 5 096 651, 1992.

(90) Le Comte, A. U.S. Patent 5 304 339, 1994.

(91) Lewit, S.M.; Jakubowski, J.C. *42nd International SAMPE Symposium and Exposition*; SAMPE: New York, 1997; 42 (2), 1173-1187.

(92) Clark-Schwebel Fiber Glass Corporation, White Plains, NY, 1999.

(93) Callister, W.D. *Materials Science and Engineering: an Introduction*; John Wiley and Sons: New York, 1997.

(94) The Dow Chemical Company, Midland, MI, 1999.

(95) Ciba Specialty Chemicals, Brewster, NY, 1999.

(96) Applied Poleramic, Inc., Benicia, CA, 1999.

(97) Reddy, J.N. *An Introduction to the Finite Element Method*; McGraw Hill: New York, 1993.